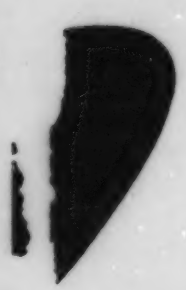

DEFENCE R&D DÉFENSE

Millimetre Wave Antennas Using an Array of Lenses

Capt J.C.R. Poirier, CD., Mr. J. Moffat
Dr. G. Morin and Dr. Y. Antar
Defence Research Establishment Ottawa

This document and the information it contains is disclosed in confidence for defence information purposes only, with no disclosure to others or any other use (including manufacturing use) to be made without the written permission of the Canadian Department of National Defence. This document contains proprietary information.

Defence R&D Canada
DEFENCE RESEARCH ESTABLISHMENT OTTAWA

TECHNICAL REPORT
DREO TR 2000-081
December 2000

National Defence Défense nationale

Canada

DEFENCE R&D DÉFENSE

Millimetre Wave Antennas Using an Array of Lenses

Capt J.C.R. Poirier, CD., Mr. J. Moffat
Dr. G. Morin and Dr. Y. Antar
Military Satellite Communications Group
Space Systems and Technology Section

This document and the information it contains is disclosed in confidence for defence information purposes only, with no disclosure to others or any other use (including manufacturing use) to be made without the written permission of the Canadian Department of National Defence. This document contains proprietary information.

DEFENCE RESEARCH ESTABLISHMENT OTTAWA

TECHNICAL REPORT
DREO TR 2000-081
December 2000

Project
5CA12

ABSTRACT

One technique to increase the gain of a single radiating element is to use a conventional lens supported above a microstrip patch element. This configuration allows modification of both the inside and the outside surface curvatures of the lens. The frequency band studied is 43.5-45.5 GHz.

Four different lens types have been investigated using simulation software. Two lens types have been designed and fabricated, a plano-convex lens to validate the simulation software and a meniscus lens to validate the results of the most promising lens.

During this research, it was demonstrated that when using a lens above a radiating element, the gain is effectively increased. As a starting point, for a single element without a lens, the measured gain was 5.1 dB. From laboratory measurements, the gain while using a plano-convex lens with the straight face facing the radiating element was 13 dB, an increase of 7.9 dB compared to the measured single element. Using a meniscus lens, based on the same design criteria as the plano-convex lens, the gain increase was 9.1 dB. For an array of 4 elements using a four plano-convex lens array, a 9 dB increase in gain from 8.2 dB to 17.2 dB was measured. A major observation while doing measurement was the impact of the reflected signal from the inside surface of the lens. In the case of the meniscus lens, a gain fluctuation of 2.3 dB was observed when the lens-to-patch distance changed by 1.5 mm.

RÉSUMÉ

Une technique pour augmenter le gain d'un élément irradiant est de positionner une lentille conventionnelle au-dessus d'un élément microstrip. Cette configuration permet ainsi de modifier les courbures internes et externes de la lentille. La bande de fréquence étudiée est 43.5-45.5 GHz.

Quatres types de lentilles ont été analysées en utilisant un logiciel de simulation. Pour valider les résultats de la simulation, un prototype a été fabriqué et mesuré en laboratoire. En realité, deux types de lentilles ont été fabriquées, une lentille plano-convexe pour la validation du logiciel de simulation et une lentille ménisque pour valider en laboratoire les performances de la lentille démontrant les meilleurs attributs

Lors de cette recherche, il fut démontré qu'effectivement l'utilisation d'une lentille positionnée au-dessus d'un élément irradiant peut améliorer le gain de ce dernier. Comme point de depart, le gain mesuré en laboratoire pour un élément irradiant simple est de 5.1 dB. Lors des mesures en laboratoire, le gain observé pour une lentille plano-convexe ayant la surface plane orientée vers l'élément irradiant est de 13 dB, soit une augmentation de 7.9 dB alors que l'augmentation du gain pour une lentille ménisque est de 9.1 dB. Pour un réseau de quatre éléments utilisant un réseau de quatre lentilles plano-convexes, l'augmentation du gain est de 9 dB, soit un gain passant de 8.2 dB à 17.2 dB. Une observation majeure fut l'impact de la réflection du signal primaire sur la surface interne de la lentille. Dans le cas de la lentille ménisque, une différence en gain de 2.3 dB peut être observée alors que la lentille est déplacée de 1.5 mm seulement.

102-01342/

EXECUTIVE SUMMARY

For limited-scan arrays, high-gain elements can be used to reduce implementation and maintenance cost. With higher gain elements, fewer elements are required to achieve the same antenna performance, the feed network is less complex, and the overall size of the antenna can be reduced. Alternately, if the number of elements is maintained, the overall performance of the array will improve with increasing element gain. Various techniques could be used to produce higher gain elements. The radiating element can be placed in a cavity, however this approach is costly and the array becomes bulky. A hemispherical lens with a flat bottom surface could be placed directly on the planar radiating element; however, this may not produce optimum performance. One technique that has not been explored is the use of a conventional lens supported above a microstrip patch element, thus allowing arbitrary shapes of both the inside and the outside surface curvatures of the lens. This approach was investigated in this study with the final objective being the demonstration of a 4-element array at 44.5 GHz using the developed high-gain element.

The single radiating element and the array of four radiating elements, including the feed networks, were implemented using microstrip technology. The lens designs were done using geometrical concepts and equations. However, simulation software employing physical optics principles was used to predict the focal point of various lenses.

It was effectively demonstrated that this architecture resulted in an increase of the gain of the individual antenna element. Various lens shapes were investigated using simulation software. Two single lens prototypes were manufactured, the first one to validate the software simulation and the second one to observe the measured results of the most promising lens, the meniscus lens. Finally an array prototype of four lenses was manufactured and measured.

A major observation while doing measurement was the impact of the reflected signal from the inside surface of the lens. In the case of the meniscus lens, a gain fluctuation of 2.3 dB was observed when the lens-to-patch distance changed by 1.5 mm.

Based on the results obtained, the approach of using a small lens above a single microstrip element was proven to be an effective means to increase the element gain. New designs of antennas using an arrangement of higher gain elements can be developed or old designs can be improved while maintaining the lightweight and low profile nature of the antenna.

Poirier, René, Moffat, John, Morin, Gilbert, and Antar, Yahia, Millimetre Wave Antennas Using an Array of Lenses. Defence Research Establishment Ottawa, DREO TR 2000-081, December 2000.

SOMMAIRE

Pour un réseau d'antennes à balayage restreint, il est requis d'avoir des éléments à gain élevé pour réduire les coûts de production et d'exploitation. En utilisant des éléments à plus haut gain, moins d'éléments sont requis pour obtenir des performances similaires. Le réseau d'alimentation sera moins complexe et la dimension de l'antenne sera réduite. En gardant le même nombre d'éléments, les performances de l'antenna vont augmenter en comparaison à une antenna sans lentilles. Différentes techniques sont présentement disponibles pour obtenir des éléments à rendement élevé. Ces techniques peuvent inclure de placer l'élément irradiant à l'intérieur d'une cavité, ce qui rend le système lourd et encombrant, ou de placer une lentille ayant un coté plat directement sur l'élément irradiant, ce qui ne génère pas une performance optimum. Une technique n'ayant pas été explorée serait de positionner une lentille conventionnelle au-dessus d'un élément irradant, permettant ainsi de modifier les courbures internes et externes de la lentille. Cette approche a été étudiée, avec pour objectif final de démontrer l'utilisation d'un réseau de quatre éléments à 44.5 GHz.

Pour le design et la réalisation de l'élément irradiant ainsi que pour le réseau de quatres éléments, incluant le réseau de distribution, la technologie microstrip fut utilisée. Pour la réalisation des lentilles, les concepts et les équations de l'optique géomitrique furent utilisés. Cependant pour la prédiction du point focal des lentilles, l'utilisation de l'optique physique fut requis par l'intermédaire du logiciel de simulation.

Il a été démontré lors de cette recherche qu'effectivement le gain d'un simple élément peut être accru considérablement lorsque combiner avec l'utilisation d'une lentille. Quatre types de lentilles furent analysées par simulation en utilisant un logiciel approprié. Deux types de lentilles furent construites physiquement, la première pour valider les résultats des simulations du logiciel et la deuxième, une lentilles ménisque, pour observer les mesures en laboratoire de la lentille la plus prometteuse. Finalement la simulation et la construction d'un réseau de quatre lentilles fut réalisé.

Une observation majeure fut l'impact de la réflection du signal primaire sur la surface interne de la lentille. Dans le cas de la lentille ménisque, une différence en gain de 2.3 dB peut être observée alors que la lentille est déplacée de seulement 1.5 mm.

Basé sur les résultats obtenus, l'approche utilisant une lentille conventionelle au-dessus d'un élément irradiant donne effectivement un rendement accru. Il est maintenant possible de réaliser de nouveaux designs d'antenne ou d'améliorer d'anciens designs utilisant des éléments à plus haut gain tout en gardant une antenne légère et de bas profil.

Pourier, René, Moffat, John, Morin, Gilbert, and Antar, Yahia, Antennes micro-onde utilisant un réseau de lentilles, Le Centre de recherches pour la défense Ottawa, DREO TR 2000-081, décembre 2000. (en anglais)

TABLE OF CONTENTS

ABSTRACT iii
RÉSUMÉ iii
EXECUTIVE SUMMARY v
SOMMAIRE vi
LIST OF FIGURES ix
LIST OF TABLES xi
LIST OF ACRONYMS AND ABBREVIATIONS xiii
CHAPTER 1: INTRODUCTION 1
1.1 Introduction 1
1.2 Objectives 1
1.3 Steps of Accomplishment of the Objectives 1
1.4 Overview of the Field of Study 1
1.5 Report Organization 2
CHAPTER 2: THEORY 5
2.1 Single Radiating Element 5
2.2 Array 6
2.3 Lens 7
2.3.1 Dielectric lenses 7
2.3.2 Equations for the contour of lenses 8
2.3.3 Plano-convex lens 9
2.3.4 Meniscus lens 9
2.3.5 Straight face lens 9
2.3.6 Conventional converging lens 10
CHAPTER 3: DESIGN 13
3.1 Simulation Software 13
3.1.1 High Frequency Structure Simulator (HFSS) 13
3.1.2 IE3D 13
3.2 Dielectric Substrate Selection 13
3.3 Single Radiating Element 14
3.3.1 Resonant frequency 15
3.3.2 Matching 17
3.4 Array 19
3.4.1 Element spacing 19
3.4.2 Element configuration 21
3.4.3 Feed network optimization 23
3.5 Lens 32
3.5.1 Design of four lens types 32
3.5.2 Design of prototypes 33
CHAPTER 4: RESULTS 37
4.1 Physical Installations and Set-up 37
4.1.1 Experimental facilities 37
4.1.2 Experimental mounting 37
4.2 Single Radiating Element 38
4.3 Simulation of Four Lens Types 43
4.4 Prototype 1 - Single Straight Face Lens 47

4.4.1 Investigation of focusing region 51
4.5 Microstrip Element Array 52
4.6 Prototype 2 - Single Straight Face Lens for the Array 55
4.7 Prototype 3 - Lens Array 56
4.8 Prototype 4 - Meniscus lens 59
CHAPTER 5: INTERPRETATION OF RESULTS AND DISCUSSION 63
5.1 Introduction 63
5.2 Single Radiating Element 63
5.3 Single Radiating Element with Lens, Prototype 1 63
5.4 Four Element Array 64
5.5 Four Element Array with Lens, Prototypes 2 and 3 65
5.6 Gain Comparison from Laboratory Measurements 66
5.7 Analysis of the Focusing Region 67
5.8 Comparison of the Four Lens Types 68
5.9 Selection of the Lens 69
CHAPTER 6: CONCLUSIONS AND RECOMMENDATIONS 71
6.1 Summary 71
6.2 Accomplishments 71
6.2.1 New type of architecture for limited-scan array 71
6.2.2 Geometrical optics versus physical optics 72
6.2.3 Optimum lens selection 72
6.3 Future Work 73
6.3.1 Aperture-coupled patches 73
6.3.2 Lens matching 73
6.3.3 Reduction of edge scattering 73
6.3.4 Circular polarization patches 73
REFERENCES 75
APPENDIX A: Matlab files for lens design 77
APPENDIX B: Lens design specification 87

LIST OF FIGURES

Figure 1: Microstrip patch antenna 5
Figure 2: Rectangular microstrip patch antenna 6
Figure 3: Lens types 8
Figure 4: Lens contour equation parameters 9
Figure 5: Conventional lens equation parameters 10
Figure 6: Thick lens equation parameters 11
Figure 7: Resonant frequency setup 16
Figure 8: Patch resonant frequency determination by transmission simulation (a) Wide frequency range (b) Close-up at 44.5 GHz 16
Figure 9: Matching line simulation configuration 18
Figure 10: Simulated S11 results for single patch 19
Figure 11: Radiation pattern for spacing of 1 wavelength; phi = 0 cut. 20
Figure 12: Radiation pattern for spacing of 3 wavelengths; phi = 0 cut. 21
Figure 13: Array configuration: (a) square array, (b) staggered rows array, (c) hexagonal array with 3λ between elements 21
Figure 14: Lens array for hexagonal configuration 22
Figure 15: Radiation pattern for microstrip patch source for hexagonal array; phi = 0 ... 22
Figure 16: Feed network configuration 23
Figure 17: Feed network, transmission line impedances 24
Figure 18: Feed network matching line simulation configuration 24
Figure 19: Matching line and patch dimensions 25
Figure 20: S11 of matching line for feed network configuration 25
Figure 21: Power divider (a) without quarter-wave transformer (b) and with quarter-wave transformer. 26
Figure 22: 50 Ω to 100 Ω divider dimensions 26
Figure 23: S11, S21 and S31 for 50 Ω to 100 Ω divider 27
Figure 24: 100 Ω to 100 Ω divider dimensions 27
Figure 25: S11, S21 and S31 for 100 Ω to 100 Ω divider 28
Figure 26: Mitered 90° bend 29
Figure 27: Optimized 90° bend 29
Figure 28: S11, S21 for optimized 90° bend 29
Figure 29: 51.5° bend 30
Figure 30: S11 and S21 for 51.5° bend for (a) 50 Ω line (b) 100 Ω line 30
Figure 31: Feed network dimension 31
Figure 32: S11 for complete microstrip antenna array 31
Figure 33: Lens design shapes 33
Figure 34: Prototype 1 HFSS simulation 34
Figure 35: Mechanical design prototype 1 35
Figure 36: Mechanical design prototype 2 35
Figure 37: Mechanical design prototype 3 36
Figure 38: RF measurement setup 37
Figure 39: Picture of the four element array and lenses 38
Figure 40: Patch S11 laboratory measurements 39
Figure 41: Patch S11 simulation and lab measurement 40

Figure 42: Ripple analysis 40
Figure 43: Patch radiation patterns, simulation and measurement with no mask, phi=0° and phi=90° 41
Figure 44: Patch radiation patterns, simulation and measurement with and without mask, phi=0° and phi=90° 41
Figure 45: Patch gain from simulation 42
Figure 46: Patch gain from laboratory measurement 42
Figure 47: Transmission line loss 43
Figure 48: Physical focal region for four types of lens 44
Figure 49: Focal point, in plane XY, distance from bottom of the meniscus lens (a) at 12.99 mm (b) 11.99 mm (c) 9.99 mm 45
Figure 50: HFSS simulation radiation patterns for four lens types 47
Figure 51: Focal region for prototype 1 48
Figure 52: Radiation patterns for prototype 1 at various focal lengths 48
Figure 53: Radiation patterns, patch with lens, simulation and laboratory measurement with and without mask 49
Figure 54: Patch with lens prototype 1 gain from simulation 50
Figure 55: Patch with lens prototype 1 gain from laboratory measurement 51
Figure 56: Prototype 1, lens focusing region 51
Figure 57: HFSS simulation, lens focusing region 52
Figure 58: Array S11 laboratory measurements 52
Figure 59: Array Radiation patterns, simulation and measurement (a) phi 0 (b) phi 90 .. 54
Figure 60: Array gain from laboratory measurement 55
Figure 61: Prototype 2 focal region 56
Figure 62: Prototype 2 gain 56
Figure 63: Array with lens comparison radiation patterns (a) phi=0° (b) phi=90° 57
Figure 64: CP and XP comparison radiation patterns (a) phi=0° (b) phi=90° 58
Figure 65: Prototype 3, array with lens gain 59
Figure 66: Prototype 4, meniscus lens, radiation patterns (a) phi=0° (b) phi=90° 60
Figure 67: Prototype 4, lens focusing region 61
Figure 68: Prototype 4, Gain at various distances 61
Figure 69: Array pattern comparison: lab measurement and simulation 66
Figure 70: Gain comparison 67
Figure 71: Focusing region comparison 68

LIST OF TABLES

Table 1: Substrate comparison 14
Table 2: Microstrip patch trade-off 15
Table 3: Matching line preliminary dimensions 18
Table 4: Lens design specifications 32
Table 5: Prototype 1 specifications 34
Table 6: Location of radiating patch element 45
Table 7: F/D ratio for lens shapes 46
Table 8: Characteristic impedance variation for the matching line 53

LIST OF ACRONYMS AND ABBREVIATIONS

ε_o	permittivity of free space
ε_r	relative permittivity
ε_{reff}	relative effective permittivity
λ	wavelength
μ_o	permeability of free space
Ω	ohms (impedance)
c	speed of light
f_r	resonant frequency
h	substrate height
L	length of radiating element
ΔL	length of fringing effect of radiating element
N	index of refraction
W	width of radiating element
ARPS	Antenna Radiation Patterns Software
AUT	Antenna Under Test
CAD	Computer Aided Design
CRC	Communications Research Centre
DDARLing	DREO DFL Antenna Research Laboratory
DFL	David Florida Laboratory
DREO	Defence Research Establishment Ottawa
GO	Geometrical Optics
HFSS	High Frequency Structure Simulator
PO	Physical Optics
TDR	Time Domain Reflectometry

CHAPTER 1: INTRODUCTION

1.1 Introduction

For limited-scan arrays, high-gain elements are required to reduce fabrication and other implementation costs. Various techniques can be used to produce higher gain elements. These techniques include placing the radiating element in a cavity, however this approach is costly and leads to a bulky element. Another technique involves placing a hemispherical lens directly on the planar element, however, this produces a limited gain increase. One technique that has not been explored is the use of a conventional lens supported above a microstrip patch element. This approach was first investigated for one element. The final objective was the demonstration of the concept in an array configuration through implementation of a 4-element array at 44.5 GHz using the high-gain element developed.

1.2 Objectives

The primary objective of this work was to investigate the utilization of a dielectric lens located over a radiating element as a means of increasing its gain. Various shapes of lenses were investigated, as well as the application of the technique to a phased array. This research was in various domains of interest. A new antenna architecture was designed that combines a microstrip radiating element with a more conventional lens suspended over it, separated by an air gap. Plano-convex, meniscus and conventional lens shapes were investigated. Differences between geometrical optics and physical optics were emphasized.

1.3 Steps of Accomplishment of the Objectives

After developing a comprehensive understanding of the theory, a single radiating element was designed and optimized using software tools. This final design was simulated, then built and measured in the laboratory.

Four lens shapes were designed and their characteristics simulated with a 3-D simulation software program. Each lens was then combined with the single radiating element and simulated to determine radiation pattern and gain. To validate the simulation results, a lens prototype was built and integrated with the antenna element, and the simulated and measured performance of this combination compared.

A four-element microstrip phased array was then designed, optimized and simulated. One of the lens types investigated was chosen and a lens array designed and fabricated. Measurement of the microstrip phased array alone was compared with the simulations. The performance enhancement from the lens array was assessed by comparing the lab measurement before and after the installation of the lens array.

1.4 Overview of the Field of Study

The proliferation of recent and projected deployments of various systems at millimeter wave frequencies, such as mobile and satellite communications, resulted in an increased demand for high performance, small, light-weight and low profile antennas.

An antenna architecture, which can meet some of these requirements is the microstrip antenna. The characteristics of microstrip antennas can offer some advantages [1] such as: thin profile, light weight, simple to manufacture, low cost, easily integrated with circuits, and ease in fabricating simple arrays. Almost any shape of microstrip radiating element can be used in antenna design. One common shape is the rectangular patch, which can be modeled as a pair of radiating slots separated by a transmission line. Analysis of the rectangular patch has been described [2]. A major disadvantage is the wide main radiation beam; this results in low directivity. To improve the directivity, and at the same time the gain, single elements are combined in an array. Use of higher gain elements will then result in an array with higher gain.

One technique used to increase the element gain is to place the radiating element in a metal cavity. By properly selecting the size and the shape of the cavity, the gain can be increased by more than 3 dB [3]. While the antenna maintains a low profile, the system becomes heavy and bulky.

A second technique, which has been known for a long time, is the use of dielectric lenses. It has been shown that lenses can also be used in the microwave frequency range, and geometrical optics equations can be used in their design [4].

One technique that is currently used is to locate the lens directly on the radiating element, e.g. a slot or a patch. Hemispherical or hyperhemispherical lenses directly located on a slot antenna have been investigated [5-7]. It was also demonstrated that a dielectric lens can be directly located on a microstrip patch antenna that is being fed by a slot [8]. More investigation has been done on the reflections inside the substrate lens [9] and their potential to modify the radiation pattern. Finally, many applications like millimeter-wave frequency mixers and Schottky-diode receivers use this lens technique [10-12].

One project named EHF SATCOM-XLENS conducted by Spar Aerospace Limited investigated the used of more conventional lenses being separated by air from a horn antenna [13]. This design was at 44.5 GHz but using hemispherical lenses with diameters ranging from 207.01 mm to 596.9 mm which is 10 to 50 times larger than the proposed design in this project.

From the literature research conducted, it was found that no investigation had been performed on an antenna using a microstrip radiating element combined with various types of lenses located at different heights above the radiating element. This new approach allows more flexibility in the lens design, thus enabling the two surfaces to be shaped.

1.5 Report Organization

This introductory chapter presents the objectives of the work as well as the steps required to accomplish these goals. It also presents the contribution to the field of study accomplished by this work and provides a short overview intended to position the specific research within the broader field of research performed in the microwave antenna field.

In Chapter 2, a brief review of the needed theory is provided as background for the reader prior to the reading of the report. This chapter includes a review of a single radiating element as well as of an array of elements. Finally optics lens equations used to design the prototype lenses are reviewed.

Chapter 3 comprises the details of the design and fabrication of the prototypes, including all required optimizations. It also describes the simulation software used to optimize the antenna designs and predict the performance.

Chapter 4 includes the description of the physical resources used for the fabrication and the measurement of the antenna prototypes. Details of the experimental set-up built to carry out the measurement are also presented. However the main purpose of this chapter is to present both the simulation and the measurement results of the final single radiating element, the array of elements and the lens prototypes.

In Chapter 5, interpretation of the results and comparison between simulation and measurement results are discussed. The implication and usefulness of the results are explained.

Chapter 6 summarizes the findings and major conclusions reached in the discussion. It also indicates how well the goals of the research have been met and states the major aspects of the research that could have been done differently, in retrospect, and new directions in which the research could be continued.

CHAPTER 2: THEORY

2.1 Single Radiating Element

For the selection of the radiating element, a rectangular patch was chosen. The major goal of the work was to study the effect of the lens on radiation patterns. The selection of the radiating element shape can be arbitrary. However since the design of a rectangular patch is well understood and described in the literature, a rectangular patch was chosen.

The basic microstrip antenna consists of a thin metallic strip, the patch, placed above a ground plane. The patch and the ground plane are separated by a dielectric substrate [14].

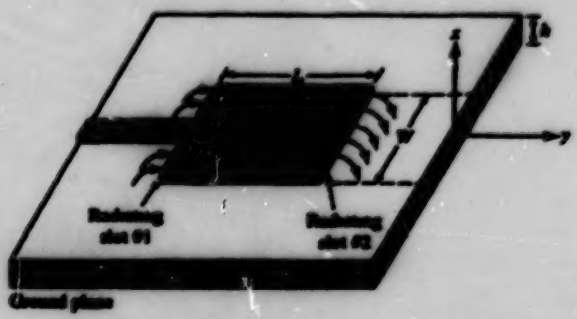

Figure 1: Microstrip patch antenna

From Figure 2, it can be noticed that two sides of the patch are considered the radiating edges. The length of the patch is inversely proportional to the frequency of operation and will be approximately half the wavelength in the dielectric at the design frequency.

In particular, knowing the relative dielectric constant of the substrate ε_r, the resonant frequency f_o, and the height of the substrate h, equations in reference [14] can be used to estimate the length (L) and width (W) of the antenna. In these equations, ε_o and μ_o are the permittivity and permeability of free space.

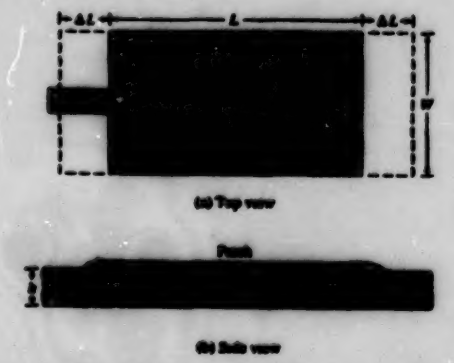

Figure 2: Rectangular microstrip patch antenna

$$W = \frac{1}{2f_r\sqrt{\mu_0\varepsilon_0}}\sqrt{\frac{2}{\varepsilon_r+1}}$$

$$L = \frac{1}{2f_r\sqrt{\varepsilon_{reff}}\sqrt{\mu_0\varepsilon_0}} - 2\Delta L$$

$$\varepsilon_{reff} = \frac{\varepsilon_r+1}{2} + \frac{\varepsilon_r+1}{2}\left(1+12\frac{h}{W}\right)^{-1/2}$$

$$\Delta L = 0.412h\frac{(\varepsilon_{reff}+0.3)\left(\frac{W}{h}+0.264\right)}{(\varepsilon_{reff}-0.258)\left(\frac{W}{h}+0.8\right)}$$

For the length, because of the fringing effects, the patch looks longer electrically than its physical size. This is why 2ΔL has to be subtracted from the electrical size of the patch. It has to be noticed that the dimensions derived from these equations are mostly applicable for lower frequencies because they are based on the transmission line model. It provides a square patch design, or close to a square patch. It is an excellent starting point for higher frequencies. To optimize the dimensions of the patch at 44.5 GHz, simulation software was used.

One important consideration of the microstrip antenna is the impedance matching of the patch to the feed network. The narrower the patch width, the higher will be the impedance. For matching purposes, to allow lower patch impedance, a rectangular patch was used.

2.2 Array

The radiation pattern of a single element is relatively wide, and provides low values of directivity and gain. To increase the directivity one solution is to increase the electrical size of the radiating antenna aperture. One way to enlarge the dimensions of the antenna is to form an assembly of radiating elements, referred to as an array.

The total field of the array is a combination of the element pattern and the array factor. To provide a very directive pattern, the fields from the elements have to interfere constructively in the desired directions and destructively in the remaining directions.

To shape the radiation pattern of the array, five types of controls can be applied. These controls are the geometrical configuration of the elements, the distance between elements, the excitation amplitude of the individual elements, the excitation phase of the individual elements, and the pattern of the individual elements [14]. In this report, besides the optimization of the individual element pattern, the two other factors to be investigated are the geometrical configuration and the distance between elements.

A major consideration in an array antenna is the formation of unwanted radiation peaks, called grating lobes. The location of the grating lobes can be determined by the following equation [15]:

$$\sin\theta_n = \sin\theta_0 + \frac{n\lambda_0}{d}$$

n = grating lobe number ≥ 1
θ_n = angle location of the n^{th} grating lobe
θ_0 = angle location of the main beam
λ_0 = wavelength
d = element spacing

By having the main beam located at $\theta = 0$ degrees, if the elements are separated by one wavelength, the first grating lobe will be at $\theta = 90$ degrees. However, the greater the separation between the elements, the closer the grating lobes will get to the main beam. Various spacings were investigated in relation to the required design specifications.

2.3 Lens

2.3.1 Dielectric lenses

Various shapes of dielectric lenses can be used to modify the radiation pattern of an antenna. One objective of this work was to study different lens types and exploit the best possible shape for the final design. The following are the 4 lens types being studied: (a) the plano-convex lens, (b) the meniscus lens, (c) the straight face lens, and (d) the conventional converging lens. While, other shapes of lenses could have been investigated, these shapes are the basic ones that were used for lens design.

The plano-convex lens (a) has a flat outer and a hyperbolic inner surface. The meniscus lens (b) has a spherical inner surface and an elliptical outer surface. The straight face lens (c), which is also a plano-convex lens, is named differently so that it can be distinguished in this document. It has a flat inner and a hyperbolic outer surface, while the conventional converging lens (d) has spherical inner and outer surfaces.

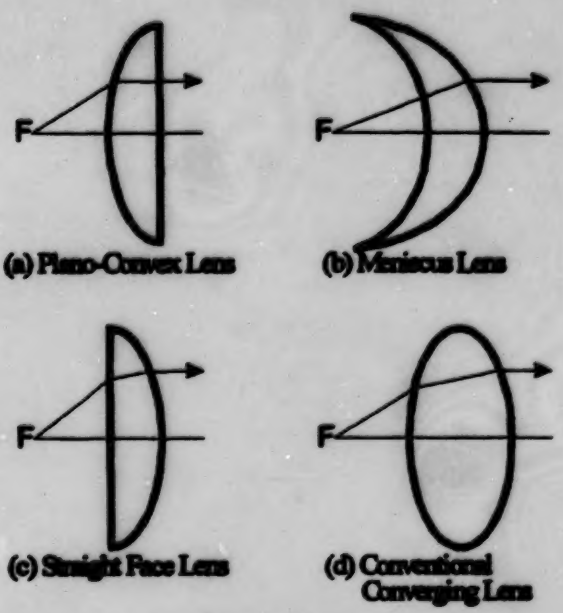

Figure 3: Lens types

2.3.2 Equations for the contour of lenses

Analytically the lenses (1) to (4) can be defined by selecting the optical axis to pass through the center of the lens and by determining the inner and outer lens contours $f_1(y_1,z_1)$ and $f_2(y_2,z_2)$. Then, by rotating f_1 and f_2 about the optical axis, the axially symmetric lenses are generated. The four lenses studied can direct the radiation from a point source F to a plane wave in front of the outer surface of the lens. In [18], the basic equations to determine f_1 and f_2 for the three first cases are stated. These equations are described in detail.

One important lens concept is the optical path. All rays passing through one of the studied lenses should have the same optical length. The parameter N is the lens index of refraction and is also defined as the square root of the dielectric constant of the lens, $N = \sqrt{\varepsilon}$. For the optical path to be the same for all rays passing through the lens in Figure 4, then

$$R + ND + t = D_1 + ND_0$$

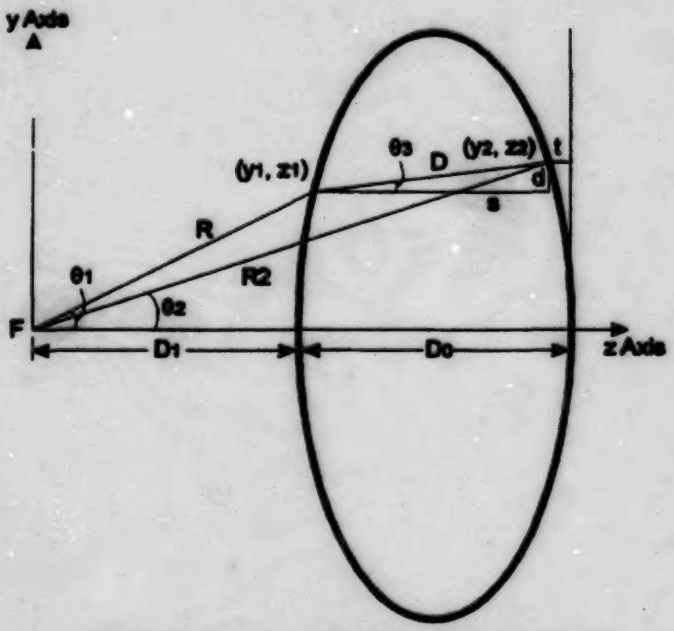

Figure 4: Lens contour equation parameters

2.3.3 Plano-convex lens

For the plano-convex lens, by looking at Figure 3 for the shape of the lens and Figure 4 for the parameters, the outer surface is a plane given by

$$z_2 = D_1 + D_0$$

the inner plane can be determined using the optical path equation.

$$R = D_1 + N(R\cos\theta_1 - D_1)$$

Solving for R in term of θ_1.

$$R(\theta_1) = \frac{D_1(N-1)}{N\cos\theta_1 - 1}$$

2.3.4 Meniscus lens

For the meniscus lens, the inner surface is spherical and can be defined as

$$f_1 = (y_1^2 + z_1^2)^{1/2}$$

and the outer elliptical surface is defined by

$$R_2(\theta_2) = \frac{(D_1 + D_0)(N-1)}{(N - \cos(\theta_2)}$$

2.3.5 Straight face lens

The inner face is

$$z_1 = D_1$$

For the outer surface, the Snell's law at each surface is applied and the following equations can be derived

$$\theta_1 = \sin^{-1}(y_1 / R) = \tan^{-1}(y_1 / D)$$
$$\theta_2 = \sin^{-1}(\sin(\theta_1) / N)$$
$$D_2 = ND_0 + D_1$$
$$t = [(D_2 - R_0 \cos\theta_2 / N - D_0] / [\cos\theta_2 / N - 1]$$
$$s = D_0 - t$$
$$d = s \tan(\theta_2)$$
$$z_2 = s + D_1$$
$$y_2 = y_1 + d$$

2.3.6 Conventional converging lens

The case of the conventional converging lens is slightly different from the previous cases. The equations for the inner and outer contours are derived in [20]. They are rewritten to follow the same notation as the previously derived equations:

$$f_1(y) = T_1 - [R_1 - (R_1^2 - y^2)^{1/2}$$

$$f_2(y) = T_2 - [R_2 - (R_2^2 - y^2)^{1/2}$$

However, f_1 and f_2 have to be moved on the z-axis depending on the lens thickness, T, to join together the three lens layers, as shown in Figure 5.

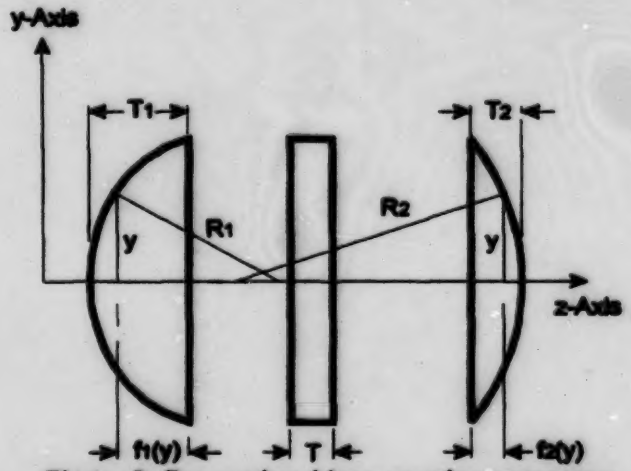

Figure 5: Conventional lens equation parameters

The focal length, f, for thin lens is defined as

$$\frac{1}{f} = (N-1)(\frac{1}{R_1} - \frac{1}{R_2})$$

A sign convention has to be defined; if R is to the right of the lens contour, it is positive, if R is to the left of the lens contour, it is negative.

A more general approach is developed in Borrelli's book [18] to determine the focal point F. A two-component vector is formed with the first component representing the distance above or below the optical axis, y_1 or y_2, and the second representing the slope of the ray *m* through the point, defined as $m_1=y_1/s_1$, s_1 being the distance from the lens to the point where the ray is crossing the optical axis. This can be visualized in Figure 6.

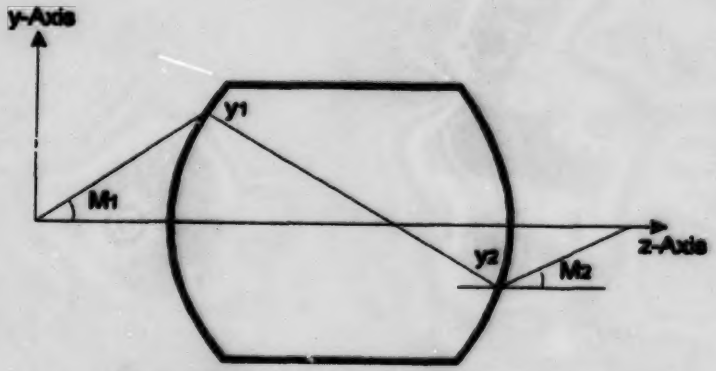

Figure 6: Thick lens equation parameters

The vector is simply:

$$\begin{bmatrix} y_2 \\ m_2 \end{bmatrix} = M \begin{bmatrix} y_1 \\ m_1 \end{bmatrix}$$

where M is made up of the product of three operations: the refraction at the first surface, the translation operation through the lens and, the refraction at the second surface.

$$M = \begin{bmatrix} 1 & 0 \\ -1/Nf_2 & 1/N \end{bmatrix} \begin{bmatrix} 1 & T \\ 0 & 1 \end{bmatrix} \begin{bmatrix} 1 & 0 \\ -1/Nf_1 & 1/N \end{bmatrix} = \begin{bmatrix} 1-(T/Nf_1) & T/N \\ (T/Nf_1f_2)-(1/f_1)-(1/f_2) & 1-(T/Nf_2) \end{bmatrix}$$

where T is the thickness of the lens and

$$f_i = \frac{R_i}{(N-1)}$$

with R_i being the radius of curvature of its surface. R_i is always positive.

To find the focal length, f, either m_1 or m_2 has to be parallel to the optical axis.

By assuming a thin lens with T=0 and m_2=0, M can be simplified to

$$M = \begin{bmatrix} 1 & 0 \\ -1/f_1 - 1/f_2 & 1 \end{bmatrix}$$

This leads to

$$\begin{bmatrix} y_2 \\ 0 \end{bmatrix} = \begin{bmatrix} 1 & 0 \\ -1/f_1 - 1/f_2 & 1 \end{bmatrix} \begin{bmatrix} y_1 \\ m_1 \end{bmatrix}$$

by solving the algebraic equations, remembering that $m_1=y_1/s_1$

$$0 = y_1\left(-\frac{1}{f_1} - \frac{1}{f_2}\right) + \frac{y_1}{s_1} \quad (1)$$

With s_1=f, since m_2=0, then

$$\frac{1}{f} = (N-1)(\frac{1}{R_1} + \frac{1}{R_2})$$

which is the well known formula for the focal length of a thin lens.

These equations were used in a software program developed in Matlab for the calculation of the lens surface curvatures required for the design, simulation and fabrication of the lenses.

CHAPTER 3: DESIGN

3.1 Simulation Software

Some antenna problems may be solved analytically, yielding approximate design expressions. However, often more design accuracy and flexibility are required. New desktop PC technology and advancement in numerical electromagnetic simulation bring the Computer Aided Design (CAD) capability to common users, and hence provide the design flexibility required. Two main simulation software tools were used in this work, HFSS produced by Ansoft [20] and IE3D produced by Zeland [21]. They are described in more detail in the following sections. A third software package called Antenna Radiation Patterns Software (ARPS) [25] was used in the simulation of the array radiation pattern. Other software was used to simplify mathematical calculations; Microwave Design Computations, by Rogers Corp., for the transmission lines and a software program from the reference book by Sainati [19], for the patch size calculation.

3.1.1 High Frequency Structure Simulator (HFSS)

Ansoft HFSS is a finite element analysis tool for the solution of complex electromagnetic problems. It permits a user to define a model in terms of geometry, material parameters, and boundary conditions and to solve Maxwell's equations within the model for different types of excitation. The 3D modeler of HFSS provides the capability to design in 3 dimensions, allowing for full simulation. HFSS allows the designer to compute and to view the following areas of interest: basic electromagnetic field quantities, such as antenna parameters, radiated fields and generalized S-parameters [20]. HFSS was used to simulate the lenses alone and the combination of the single element with a lens.

3.1.2 IE3D

Zeland IE3D is an electromagnetic simulator, which uses the method of moments. This method is commonly used for solving integral equations for the current distribution over a meshed structure, which includes the boundary conditions. This allows for the radiation patterns, S-parameters and other areas of interest to be solved [21]. Generally, IE3D was used to optimize the single radiating element as well as the array design. IE3D completes the simulation in less time than HFSS since it solves each problem on a surface rather than in a volume.

3.2 Dielectric Substrate Selection

The first step in the design of the single radiating microstrip element, or the array, is the selection of the dielectric substrate to be used. Based on readily available material at the DDARLing laboratory, evaluation of the material has been performed.

There are three main criteria for the selection of the substrate material. One is the thickness of the dielectric and the two others are related to the electrical properties, which are the relative dielectric constant ε_r and the loss tangent [16]. The higher the dielectric constant is, the smaller the patch will be, and generally the narrower the bandwidth. Because of the high operating frequency, 44.5 GHz, the patch size will already be small. The selection of ε_r is not required to be high to reduce the patch size, as space availability

is not a concern. A high loss tangent reduces antenna efficiency and increases feed losses. Feed loss is proportional to frequency, and at millimeter-wave frequencies, losses are expected to be important. Thus, in the selection of the substrate, it is best to have the lowest loss tangent. In the available material, Arlon CuClad 217 and Rogers Duroid 5880 had the lowest loss tangent of 0.0009. Their ε_r are 2.14-2.21 for Arlon and 2.181-2.215 for Rogers.

For a maximum operating frequency of f, the thickness h should satisfy the following equation in reference [19]. The substrate thickness should be as large as possible to maximize the bandwidth and the efficiency but not so large as to risk surface-wave excitation.

$h \leq \frac{0.3c}{2f\sqrt{\varepsilon_r}}$; c is the speed of light

For a frequency of 44.5 GHz, and the specified range for ε_r, the thickness should be approximately 0.2 mm for the substrate.

A comparison was done using a software program [19], which uses a transmission line model, on a 50 Ω transmission line over a 0.254 mm thick dielectric at 44.5 GHz to evaluate the loss performance. Two different dielectric constants were used: 2.17 for Arlon and 2.2 for Duroid. The width of the line used was 0.819 mm, determined using Rogers Corporation software [24]. As expected, since the variation in permittivity is minimal, the loss values were comparable, 0.0461 dB/cm for Arlon and 0.0464 dB/cm for Duroid. However, using HFSS simulation software, the losses were 0.0494 dB/cm for Arlon and 0.0574 for Duroid.

Substrate	ε_r	tan δ	loss [Rogers] dB/cm	loss [HFSS] dB/cm
Arlon CuClad 217	2.17	0.0009	0.0461	0.0494
Rogers Duroid 5880	2.2	0.001	0.0464	0.0574

Table 1: Substrate comparison

Based on loss performance which gives preference to Arlon and on the quantity of material available, the final selection was Arlon CuClad 217, 0.254 mm thick with a average $\varepsilon_r = 2.17$ and a loss tangent of 0.0009. The copper thickness on each side of the dielectric is 0.0173 mm.

3.3 Single Radiating Element

After the selection of the dielectric substrate, it was possible to begin the design of the rectangular patch.

Using a software program [19], it was possible to obtain various parameters for a variety of patch sizes. The results are illustrated in Table 2. The input parameters required were the substrate height, relative dielectric constant, loss tangent, the conductor relative conductivity, the patch length and width, the feed location, and the frequency. As for the output, the software provided the patch input resistance, total Q, efficiency, bandwidth, and the calculated resonant frequency.

Design Freq:	44.5 GHz					
Material:	Arlon 217					
Dielectric constant:	2.17					
Loss tangent:	0.0009					
Line thickness:	0.0173 mm					
Substrate height, h:	0.254 mm					
Using program PATCHD [19]						
L mm	W mm	Input resistance Ω	Q	Overall efficiency %	Bandwidth for SWR 2:1 %	PATCHD Calculated Resonant freq. GHz
2.05	2	365.87	15.880	84.80	4.45	44.491
2.02	3	196.80	12.580	85.42	5.62	44.486
2.01	3.5	156.85	11.641	85.60	6.07	44.489
2.00	4	130.08	11.014	85.71	6.42	44.468
2.01	5	97.73	10.394	85.83	6.80	44.474

Table 2: Microstrip patch trade-off

The length of the patch has to be approximately 2.00 mm, slightly smaller than one half-wavelength at the resonant frequency. The width can be selected based on the physical space available, or on the characteristics required, such as the patch impedance or the bandwidth. The narrower the patch is, the higher the patch impedance, and the more difficult it is to match to the feed network. Also, as the width decreases, so does the bandwidth. The patch size selected based on the simulator is 2.01mm x 3.5mm, which is the one resulting in a calculated resonant frequency of 44.489 GHz, and with a relatively realizable input impedance to match. The efficiency result takes into account the feed line losses and surface-wave excitation. The width of the patch also determines the frequency at which a second mode is radiating. The frequency of the second mode has to be kept away from the operating frequency to minimize the interference. The above result is based on mathematical equations, which provided a starting point for future optimization.

3.3.1 Resonant frequency

To provide a more accurate estimate of the resonant frequency of the patch, optimization of the patch length was done using IE3D simulation software. The technique used was to consider the patch as a resonant cavity with input and output coupling from transmission lines that are terminated close to, but not touching the cavity. This is illustrated in Figure 7. By connecting a source to one of the lines and measuring the signal present at the other line, the transmission through the patch as a function of frequency was determined. The patch length was adjusted until the maximum transmission occurred at the desired resonant frequency.

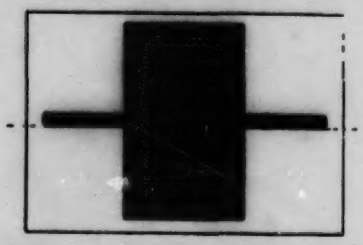

Figure 7: Resonant frequency setup

The transmission line width is 0.223 mm, which is the width required for a 100 Ω line using the selected dielectric substrate. Various air gaps were simulated. The air gap should be narrow enough so the energy is effectively coupled to the patch but wide enough so that the transmission line does not interfere with the radiation of the energy from the patch. The shape of the expected S21 results is known, a single peak of maximum value is expected at the resonant frequency, with the transmission decreasing rapidly when moving away from the resonant frequency. Air gap variations were investigated without changing the patch size. The final air gap length chosen was 0.05 mm. When the maximum transmission was at the desired resonant frequency, the patch was considered to be optimized.

After optimization of the patch length, the final size was 1.59 mm x 3.5 mm. The width was not changed and the length remained close the initially chosen values. The transmission from port one to port two, S21, is represented in the following graphs of Figure 8.

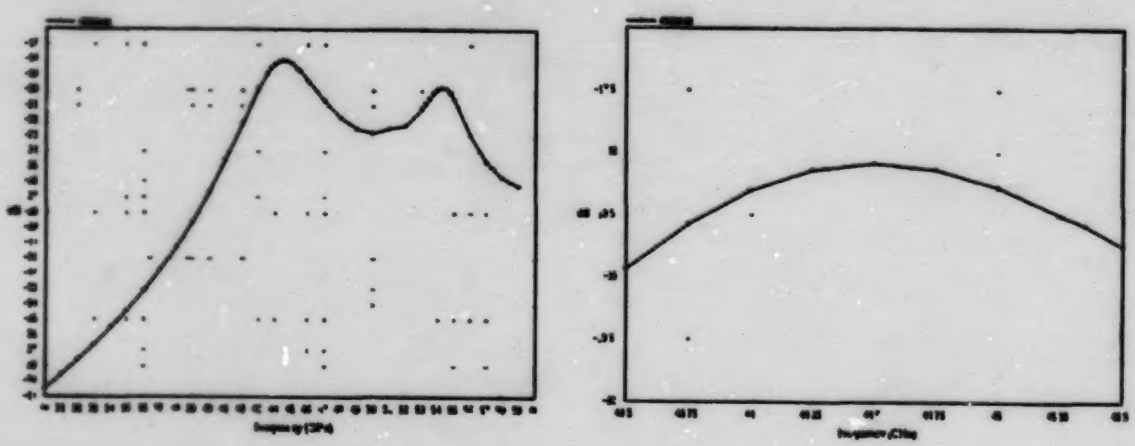

(a) (b)

Figure 8: Patch resonant frequency determination by transmission simulation
(a) Wide frequency range (b) Close-up at 44.5 GHz

In Figure 8, it is seen that the maximum S21 value is effectively at 44.5 GHz. A second maximum can be observed at approximately 54.3 GHz. It is possible with the simulation software to look at the electrical field on the patch for various frequencies. It

was found that at 44.5 GHz, the stronger E field is parallel to the length of the patch. At 54.3 GHz, the stronger E field is perpendicular to the length of the patch. Depending on the frequency, the two other parallel sides of the patch could radiate, leading to cross polarization. However, with the feed network being matched at the frequency of operation, the second frequency impact was expected to be negligible.

3.3.2 Matching

One important aspect of the feed network is the matching of the patch to the transmission line. Proper matching will result in better efficiency with more energy reaching the patch and not being reflected back. The final objective is to match the patch to a 50 Ω transmission line, with this line being connected to a coaxial cable. The impedance of the patch has two components, real and imaginary. The real part is the resistance component and the imaginary is the capacitive or the inductive reactance component. Matching is done in two steps, the first one is to take care of the capacitive or the inductive reactance by bringing it to zero and the second step is to match the resistance to the required impedance, in this case, 50 Ω.

Various techniques can be used for matching. The most common one uses a stub to remove the capacitive or the inductive reactance component, then a quarter wave transformer to adjust the resistance component. A second technique is to use a specific length of transmission line with a carefully chosen characteristic impedance to match both the real and the imaginary components.

This second matching technique was used here. It is an iterative experimental technique using software simulation. In it, the impedance that results by feeding the patch with lines having different characteristic impedances and lengths are determined and plotted. The line characteristic impedance that yields the desired result is then found and the final result simulated. This is described in the following procedure.

Step 1: Choose the patch size.
Step 2: Select a transmission line characteristic impedance; this will dictate the width of the feed line.
Step 3: Simulate the patch and the transmission line length of at least 2 wavelengths.
Step 4: Determine the patch impedance, normally done by a de-embedding technique.
Step 5: Normalize the patch impedance according to the characteristic impedance of the feed line.
Step 6: Plot the normalized patch impedance value on a Smith chart.
Step 7: On the Smith chart, rotate toward the generator until only the resistance component remains (at the intersection of the real axis).
Step 8: Calculate the value of the resistance component.
Step 9: Plot the resistance value on a Cartesian graph of load resistance versus characteristic impedance of the line.
Step 10: Repeat steps 2 to 9 for various line impedances. Draw a curve through the points on the Cartesian graph.
Step 11: On the Cartesian graph, locate the value of the line characteristic impedance required to produce the required load impedance.
Step 12: Repeat steps 2 to 9 for the line characteristic impedance.
Step 13: Find the length of the matching line in wavelengths from the Smith chart.

Step 14: Convert to linear measure (mm) if required.

The results obtained while performing the matching line procedures for the single radiating element using HFSS simulation software are shown in Table 3.

Patch W = 3.5 mm, L=1.99 mm:			
Feed line impedance Ohms	Feed line width (w) mm	Patch impedance Z=R+jI	Normalized Impedance
50	0.819	134.84+j84.32	2.70+j1.69
100	0.223	161.97+j18.39	1.62+j0.18
120	0.137	162.24+j14.34	1.35+j0.12
91.3	0.275	166.90+j36.16	1.83+j0.40
Guided wavelength for Zo 91.3 ohms: 5.0696 mm (from Rogers software) Length required, from Smith chart, 0.274 x lamda => 1.394 mm			

Table 3: Matching line preliminary dimensions

This technique is lengthy but gives an excellent starting point for the matching line dimension before software optimization is performed.

A more straightforward approach would be to use the transmission line equation. This would require knowledge of the impedance of the patch as a function of feed line width. Unless this was determined (through simulation or other means), use of a single value for calculations involving different feed line widths would lead to errors.

Optimization of the matching line was performed using IE3D software in the configuration of Figure 9. By slightly modifying the length and the width of the line, an improvement in the return loss, S11, was obtained. This was the criterion for the line matching dimension. The final matching line dimensions were 1.66 mm x 0.241 mm.

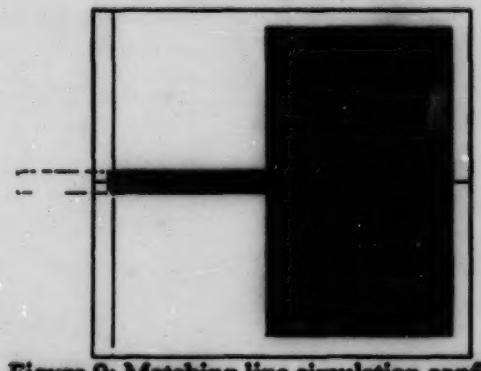

Figure 9: Matching line simulation configuration

For the final simulation, a 6 mm length of 50 Ω transmission line, of a width of 0.819 mm, was included between the port and the matching line. The return loss result, S11 is presented in Figure 10.

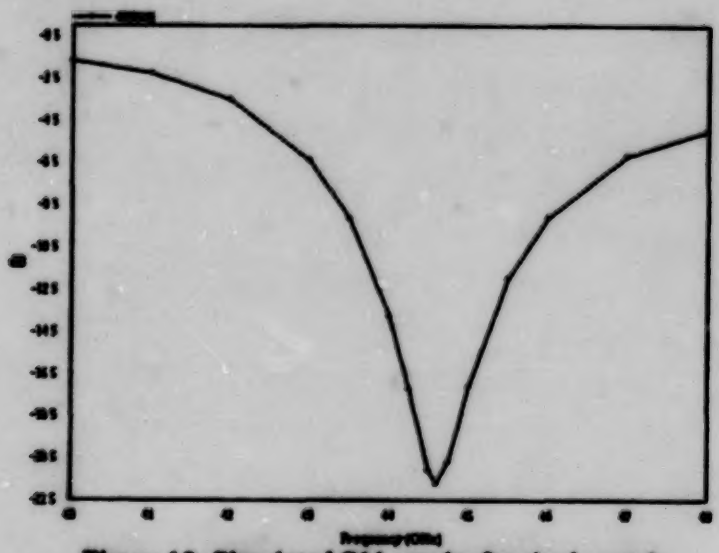

Figure 10: Simulated S11 results for single patch

3.4 Array

Two major steps in the array design have to be performed. The first one is the selection of the array configuration including the element spacing. The second one is the optimization of the feed network.

One design criterion, which was given, is that the antenna should allow for scanning capability. The constraint given was to be able to track a geosynchronous satellite, such as a Milstar satellite, which has a slightly inclined geosynchronous orbit.

A satellite in an inclined geosynchronous orbit will not actually be stationary in orbit. As seen from earth, the satellite will trace a curve, which resembles a figure 8 shaped pattern. This curve extends to ± 5 degrees to either side of the center. In the worst case, when the main lobe of the antenna is directed toward the satellite it will be pointed toward one end of this pattern. This means that the antenna needs to be able to be scanned over ± 10 degrees to keep tracking the satellite as it moves over the figure 8 shaped trajectory.

3.4.1 Element spacing

For this discussion, an antenna with a ±10° coverage area is pointing directly at the center of the figure 8 shaped pattern of the satellite. For the first grating lobe to not be within the figure 8 area, the location of that grating lobe needs to be at least 15° away from the beam center. Using the grating lobe equation, $\sin\theta_n = \sin\theta_0 + \frac{n\lambda_0}{d}$, theoretically, it is possible for the elements to be separated by up to 3.8 wavelengths apart. To account for misalignment of the antenna and the satellite, a spacing of 3

wavelengths was chosen. At 3 wavelengths, the first grating lobe appears at 19.5°. It has to be said that this is only a concept being used as a starting point to determine the element spacing. At 44.5 GHz, the wavelength is equal to 6.7369 mm, and 3 wavelengths becomes 20.2107 mm.

With the Antenna Radiation Patterns Software (ARPS) [25], it is possible to visualize the location of the grating lobes for different antenna element spacings.

Various simulations have been performed using ARPS to facilitate the understanding of grating lobe formation. The first simulation was using microstrip patch sources based on previously chosen design parameters for a square array of 4 elements. Results of the simulation of a square array with an element spacing of one wavelength are shown in Figure 11. Figure 12 shows how the results change when the element spacing is increased to 3 wavelengths. In this case, the simulation predicted that the first grating lobe would be at ±19.5°. This result is consistent with the prediction from the theory discussed in Chapter 2.

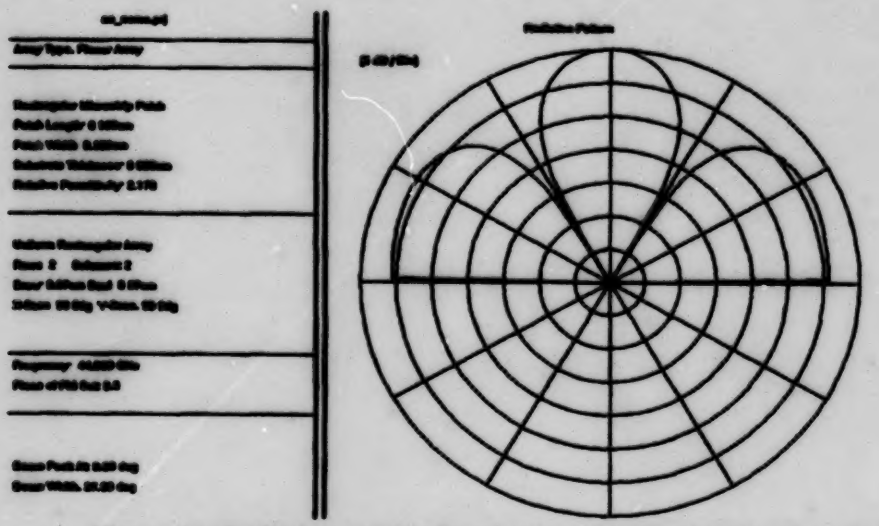

Figure 11: Radiation pattern for spacing of 1 wavelength; phi = 0 cut.

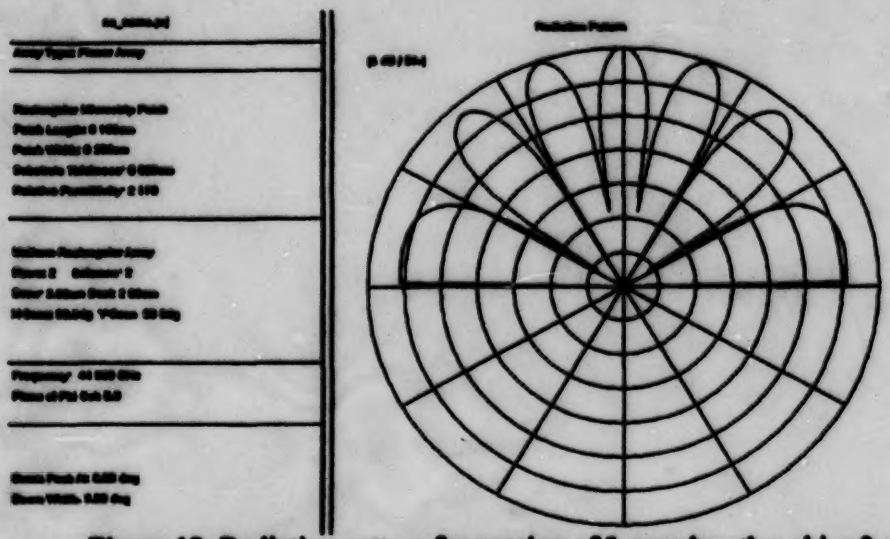

Figure 12: Radiation pattern for spacing of 3 wavelengths; phi = 0 cut.

3.4.2 Element configuration

The uniform rectangular array is the first one to come to mind when designing an array. A second configuration using staggered elements, in which the elements of one row are located mid way between the elements of the adjacent row, was analyzed. In Figure 13, three arrays are presented; (a) the square array with a spacing of 3λ between elements, (b) the staggered array with 3λ spacing between adjacent elements within each row and 3λ spacing between the rows, and (c) the hexagonal array with 3λ spacing between adjacent elements within each row and between adjacent elements in adjacent rows. In the last case, the physical space required for the array is the least.

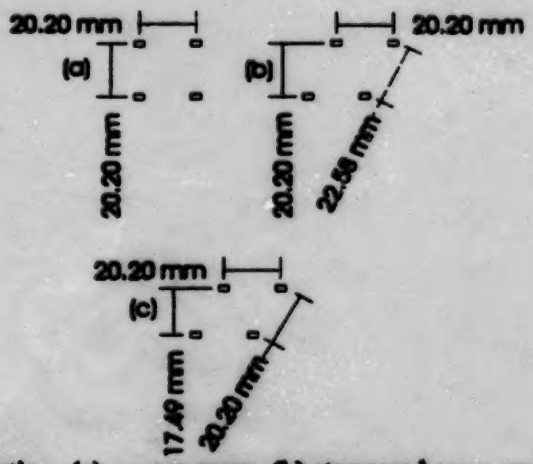

Figure 13: Array configuration: (a) square array, (b) staggered rows array, (c) hexagonal array with 3λ between elements

Another advantage of the hexagonal array (c) is to minimize the unused portion of the lens array, as shown in Figure 14.

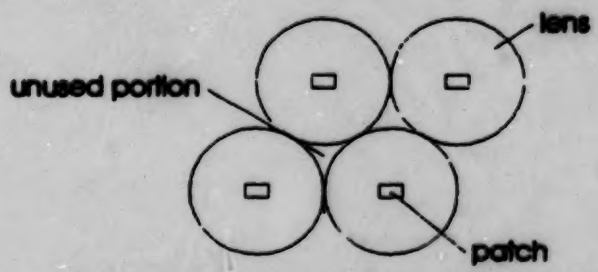

Figure 14: Lens array for hexagonal configuration

Using ARPS, the hexagonal configuration (c) was simulated using microstrip patch sources to evaluate the impact on the grating lobes. It can be observed in Figure 15, that one advantage is the reduction of the strength of the first and second grating lobes. However, it is noted that the location of the first grating lobe is now at 14°, which is slightly below the minimum design requirement. For scans in the plane of the magnetic field (phi = 90) the grating lobe pattern will be similar to the E field cut (phi = 0) for the square, shown in Figure 12.

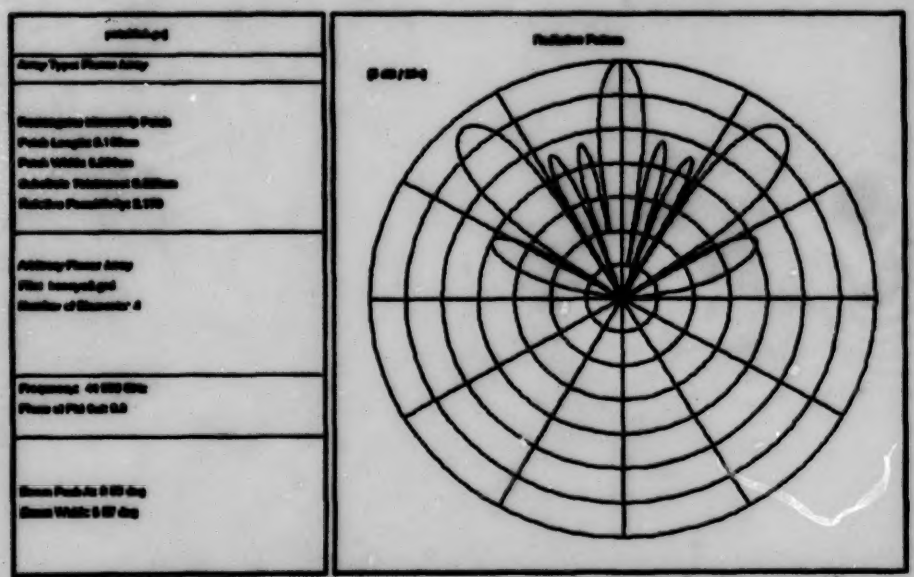

Figure 15: Radiation pattern for microstrip patch source for hexagonal array; phi = 0

Based on the advantages of a reduced physical array size, reduced unused section of the lens array and lower first and second grating lobe value in the electrical field plane, the hexagonal array (c) was chosen.

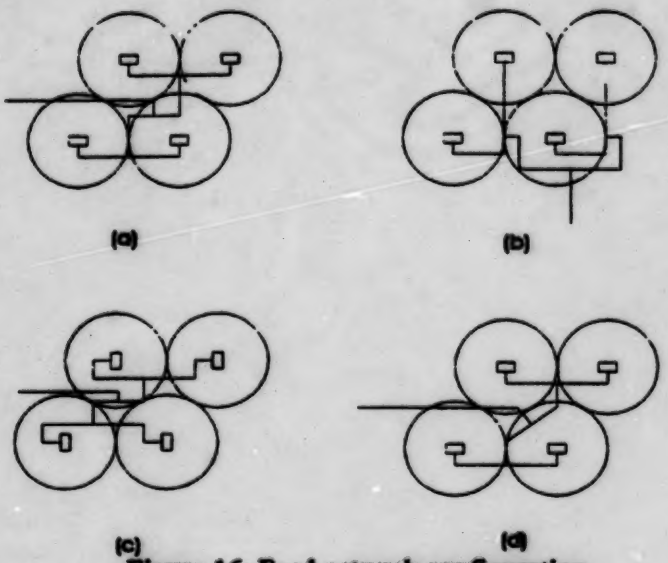

Figure 16: Feed network configuration

3.4.3 Feed network optimization

The next design step was to select the feed network configuration for the array. The configurations shown in Figure 16 were developed and analyzed.

One of the design objectives was to minimize the feed loss, since at millimeter wave frequencies, the loss could be significant. The shorter the feed network transmission lines are, the lower would be the loss. All the patches have to be fed and radiate in phase, meaning that they have to be fed on the same side with identical length lines. By looking at Figures 1 and 2, it can be seen that the fields, represented by the arrows, are on the feed line side, from the ground plane to the patch and on the other side from the patch to the ground plane. In an array the objective is to have the fields combined together and not canceling each other. Another option is to include a 180-degree phase shift for two patches, which will increase the length of the transmission line and at the same time increase the loss. All proposed configurations require three transmission line dividers, and various bends. Configuration (a) was the first one to come to mind and it has 7 bends. Configuration (b) has 8 bends and the top and bottom rows are not fed symmetrically. Configuration (c) has the most number of bends, a total of 11 bends. Configuration (d) is an improved version of (a) with three bends not being 90 degrees. The fewer discontinuities a transmission line is submitted to, the better its performance will be. Finally, configuration (d) was chosen since it has the minimum number of bends, the shorter lines and the minimum discontinuities with 3 bends not being 90 degrees.

The first decision to make was the transmission line characteristic impedance required for the various dividers. The feed network has to match an initial source of 50 Ω and final patch impedance of approximately 165 Ω. The feed network was organized as shown in Figure 17. The 50 Ω line is divided into two 100 Ω lines. A quarter-wave

transformer is used at the next divider to bring the impedance back to 50 Ω and immediately divide into two 100 Ω lines to feed into the patch matching stub.

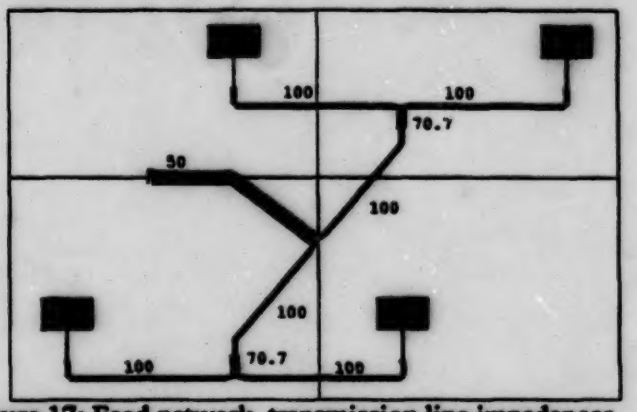

Figure 17: Feed network, transmission line impedances

Each element of the feed network must optimized individually before being incorporated to the final structure.

The two first items to be optimized were the 50 Ω and 100 Ω transmission lines. Based on the Rogers software the initial line width value provided is 0.819 mm for the 50 Ω line; this value was used in the previous design of the single patch. After analyzing the results of the simulation it was found that this value could be optimized to provide better results. The final widths of the 50 Ω and 100 Ω lines were 0.75 mm 0.22 mm.

The next item to be optimized was the matching line between the 100 Ω line and the patch. A similar approach was used, as described in the single radiating element design. However, for the optimization of the matching line using IE3D software, an additional length of transmission line, as shown in Figure 18, was added between the port and the matching line to take into account the field interactions at the intersection. This is an improvement from the design of the single element.

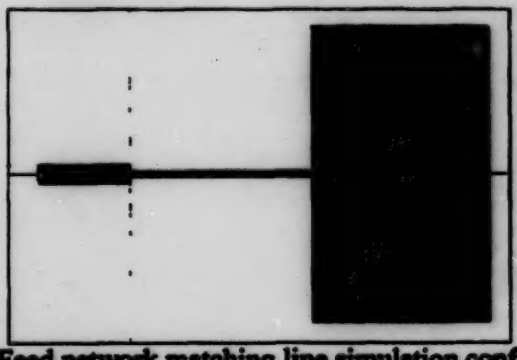

Figure 18: Feed network matching line simulation configuration

The final dimensions of the matching line are 2.04 mm x 0.065 mm, shown in Figure 19. The return loss is presented in Figure 20. It can be seen that matching performance was improved over that of the initial design.

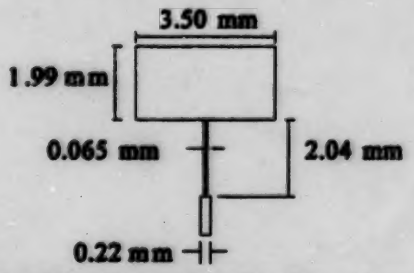

Figure 19: Matching line and patch dimensions

Figure 20: S11 of matching line for feed network configuration

The next items to optimize were the two-way power dividers. These are illustrated in Figure 21. Based on the equations provided by Lee and Chen [22], it is possible to calculate the initial dimensions for the divider.

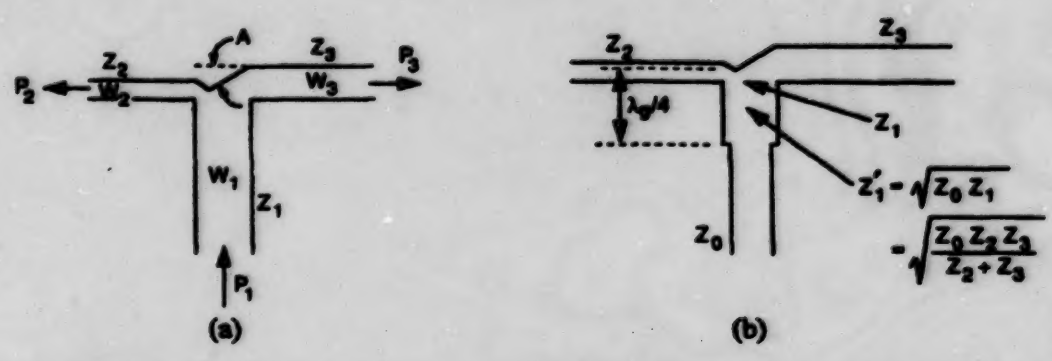

Figure 21: Power divider (a) without quarter-wave transformer (b) and with quarter-wave transformer.

In (a), $Z_1 = Z_2 \times Z_3 / (Z_2 + Z_3)$, which describes the 50 Ω to 100 Ω divider. In (b), the quarter wave transformer will provide the 100 Ω to 100 Ω divider. It is also possible to determine the angle A with the following equation:

$$A = \arctan\left(W_3 / W_1\right)$$

The final simulation results expected are –3 dB for S21 and S31, meaning that the power is effectively divided in two, and at least –25 dB for the return loss S11. After going through manual optimization using IE3D for the 50 Ω to 100 Ω divider, the dimensions and the simulation results are shown in Figures 22 and 23. The S21 and S31 simulation results are overlapping near –3 dB.

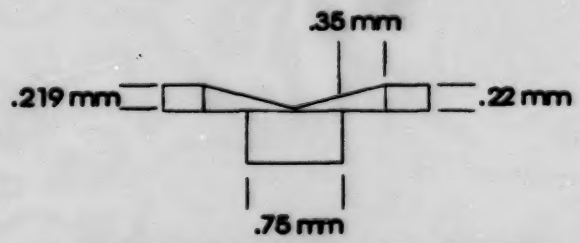

Figure 22: 50 Ω to 100 Ω divider dimensions

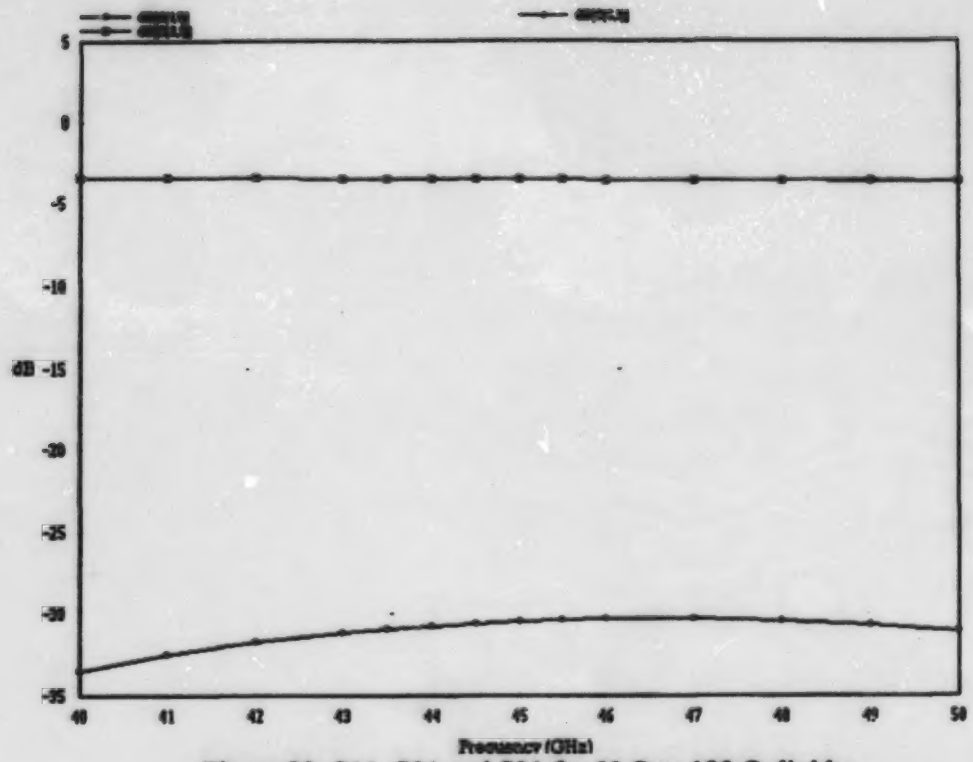

Figure 23: S11, S21 and S31 for 50 Ω to 100 Ω divider

The dimensions and the simulation results for the 100 Ω to 100 Ω divider are shown in Figures 24 and 25. As with the 50 Ω divider, the S21 and S31 results are overlapping.

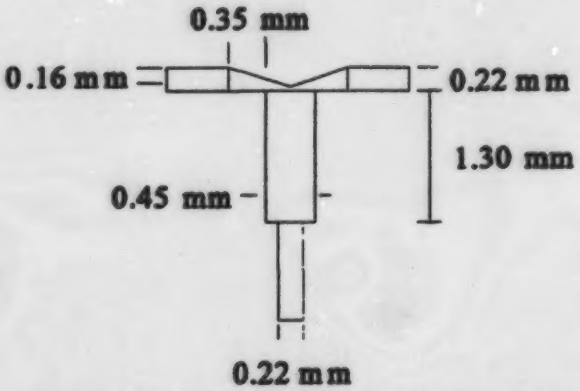

Figure 24: 100 Ω to 100 Ω divider dimensions

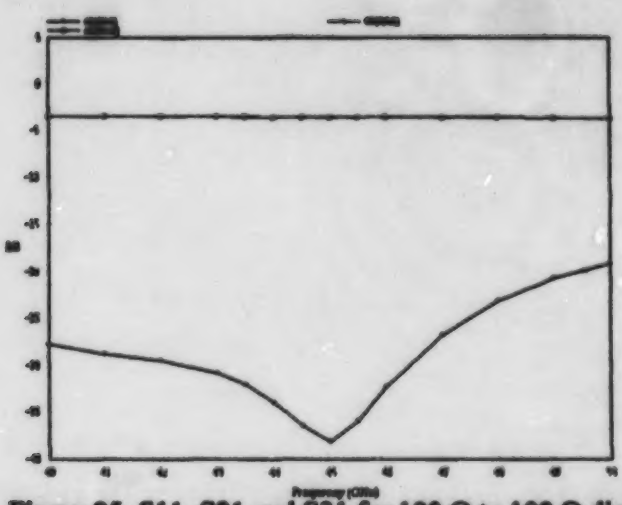

Figure 25: S11, S21 and S31 for 100 Ω to 100 Ω divider

The next step was to optimize the 90° bend in the 100 Ω transmission line. A formula is available for the optimally mitered 90° bend in microstrip for the defined range [23]:

$$f_r \le \frac{15}{h(mm)}(GHz)$$

$$2.5 \le \epsilon_r \le 25$$

$$angle = 90°$$

$$0.5 \le \frac{W}{h} \le 2.75$$

f_r = frequency of operation
h = dielectric thickness
ϵ_r = relative dielectric constant
W = width of the line

In this case, the condition on the substrate dielectric constant is not adhered to, for the dielectric used, $\epsilon_r = 2.17$ is below the range specified. The optimum miter formula was still used for an approximation, and manual optimization was done using IE3D. Based on Figure 26, the formula is:

$$\frac{X}{D} = 0.52 + 0.65e^{-1.35\frac{D}{h}}$$

Figure 26: Mitered 90° bend

Figures 27 and 28 show the optimized dimensions and S parameters of the 90° bend in 100 Ω line.

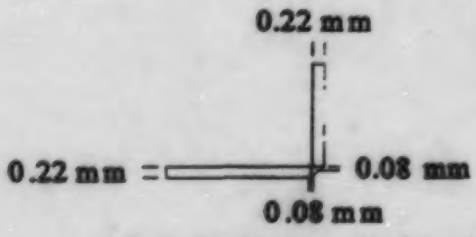

Figure 27: Optimized 90° bend

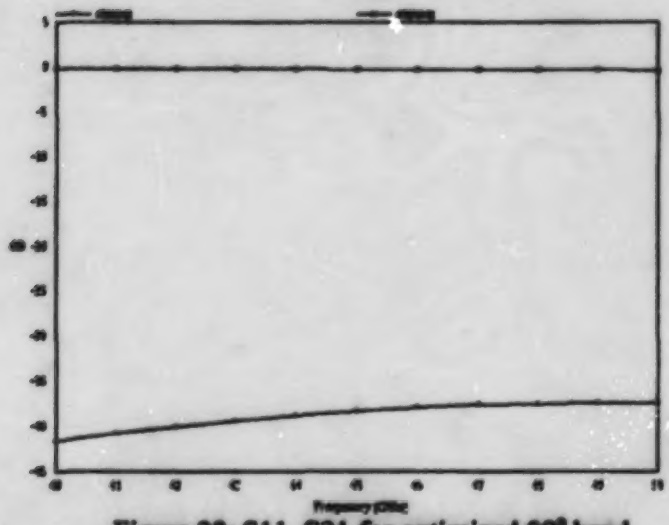

Figure 28: S11, S21 for optimized 90° bend

Three other bends exist in the feed network; these are a 51.5° bends. Their locations and implementation are shown in Figure 29. A simulation was performed by joining the corners of the transmission line with a straight line. The results obtained were acceptable. For the 50 Ω line, S11 was under -25 dB and for the 100 Ω, S11 was under -35 dB, for a frequency range from 40 GHz to 50 GHz, as shown in Figure 30.

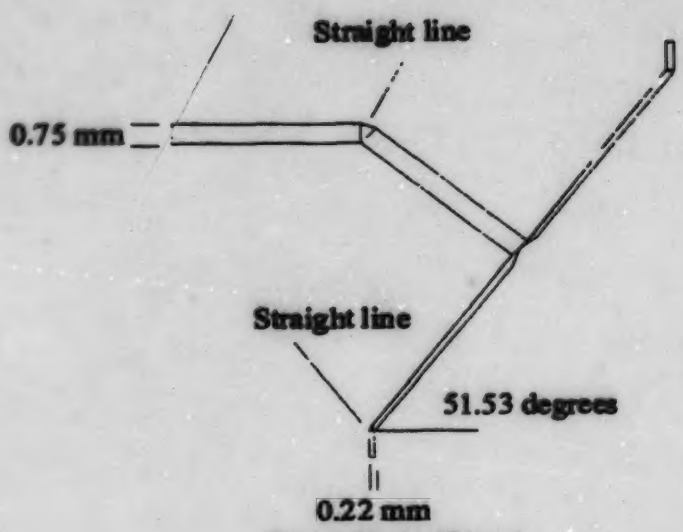

Figure 29: 51.5° bend

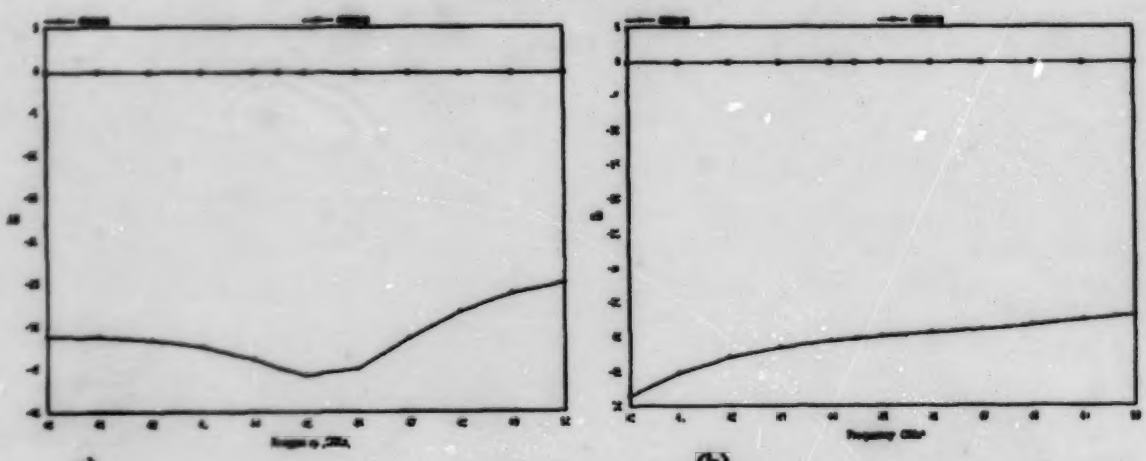

a) (b)

Figure 30: S11 and S21 for 51.5° bend for (a) 50 Ω line (b) 100 Ω line

The last configuration to be simulated was the entire feed network combining all the optimized components, shown in Figure 31. The distance between each microstrip patch radiating element is 3λ, which is 20.22 mm. This was simulated using IE3D and the return loss characteristic is shown in Figure 32. This completed the array design, and the simulation results were acceptable.

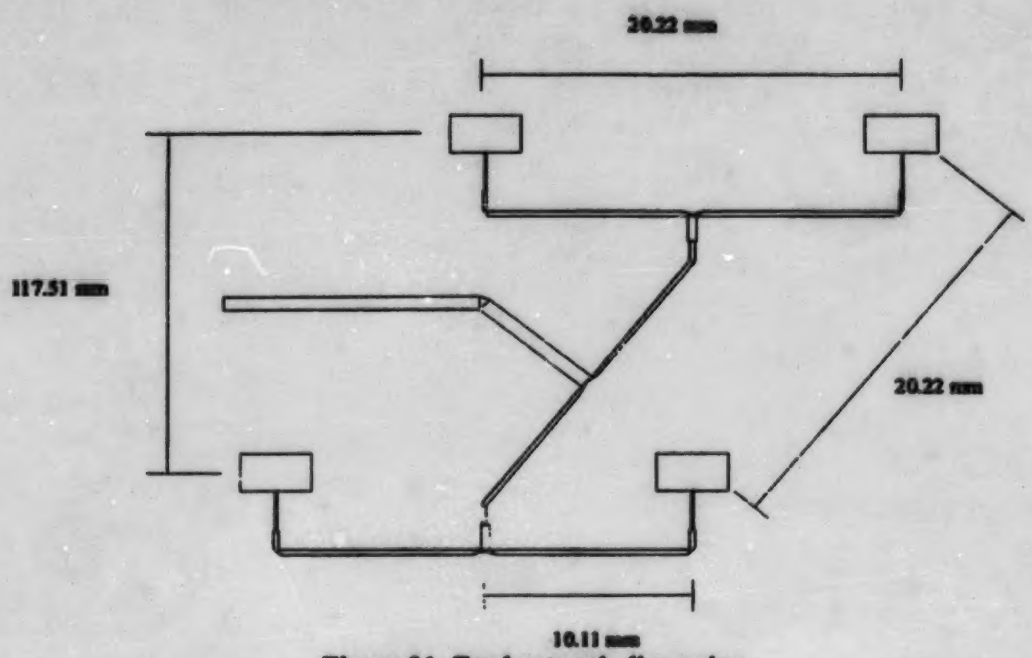

Figure 31: Feed network dimension

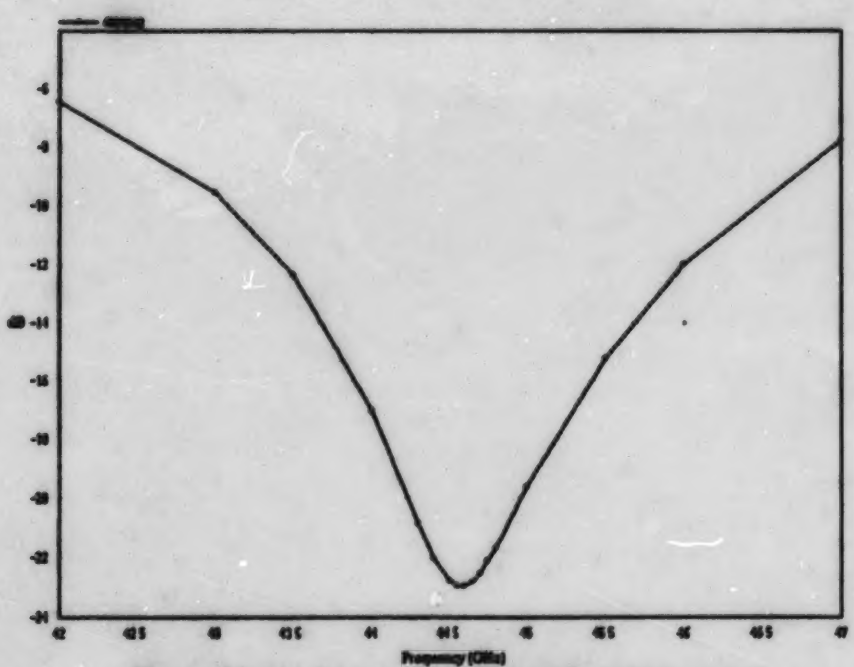

Figure 32: S11 for complete microstrip antenna array

3.5 Lens

Lenses were designed using Rexolite dielectric material having a relative dielectric constant of 2.53. Based on the lens equations presented in the theory chapter, the four lens types were designed. They were simulated using HFSS simulation software. Comparioon of simulation results illustrated the advantages and disadvantages of each lens type. To validate the simulation results, one of the types of lenses was designed, simulated, fabricated and measured in the laboratory. Comparison between simulations and measurements was conducted. A four-lens array was designed, built and combined with the four-microstrip patch array for laboratory measurements.

3.5.1 Design of four lens types

Using the Matlab software, program files were developed based on geometrical optics lens equations to determine lens curvatures for the various types. The program files are presented in Appendix A.

Common parameters were required to be able to compare the lenses. The diameter of the lens is directly related to the element spacing of the microstrip array. The lens diameter is 20.2108 mm. The second common parameter chosen was the distance between the focal point and the maximum outer surface point of the lens, based on the geometrical equations. The distance is 21.1645 mm. Lens data are presented in Table 4 and shapes in Figure 33. Data points of the curvatures are available in Appendix B. In Table 4, "Theta max" is the angle from the focal point, z = 0 mm, to the edge of the lens at y = 10.1054 mm, "Inner length" is the distance from the focal point to the inner, first, surface of the lens on the z axis, and "Outer length" is the distance from the focal point to the outer, second, surface of the lens on the z axis, which is z = 21.1645 mm. These distances are shown in Figure 33.

Plano-convex:		Meniscus:	
Dielectric constant:	2.53	Dielectric constant :	2.53
Theta max:	25.523 degree	Theta max:	51.0461 degree
Inner length:	17.2892 mm	Inner length:	12.9948 mm
Lens Thickness:	3.8753 mm	Lens Thickness:	8.1697 mm
Outer length:	21.1645 mm	Outer length:	21.1645 mm
Diameter:	20.2108 mm	Diameter:	20.2108 mm
Straight face:		Conventional:	
Dielectric constant:	2.53	Dielectric constant:	2.53
Theta max:	31.8167 degree	Theta max:	27.1939 degree
Inner length:	16.28775 mm	Radius 1:	22.1123
Lens Thickness:	4.87675 mm	Radius 2:	22.1123
Outer length:	21.1645 mm	Inner length:	16.2761 mm
Diameter:	20.2108 mm	Lens Thickness:	4.8884 mm
		Outer length:	21.1645 mm
		Diameter:	20.2108 mm

Table 4: Lens design specifications

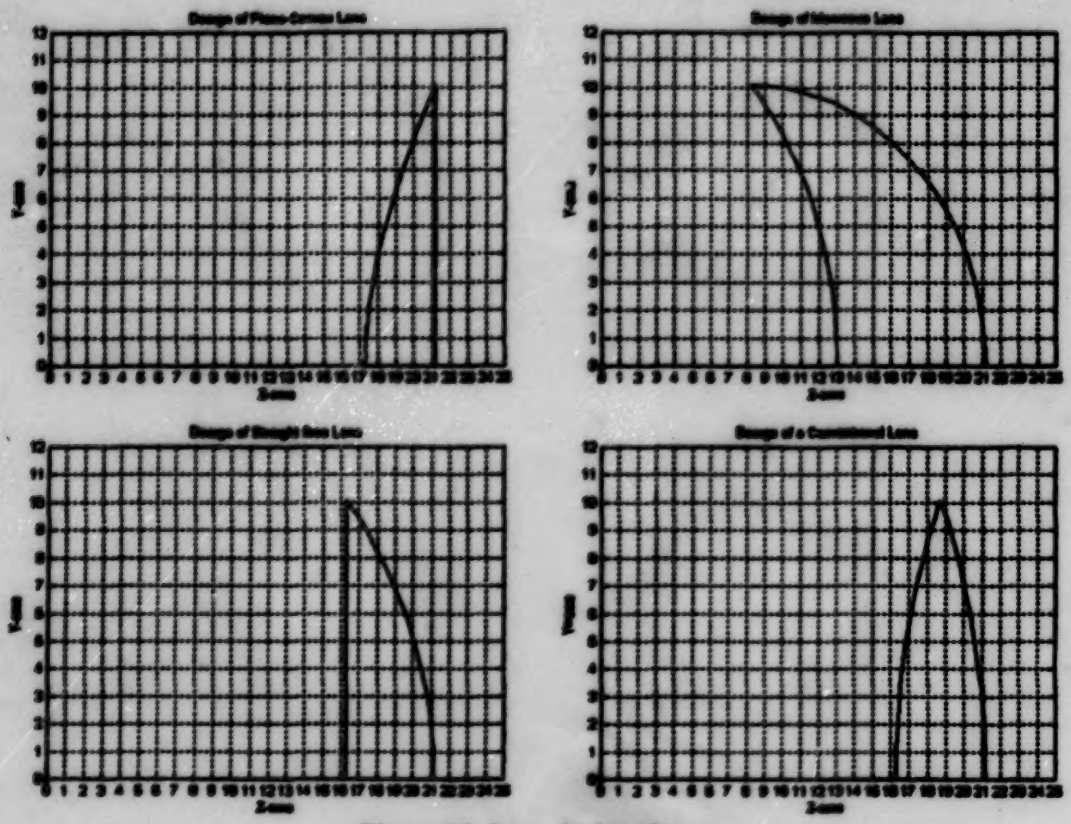

Figure 33: Lens design shapes

These are the four lens designs that were simulated using HFSS software.

3.5.2 Design of prototypes

To be able to validate the simulations, a prototype of the straight face lens, designed as Prototype 1, was designed, built and measured. This first prototype was designed before the microstrip patch array was designed. The exact spacing of the elements was unknown at that time. The diameter of the lens was selected based on the fact that the diameter would be in the 20 mm range. This model was simulated including as much of the support structure as possible.

The prototype specifications are described in Table 5 and in Appendix B.

Straight Face Lens (for prototype 1):	
Dielectric constant of lens:	2.53
Theta max:	approx 36°
Inner length:	15 mm
Lens Thickness:	6 mm
Outer length:	21 mm
Diameter:	20.075 mm

Table 5: Prototype 1 specifications

A support structure was required to maintain the lens in the proper position. The design of the support structure was done to minimize the effect at the edge of the lens by tapering the thickness to only 1 mm.

By trying to properly represent the support structure, a simulation model was designed. Due to computer memory and simulation software limitations, only a small section of the support structure could be included in the simulation. The elements of the HFSS simulation are shown in Figure 34. The full lens mechanical design is shown in Figure 35. Prototype 1 was extensively measured in the laboratory.

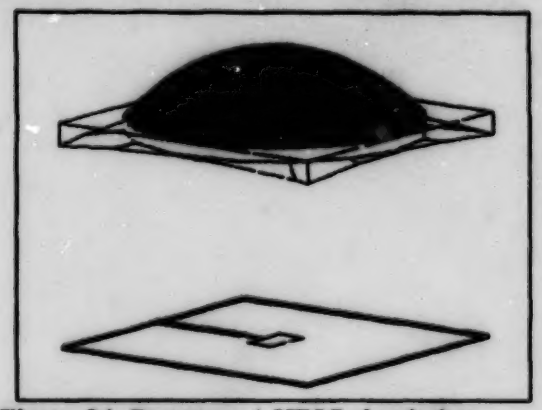

Figure 34: Prototype 1 HFSS simulation

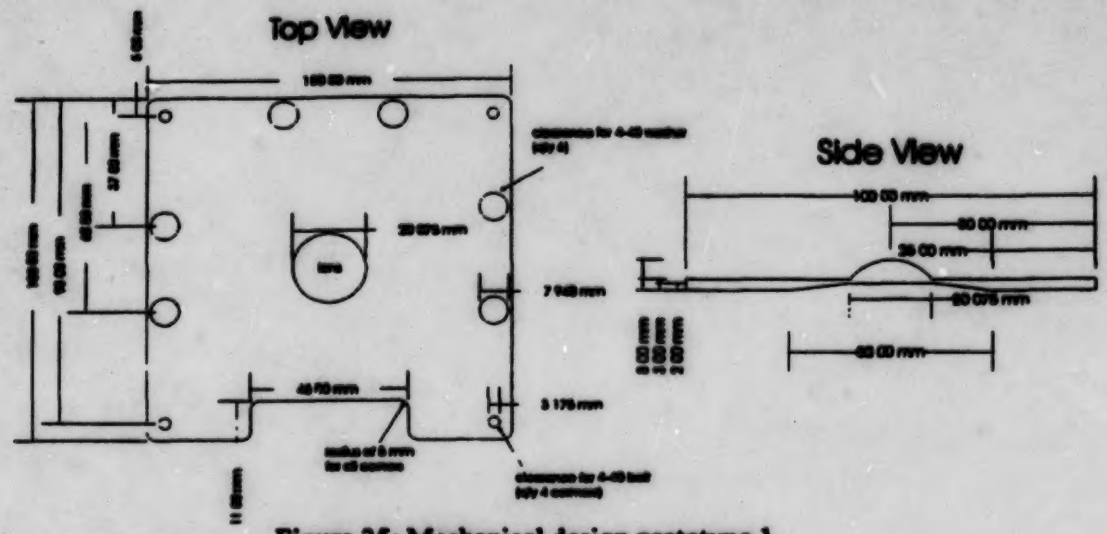

Figure 35: Mechanical design prototype 1

A second single lens prototype was designed based on the dimension of the lens required for the array. The data was extracted from Table 4 for the straight face lens. The differences from prototype 1 were the lens diameter and thickness; the support structure was the same. To simplify the design procedure, the 1mm thickness of support structure was added to the lens thickness. The effect was to locate the focal point at a different distance, which had to be determined. The mechanical design of the second prototype is shown in Figure 36.

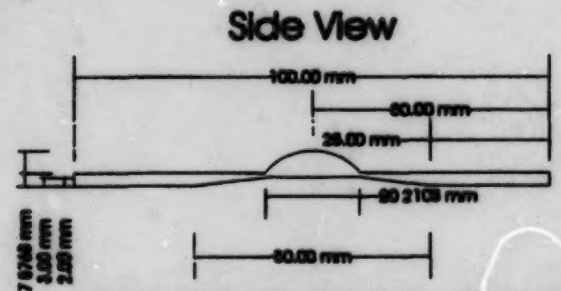

Figure 36: Mechanical design prototype 2

The third prototype was the design of the four-lens array, shown in Figure 37. The dimensions of the individual lenses were the same as in prototype 2. The location of the lenses is based on the microstrip array. The lens specifications are provided in Table 4 for the straight lens. Appendix B provides the detailed lens design for prototypes 2 and 3.

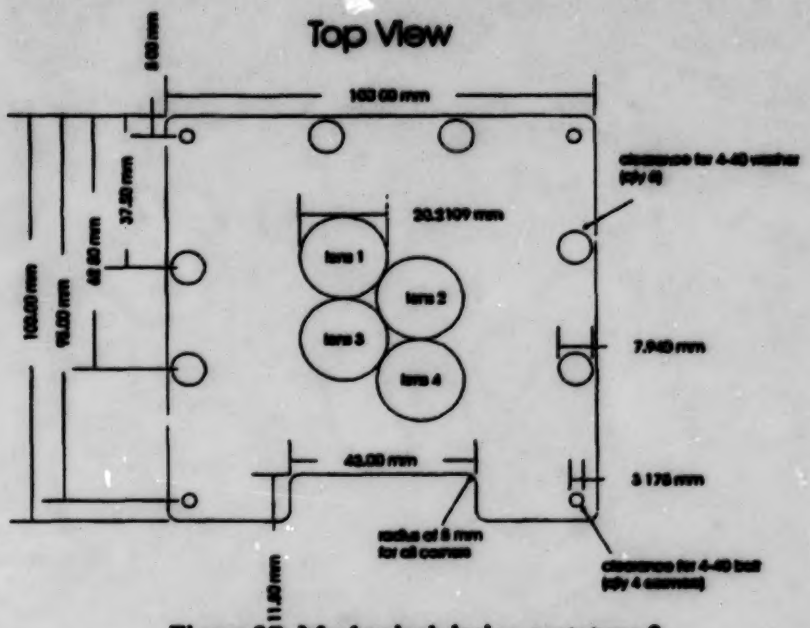

Figure 37: Mechanical design prototype 3

A fourth prototype was designed to allow lab measurements of a meniscus lens. The lens specifications are provided in Table 4 for the meniscus lens. Appendix B provides also detailed lens design for prototype 4. The same support structure as for prototype 1 was used.

The design of the following various components, the single element, the 4-element array, the single lens prototypes and an array of four lenses, was completed. The next step was to fabricate and measure the components. The next chapter presents both the simulation and the measurement results.

CHAPTER 4: RESULTS

Results will be presented in the order detailed below. The single patch, including the simulation and the measurement results is presented. Then the results of simulations using HFSS for the four lens types are discussed. Following this is a presentation of the simulation results and the extended measurement results of prototype 1. The next results to be shown are the microstrip patch array, both simulation and measurement results. A brief results section is presented on prototype 2, which is the same single lens dimensions and support structure configuration used for the lens array. Finally the results of the patch array combined with the lens array are presented as prototype 3.

4.1 Physical Installations and Set-up

Before any experimental results could be obtained, prototypes had to be manufactured and measured.

4.1.1 Experimental facilities

All manufacturing of the microstrip circuits and dielectric lenses was carried out in the Communications Research Center (CRC) model shop facility. All RF measurements were done in the DDARLing laboratory facility, under the supervision of a qualified technician.

The DDARLing laboratory antenna measurement setup is presented in the following figure. For S11 measurements, only the Wiltron 360B vector network analyzer is required.

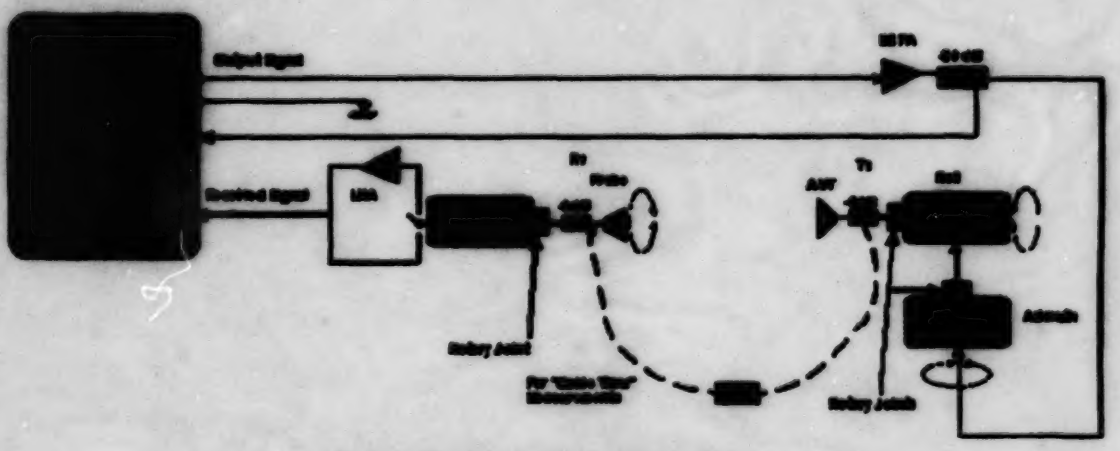

Figure 38: RF measurement setup

4.1.2 Experimental mounting

For the mounting of the microstrip circuits a 100x100 mm metal frame was used. The substrate was held to the frame by 12 nylon screws. To insure a better ground connection between the ground plane of the substrate and the frame a plexiglass bridge was used to apply pressure on the substrate. The lens was maintained above the microstrip radiating element using the four corner screws with a piece of compressible

foam between the lens support structure and the substrate. The height of the lens was adjusted manually by turning each of the screws. Distances between the lens and the radiating element were measured using a caliber and averaging the four corner distances.

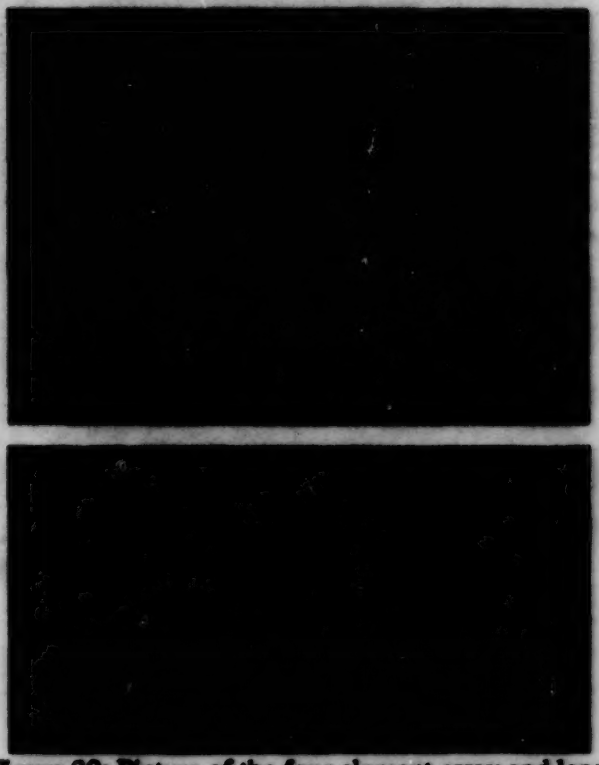

Figure 39: Picture of the four element array and lenses

4.2 Single Radiating Element

The first result to be presented for the patch is the laboratory measurement of return loss, S_{11}, in Figure 40. Two measurements are presented in the figure, the solid line is the gated S_{11} measurement. The term "gated" means that the reflection at the connector has been removed using Time Domain Reflection (TDR) technique available in the Wiltron 360B Vector Network Analyzer.

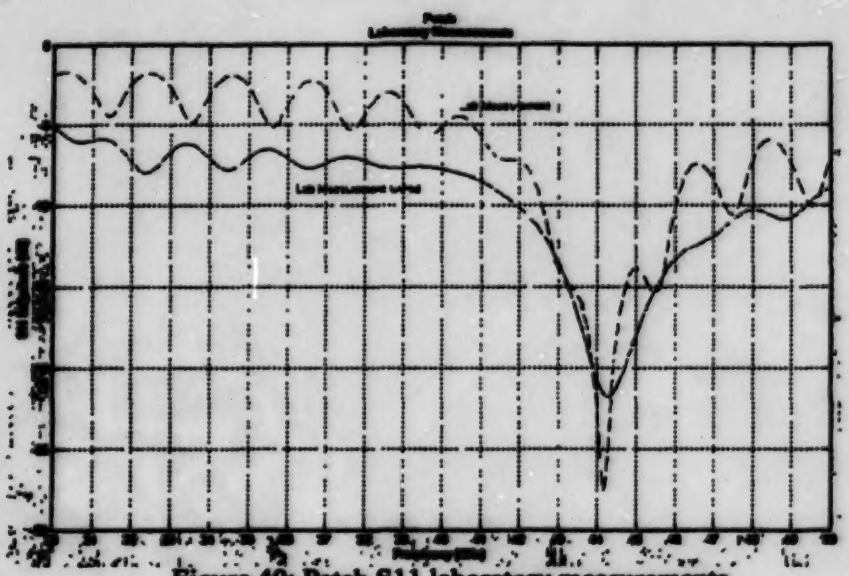

Figure 40: Patch S11 laboratory measurements

The comparison between the IE3D simulation and the measurement values is done using the gated S_{11}, since the simulation software does not take into account the connector. In Figure 41, the important aspect to look at is the resonant frequency, which is close to 44.5 GHz, as predicted. The difference away from the resonant frequency is due to the fact that the simulation was done using a feed line of 6 mm length and the physical model has a feed line length of 50 mm. This greatly increased loss results in an apparent improvement in S_{11} over the simulated results.

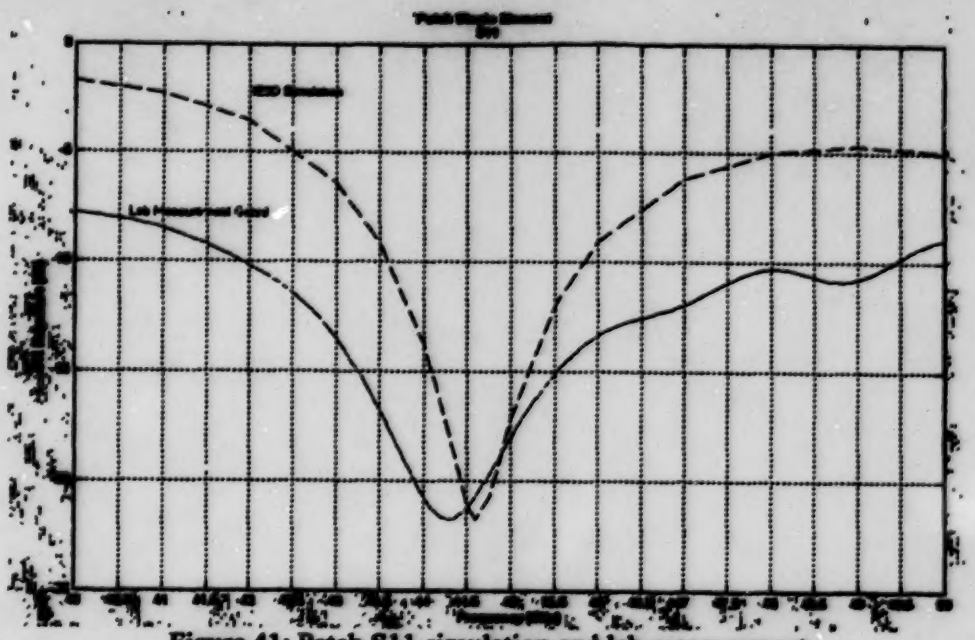

Figure 41: Patch S11 simulation and lab measurement

The next aspect to look at is the radiation patterns of a single element. Initial results from the laboratory showed significant ripples, especially in the E plane, phi=90°, which were not present in the simulation patterns. After investigation, using the angle measurement between two ripples, it was found that the edges of the plexiglass bridge region, used to provide the good ground contact near the launching area and the region near the connector, were the major problems. The average angle between two ripple maxima was 9°. Knowing that the wavelength is 6.7369 mm, using geometry it is possible to determine the distance d between two sources generating a constructive signal. Figure 42 presents the required parameters with 1 and 2 being element 1 and element 2.

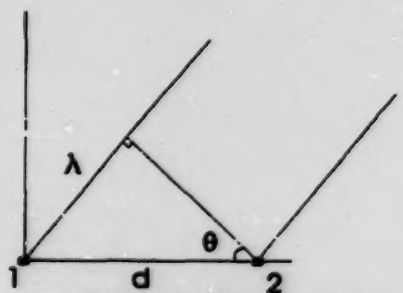

Figure 42: Ripple analysis

In this case, using the equation

$$d = \frac{\lambda}{\sin\theta}$$

The distance d was calculated to be 43.01 mm, which is within 1 mm of the distance between the center of the patch and the edge of the plexiglass.

RF absorbing material was attached to the support structure so that it covered the edges of the substrate and the plexiglass bridge. For the single patch and single lens, the material was 16 mm thick and the tapered hole in the center to expose the lens was 28 mm in diameter at its narrow point. Also an extra 16 mm was placed over the plexiglass bridge. An 80 mm square hole in 28 mm thick material was used for the array. Results showed improvements. Radiation patterns are presented in Figures 43 and 44.

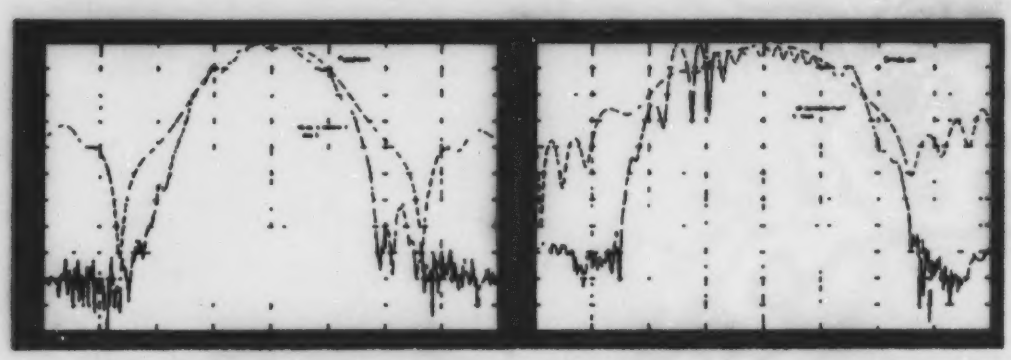

Figure 43: Patch radiation patterns, simulation and measurement with no mask, phi=0° and phi=90°

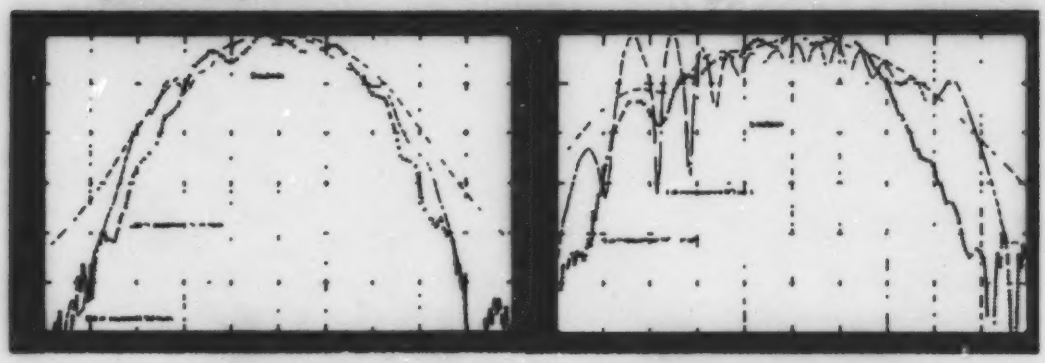

Figure 44: Patch radiation patterns, simulation and measurement with and without mask, phi=0° and phi=90°

By introducing the absorbing mask, it is evident that radiation from the edges was attenuated, but the scanning angle where the patch can be seen from the probe is also reduced due to the thickness of the mask.

Results presented in the two previous figures show acceptable agreement for radiation patterns between the simulation and measurement, especially when the mask is added. The next step was to look at the gain of the patch.

From the simulation the maximum gain was 8.3 dB, as shown in Figure 45.

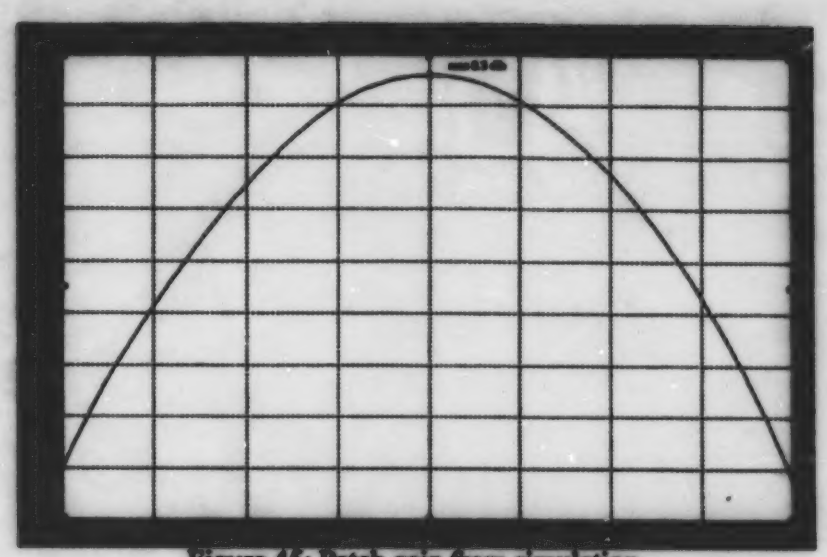

Figure 45: Patch gain from simulation

From the laboratory measurement, the gain was calculated using the gain comparison technique. By comparing the signal received using the antenna under test (AUT) to the signal received using an antenna having a known gain, the gain of the AUT can be determined. The gain was measured for a frequency range of 43.5 to 45.5 GHz. A value of 5.1 dB was found for the gain at 44.5 GHz, as shown in Figure 46.

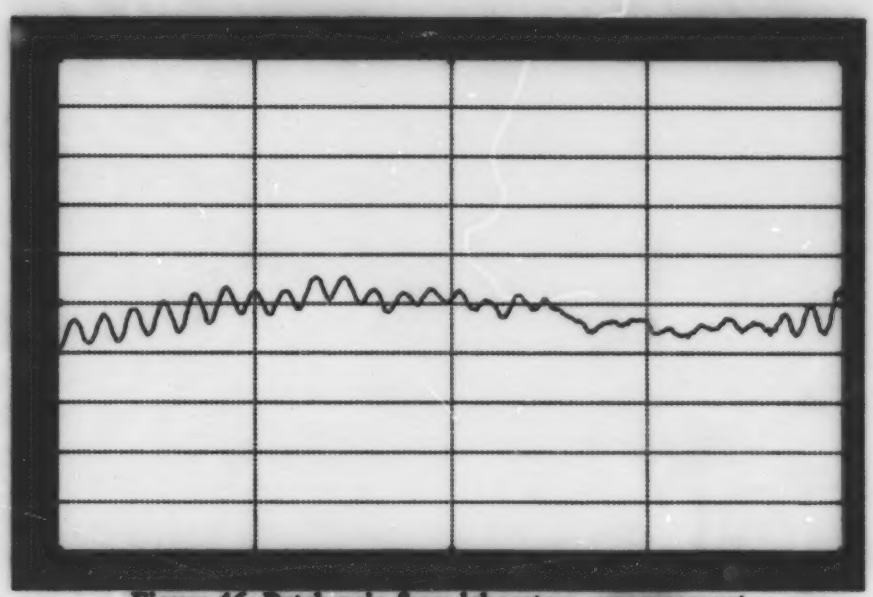

Figure 46: Patch gain from laboratory measurement

There is a difference in the gain of 3.2 dB between the simulation and the lab measurement. As mentioned before, the loss encountered by the feed network is

important at millimeter wave frequencies. To estimate the magnitude of the loss for a transmission line (TL), a 100mm long 50 Ω line (0.819mm wide) TL prototype was built and measured. The measured loss at 44.5 GHz, shown in Figure 47, was found to be 4.3 dB. Since the single element patch is located 50 mm from the launcher, the measured feed line loss is taken to be 2.15 dB. Extra loss has to be included for the discontinuity of the feed line and because of the narrower matching line, which will introduce more loss per distance than the 50Ω line. Also the loss due to the patch itself has to be considered.

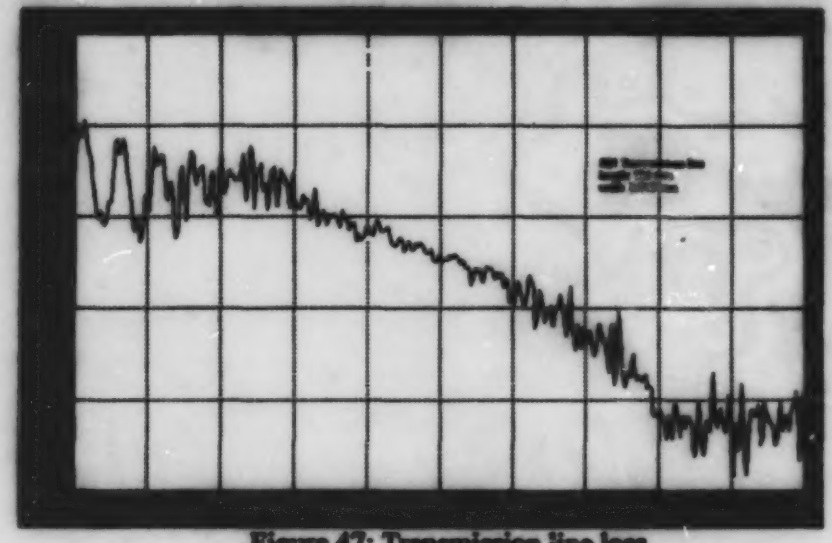

Figure 47: Transmission line loss

From this comparison between the measurements and the simulation, the results for the single patch radiating element are considered to be acceptable.

4.3 Simulation of Four Lens Types

As described in the design chapter, four lenses, having as common criteria their diameters and the same distance between the geometrical optics (GO) focal point and the top of the lens, were compared by simulation.

It was expected that the GO focal point might not be at the same location as the physical optics (PO) focal point. The GO focal point is located at 16.29 mm from the bottom of the lens. To determine the PO focal point using HFSS simulation software, a plane wave was assumed incident on the top of the lens, and passing through to the bottom. In physical optics, the electrical field does not focus at one point, but in a region. These regions are obvious for the various types of lens in Figure 48. The electrical field is represented in color, ranging from red for denser field to blue for non-existent field.

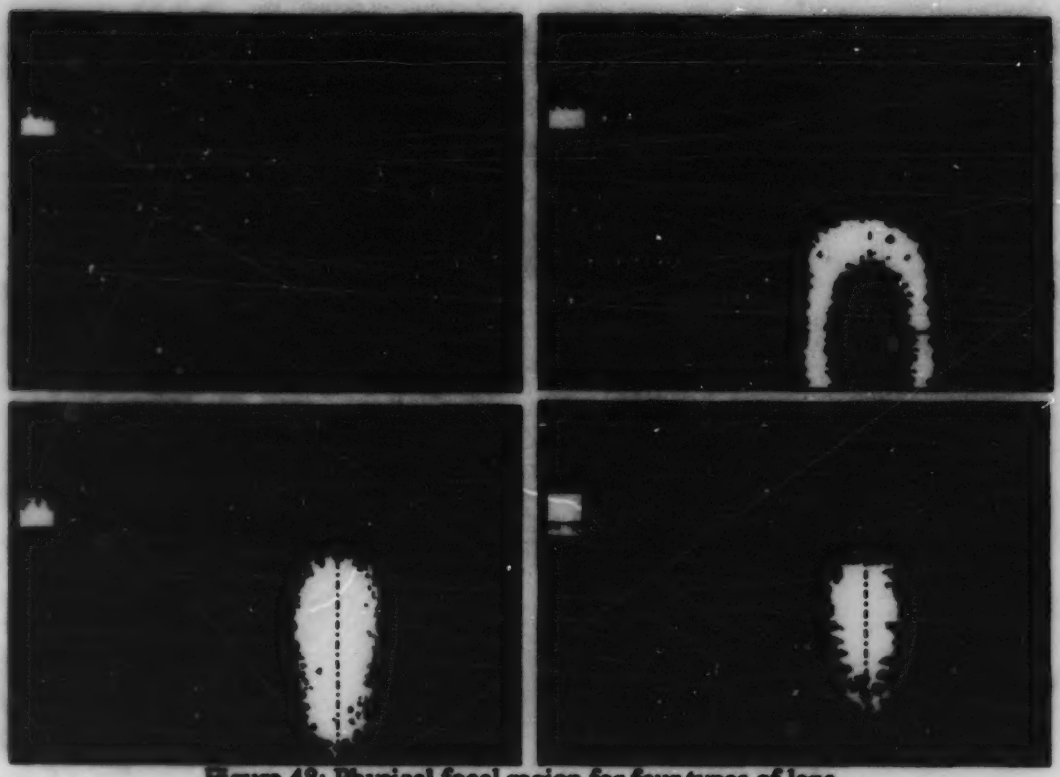

Figure 48: Physical focal region for four types of lens

From this figure, it can be observed that a focal region can be determined for each type of lens. The meniscus lens was found to focus a more intense electrical field than all the other types. On the other hand, the plano-convex lens seemed to be less efficient. However, it has to be noticed that this comparison is for a plane wave coming from the top of the lens. It does not predict the performance of the lens with a radiating element at the focal point located below the lens due to possible reflection problems. Except for the meniscus lens, the three other types were found to have a focal region located above the predicted geometrical focal point as determined in Figure 48 by the z and y axis origin location.

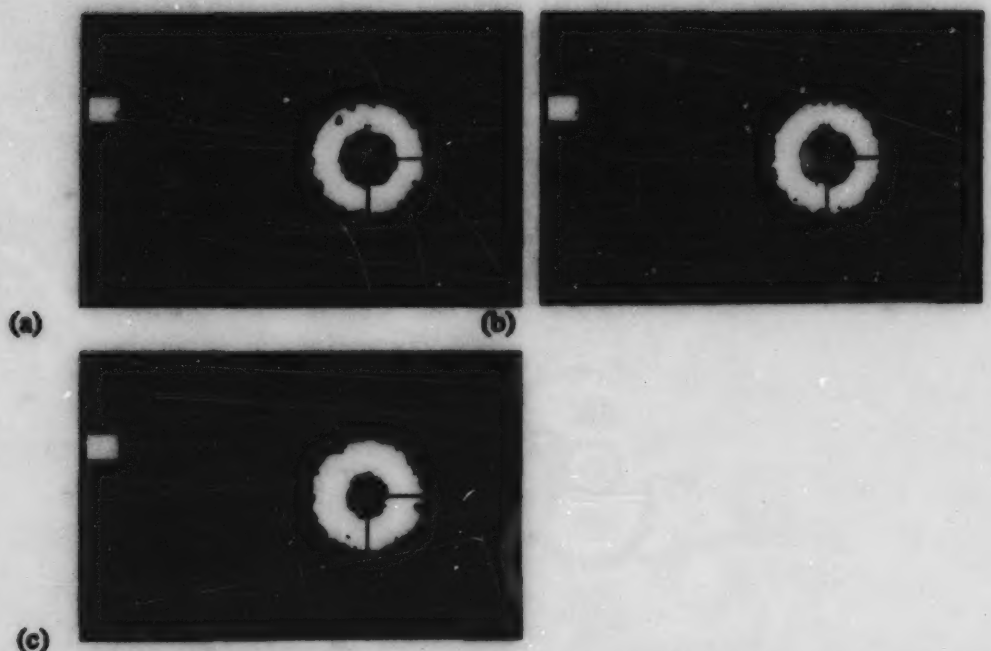

Figure 49: Focal point, in plane XY, distance from bottom of the meniscus lens (a) at 12.99 mm (b) 11.99 mm (c) 9.99 mm

To select a specific point to locate the radiating element, cuts in the XY plane were done to observe the cross-section of the focal region. The XY cuts are presented for the meniscus lens in Figure 49.

The same types of cuts were analyzed for the other types of lenses and the final choice for the location of the patch radiating element for each lens types was made from these cuts. The location of the patch is given as the distance above the axis origin, i.e. the location of the theoretical GO focal point. The optimum XY cut, the one having the best focus, was selected to be the one having the highest energy density based on color code. Other factors, like the symmetry of the field, were also considered.

Lens Types	Distance of PO focal point from GO focal point (mm)
Plano-convex	11.0
Meniscus	0.0
Straight face	8.0
Conventional	9.9

Table 6: Location of radiating patch element

The remaining analysis required for the lens types was the radiation patterns using the designed rectangular patch at the locations of the focal points suggested in Table 6 above. Results are presented in Figure 50. These radiation patterns are the baseline used to compare the lens types.

At this point it is important to mention that the normal lens comparison based on the F/D ratio, focal length-to-lens diameter ratio, was not used to compare lenses. Initially, by using thin lens theory, the assumption was that the focal length and the lens diameter would have been the same for all the lens types. However, it can be observed that the thickness of the lens is not negligible compared to the focal length. Thick lens theory was then be required to determine the GO focal length. However, by using the plane wave technique, a PO focal point was determined. It is that last focal point that was used to locate the radiating element. The difficulty at this point was to determine what the PO focal length for each of the lenses was. Some options were available, either taking the focal length distance from the top or the bottom of the lens or taking the measurement at the center of the lens. By placing the radiating element at the PO focal point and by measuring the distance to the inner surface and to the outer surface of the lens, an F/D ratio was determined and is presented in Table 7.

Lens Types	Inner F/D ratio	Outer F/D ratio
Plano-convex	0.312	0.504
Meniscus	0.644	1.050
Straight face	0.411	0.653
Conventional	0.316	0.559

Table 7: F/D ratio for lens shapes

The meniscus lens has both the inner and outer larger F/D ratio. For all the other lenses, the F/D ratio, for the inner or the outer surfaces, was within 0.15.

(a) Plano-convex lens

(b) Meniscus lens

(c) Straight Face lens

(d) Conventional lens

Figure 50: HFSS simulation radiation patterns for four lens types

4.4 Prototype 1 - Single Straight Face Lens

To validate the radiation patterns for the four lens types, the simulation and measured results of a prototype were compared. As for the lenses, the focal region of Prototype 1 was determined using the plane wave technique. The result is presented in the next figure. From geometrical optics, the focal point was determined to be 15 mm from the bottom of the lens, located at the axis origin. From the simulation, shown in Figure 51, physical optics predicted a focal point 3.5 mm above the origin, for a focal length of 11.5 mm.

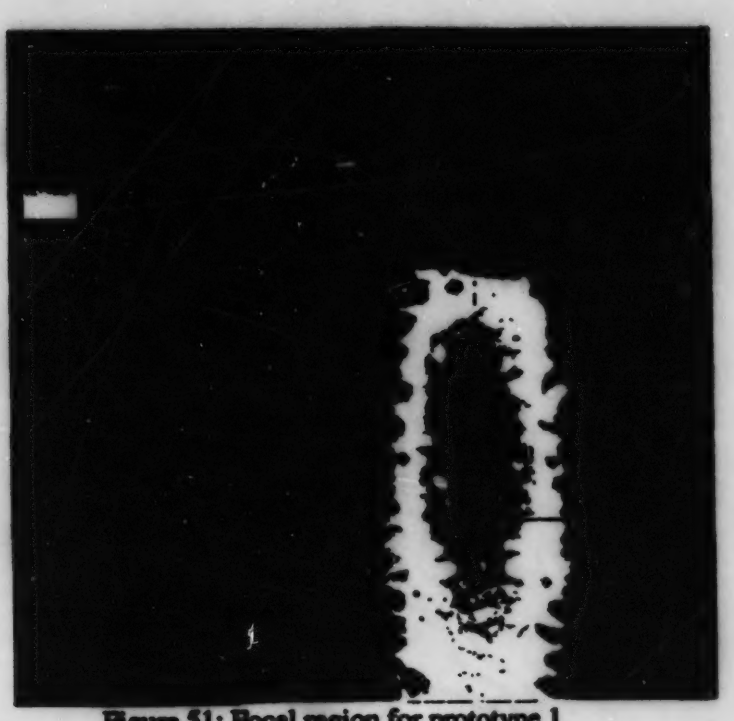

Figure 51: Focal region for prototype 1

For the prototype, radiation patterns were simulated with the lens located a 15 mm and 11.5 mm above the patch as presented in Figure 52. Improvement in the gain was expected for the second simulation, however results were in the same range. An initial possible explanation for having the same gain value is that the patch was still in the focusing region.

Figure 52: Radiation patterns for prototype 1 at various focal lengths

Comparison between simulated and measured radiation patterns was required to validate the simulation. These comparisons are presented in Figure 53. Similar problems

to those seen for the patch were expected because of edge effects. In the case of the lens it was even more critical since the simulation only included a small section of the support structure. After analyzing the measurement and simulation results, it was felt reasonable not to expect an exact agreement between the two, but it should be possible to expect some similar characteristics. One reason is that the simulation program HFSS operates with a radiation absorbtion box around the entire model in order to calculate the far field radiation patterns. The problem is that on the side of the box the radiation is coming from the patch only and on the top it is the combination of the patch and the lens. In the laboratory, the patch is completely covered with either the lens or the support structure. These physical differences could account for the pattern differences in the comparison.

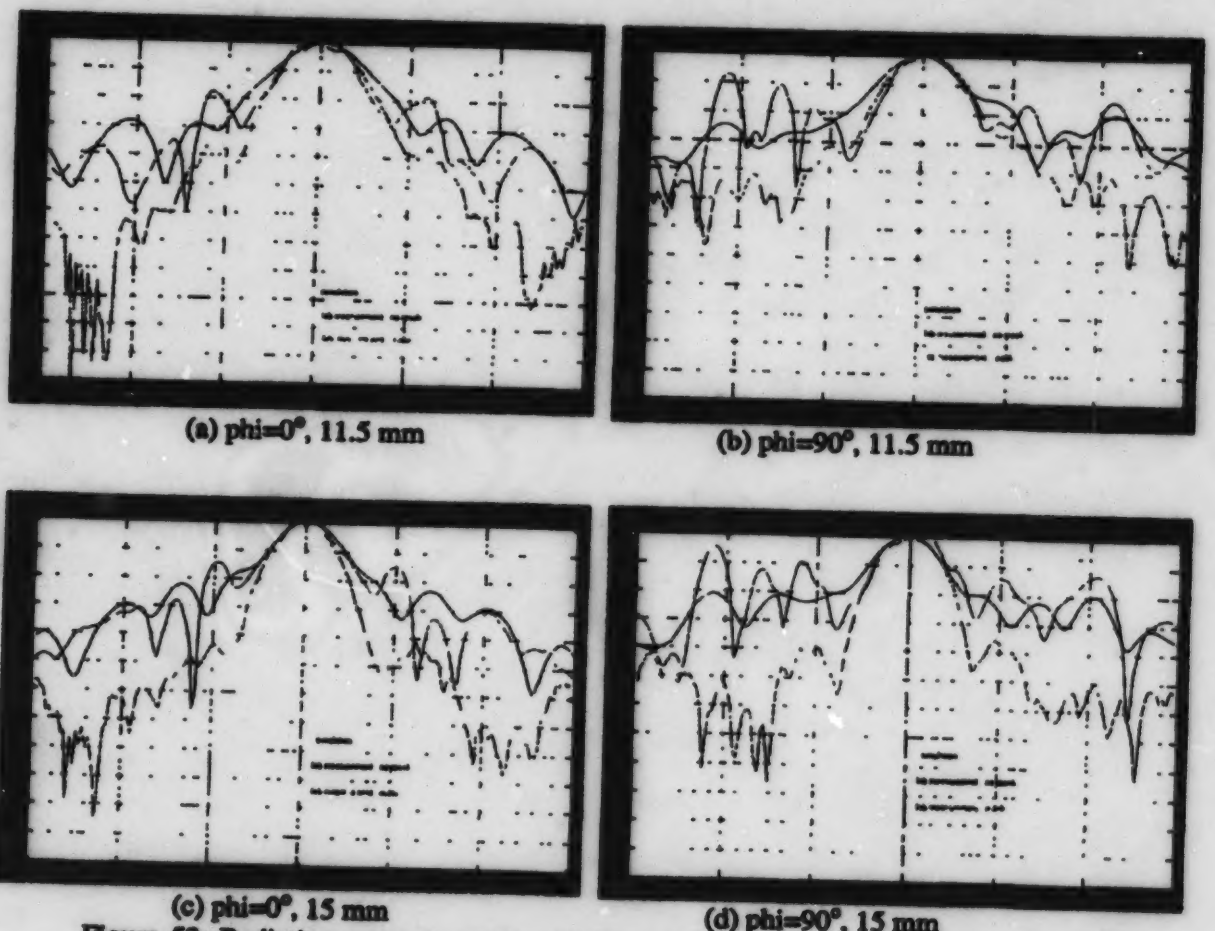

(a) phi=0°, 11.5 mm

(b) phi=90°, 11.5 mm

(c) phi=0°, 15 mm

(d) phi=90°, 15 mm

Figure 53: Radiation patterns, patch with lens, simulation and laboratory measurement with and without mask

It can be seen that for the main beam region, for boresight ±15°, simulation and measurements tend to agree with each other. It is more difficult to make comparison for the first null and first side lobe.

The last aspect to consider was the antenna gain with a lens installed. As for the single patch without lens, for the simulation the gain was taken from the antenna gain pattern at one frequency and for the laborstory measurement the gain was taken using gain comparison method over a range of frequencies. From Figures 54 and 55, the gain from the simulation is 15 dB and for the measurement it is 13.8 dB. Based on the same principles as for the single patch, the measured gain should be at least 2 dB lower due to the transmission line loss. However, this was not the case. This implied that the measured lens performance was apperently better than what was predicted by the simulation.

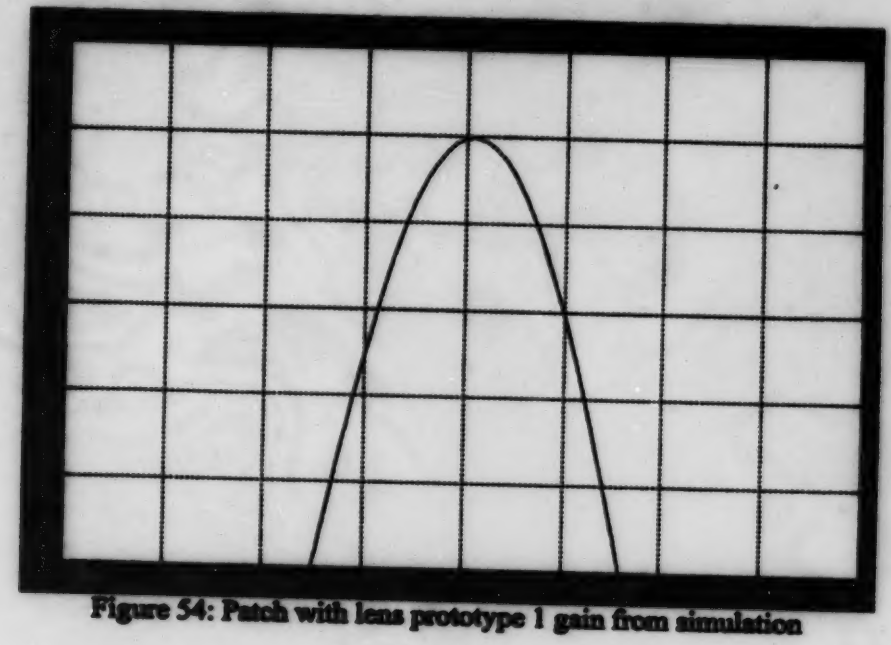

Figure 54: Patch with lens prototype 1 gain from simulation

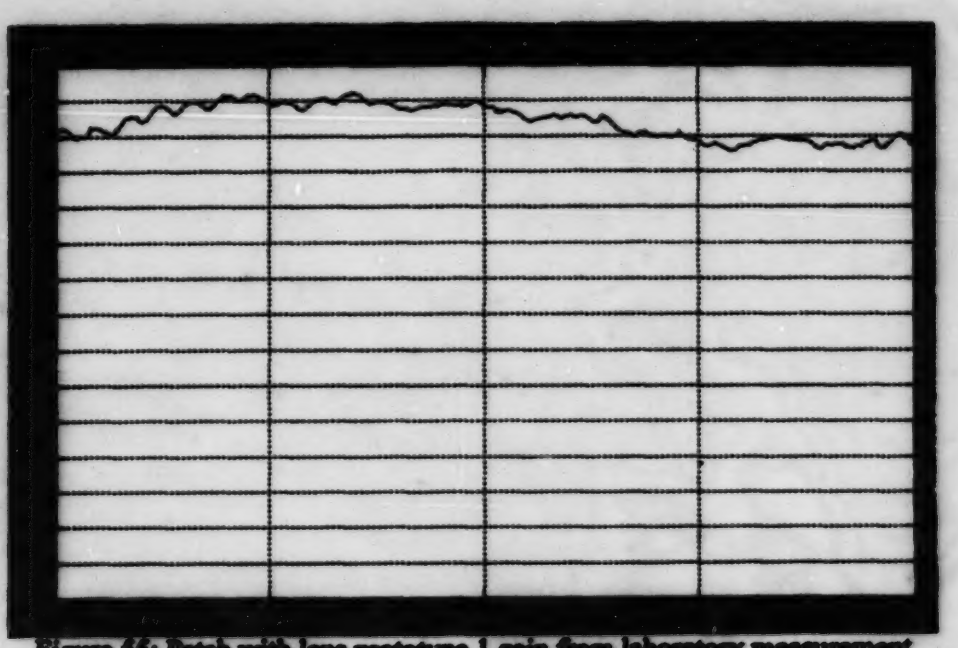

Figure 55: Patch with lens prototype 1 gain from laboratory measurement

4.4.1 Investigation of focusing region

With the prototype available, it was possible to experimentally evaluate the effect of changes to the lens-patch separation on the boresight gain measured. To do the same through simulation could have taken a few weeks of computer time. In the laboratory, the lens was located from a starting point of 20 mm from the patch and moved towards the patch in 0.3 mm increments. Measurement of S21 was taken at each lens position. The result obtained, as shown in Figure 56, was not expected.

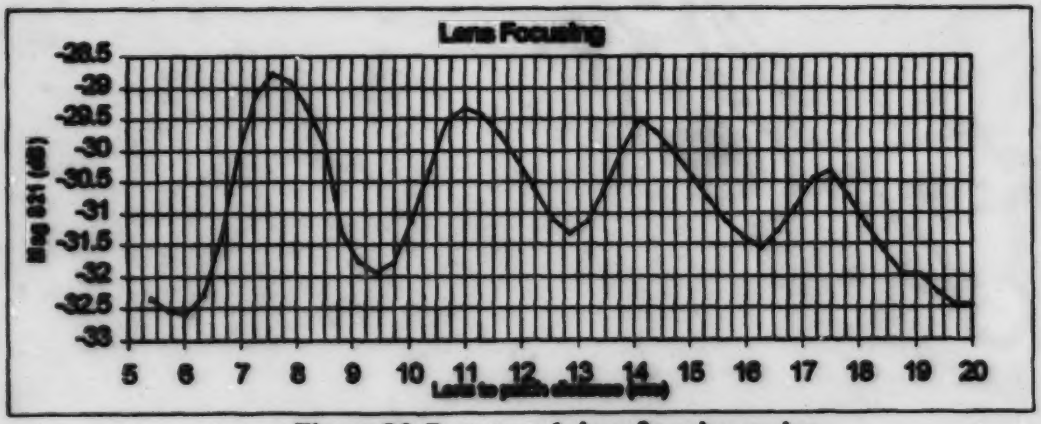

Figure 56: Prototype 1, lens focusing region

The expected result was only one maximum at the distance corresponding to the focal point. After investigation, it was found that the multiple maxima were due to reflection from the base of the lens to the substrate and back to the lens. The average distance between two maxima was 3.3 mm which is close to half a wavelength at 44.5 GHz. The best focal point was determined by drawing a line through the average of the points between an adjacent maximum and minimum. This provided an optimum focal point, if reflection was taken into account, in the range of 11.5 mm, similar to that predicted by the software. In order to further investigate this phenomenon, simulations were run for various distances and the result is shown in Figure 57, which also presents a fluctuation in gain as a function of the patch-to-lens distance.

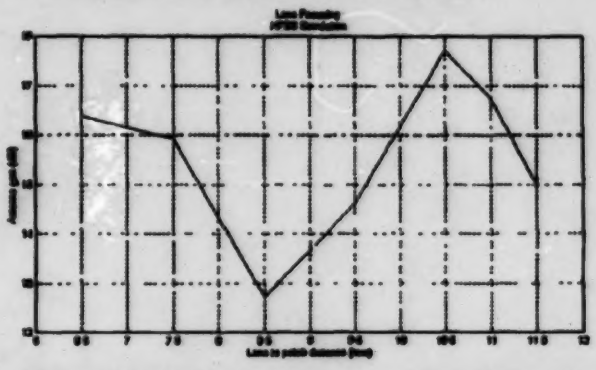

Figure 57: HFSS simulation, lens focusing region

4.5 Microstrip Element Array

Presentation of the results for the array follows the same procedure as with the single element. S_{11} results are presented first, then radiation patterns and finally the gain.

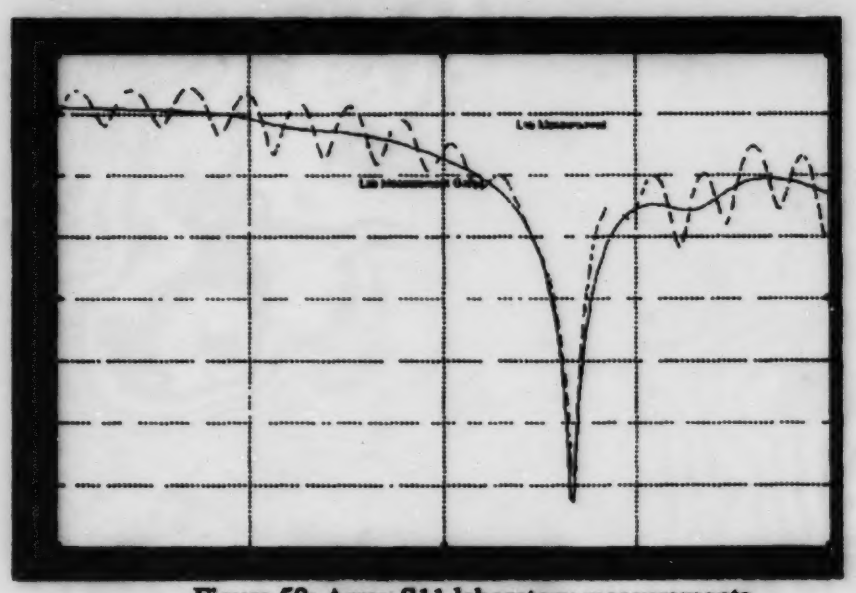

Figure 58: Array S11 laboratory measurements

The measured resonant frequency, in Figure 58, for the array is 43.5 GHz instead of 44.5 GHz according to the design specification. This is a difference of 2.2%. At 44.5 GHz, the array S_{11} is still below –12 dB allowing the array to be operational as an antenna. The difference in the resonant frequency is mainly due to fabrication tolerances since the design procedure was proven for a single element. From the CRC model shop, the fabrication tolerance is ±0.013mm. To illustrate the effect of manufacturing tolerances, Table 7 shows the characteristic impedance variation for the matching line located just before the patch. A change in the impedance of the line would modify the matching to the patch, degrading its performance at a specific frequency. By applying the tolerance to the patch directly, the resonant frequency would then be modified.

Line Width	Characteristic Impedance
- 0.013 mm: 0.052 mm	156.9 Ω
Design value: 0.065 mm	148.9 Ω
+0.013 mm: 0.078 mm	142.0 Ω

Table 8: Characteristic impedance variation for the matching line

As it was done for previous measurements, absorbing material was fixed on the edges of the support structure. Comparison of the radiation patterns between the measurement and the simulation, using ARPS, is presented in Figure 59.

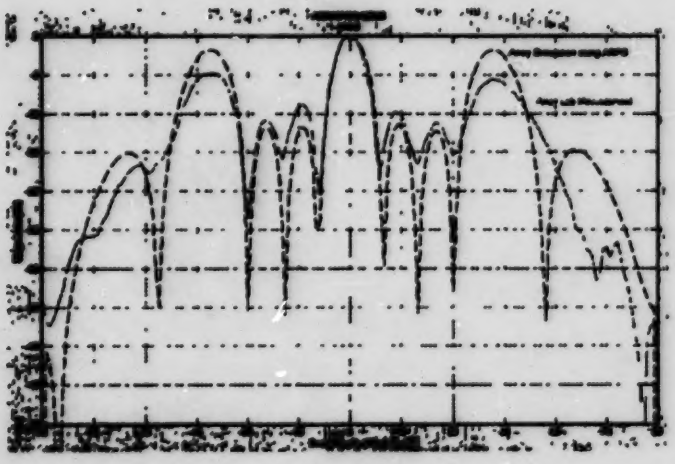

(a)

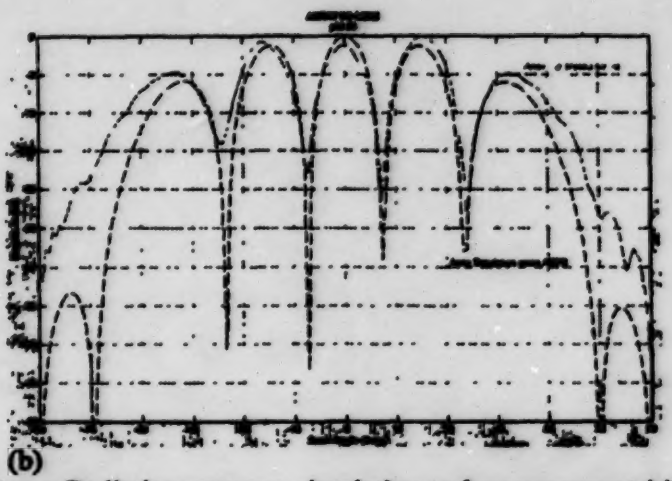

(b)

Figure 59: Array Radiation patterns, simulation and measurement (a) phi 0 (b) phi 90

It can be concluded from Figure 59 for the radiation patterns that the measurement results are in good agreement with the simulation.

The next step was to evaluate the gain of the array. The measured gain of the single patch, in the previous section was 5.1 dB. In theory, a four element array gain should be 6 dB higher. However, this does not take into account the feed network loss, which was important. In Figure 60, the gain of the array at 44.5 GHz is 8.2 dB, which is effectively less than the theoretical expected value of 11.1 dB. An important percentage of the loss is due to the feed network, which includes three power dividers, four 90° bends, three 51° bends and transmission line discontinuities required for matching. The gain value obtained is still acceptable.

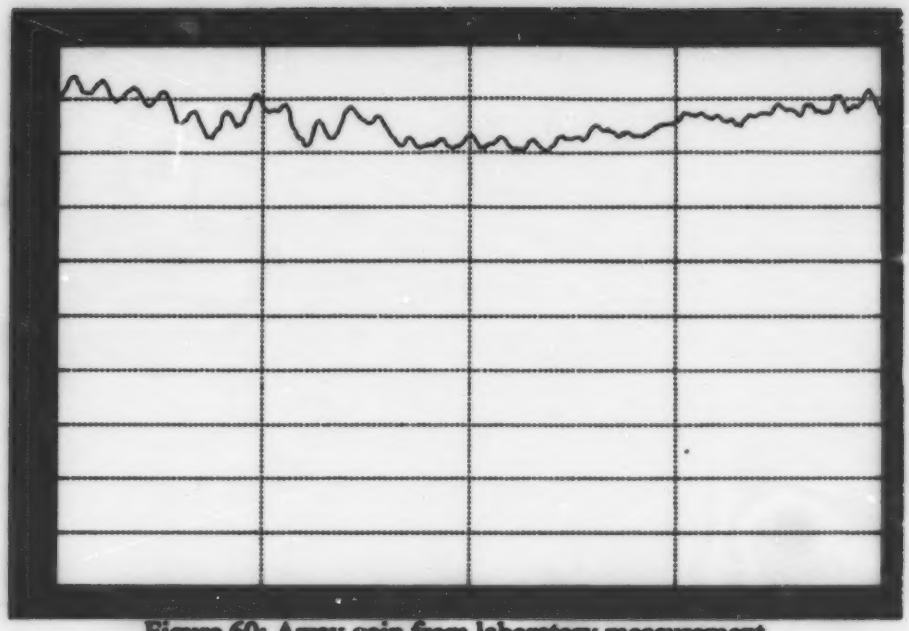

Figure 60: Array gain from laboratory measurement

The most important consideration in the measurement is the expected gain when the lens array is assembled and measured. The gain of the array by itself was required in order to enable the evaluation of the lens array performance.

4.6 Prototype 2 - Single Straight Face Lens for the Array

The purpose of prototype 2 was to evaluate the gain when moving from one single element to an array of four elements. The lens of prototype 2 had the same dimensions as the lens used for the fabrication of the lens array. The only important measurement required from prototype 2 was the gain since prototype 1 was used to validate radiation patterns from the simulation software. The configuration of prototype 2 was a straight face lens based on the design data for the lens comparison. However, there was one difference, that being the additional 1 mm thickness at the bottom of the lens for the support structure. The same simulation as prototype 1 was performed to find the best PO focal point. Figure 61 presents the focal region with the focal point chosen, in the red region, to be at 5 mm above the origin. From the GO design data, the patch was located 16.29 mm from the bottom of the lens. In prototype 2, the distance was then 10.29 mm from the bottom of the 1 mm support structure.

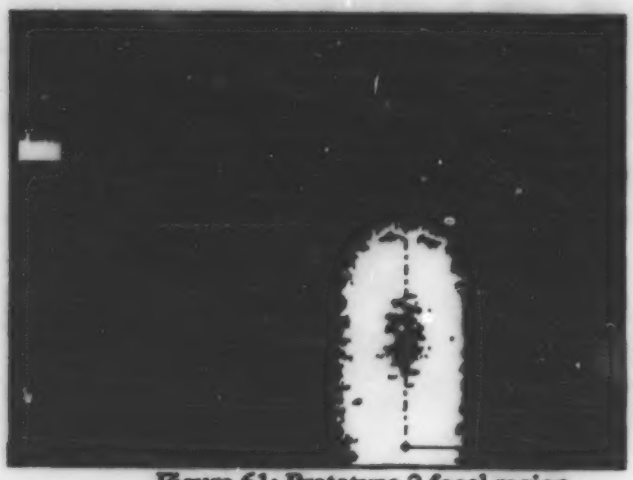

Figure 61: Prototype 2 focal region

The gain expected from prototype 2 was expected to be similar to the gain from prototype 1 since only minor modifications were done.

The gain of prototype 2 is shown in Figure 62.

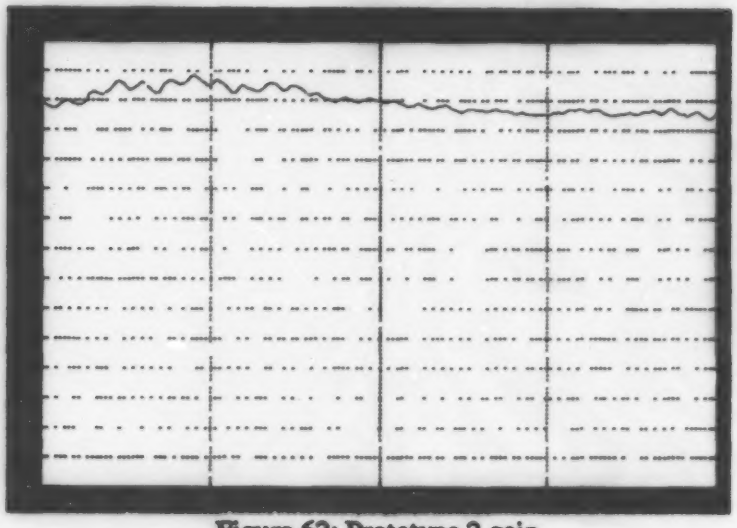

Figure 62: Prototype 2 gain

4.7 Prototype 3 - Lens Array

The lens array was made of four lenses from the design of prototype 2. The required measurements were the radiation patterns for various cuts, and the gain. The lens array was positioned, as for the prototype 2 measurements, at 10.29 mm from the radiating elements. Since this was the final design, extra measurements were taken to verify the cross-polarization characteristics of the antenna. Two possible comparisons between simulation and measurement for the array could be made. Because of the size of the model, HFSS could not be used to simulate the pattern of the array. Either the

simulated radiation pattern of a single element from HFSS or the measured pattern of prototype 2 could be used in ARPS to predict the pattern of a 4 element array. This would allow evaluation of mutual coupling between a patch and adjacent lenses since mutual coupling was not taken into account in ARPS. Figure 63 presents the results for the lab measurement and ARPS simulation using the HFSS radiation pattern for prototype 2. Measurement of the co-polarization and cross-polarization for the array and lens are presented in Figure 64.

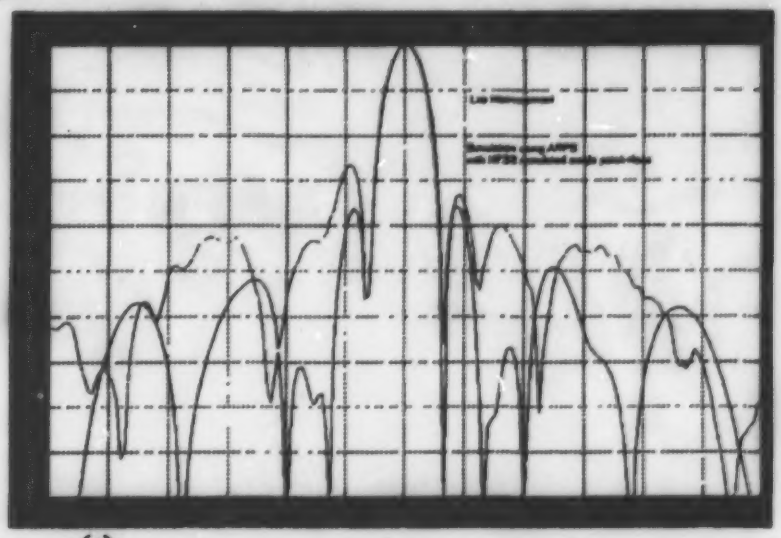

(a)

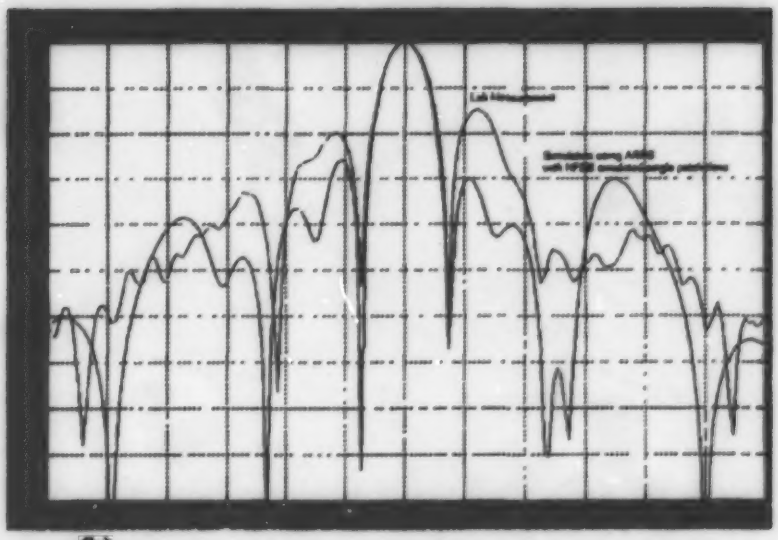

(b)

Figure 63: Array with lens comparison radiation patterns (a) phi=0° (b) phi=90°

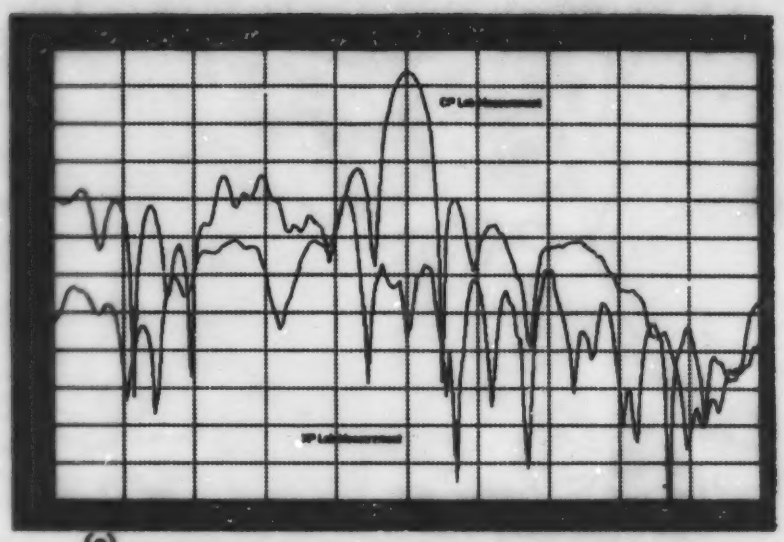

(a)

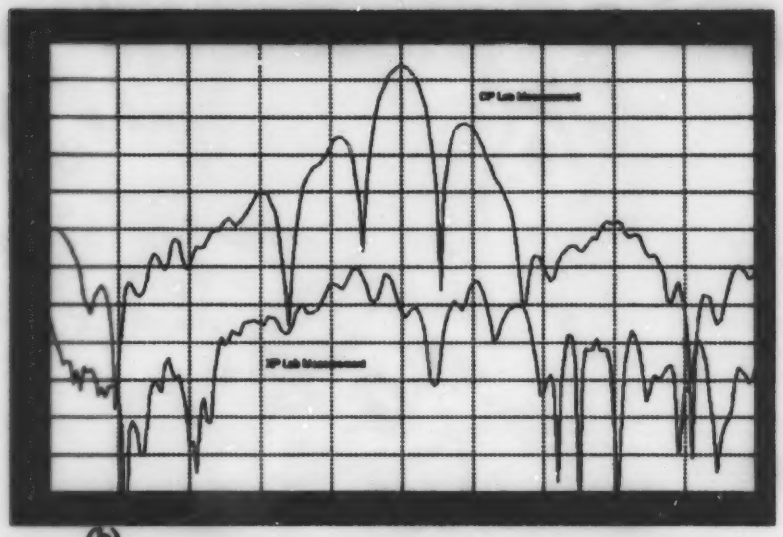

(b)

Figure 64: CP and XP comparison radiation patterns (a) phi=0° (b) phi=90°

From Figure 64, it can be mentioned that within the main beam region, the difference between the co-polarization and the cross-polarization was found to be in the 25 dB range, which is good. For the phi=0° cut, the cross-polarization increases for negative angles. This probably occurs because of the feed transmission line or the connector, however more investigation would be required to determine the exact cause.

The final required measurement was the gain of the microstrip array combined with the lens array, as shown in Figure 65. The measured gain value at 44.5 GHz for the array including the lenses was found to be 17.2 dB, which is an increase of 9 dB from the array gain without the lens.

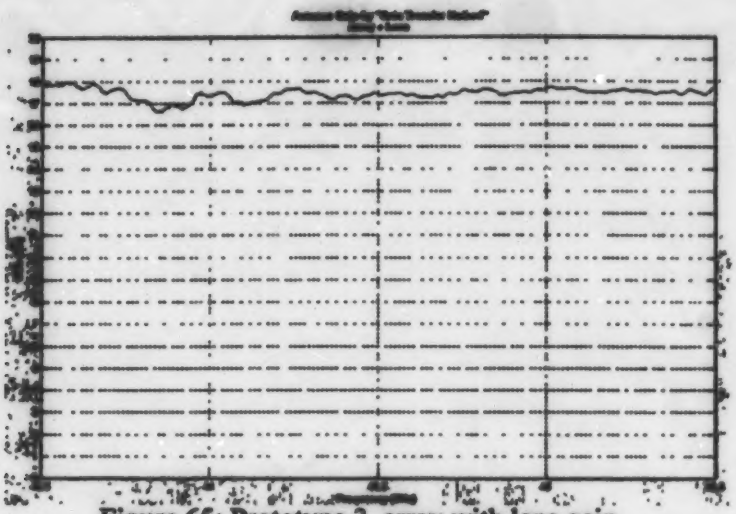

Figure 65: Prototype 3, array with lens gain

4.8 Prototype 4 - Meniscus lens

The lens design was based on the data for the meniscus lens from the lens comparison section. The measurements taken were the radiation patterns, shown in Figure 66. An investigation of the focal region was also conducted to observe the reflection effect for a meniscus type lens as presented in Figure 67. Finally, the gain of the meniscus prototype was measured and the result is presented in Figure 68. The patch was located at the GO focal point, which is the same location as the PO point simulated on HFSS, 12.99 mm from the maximum point of the inner lens surface.

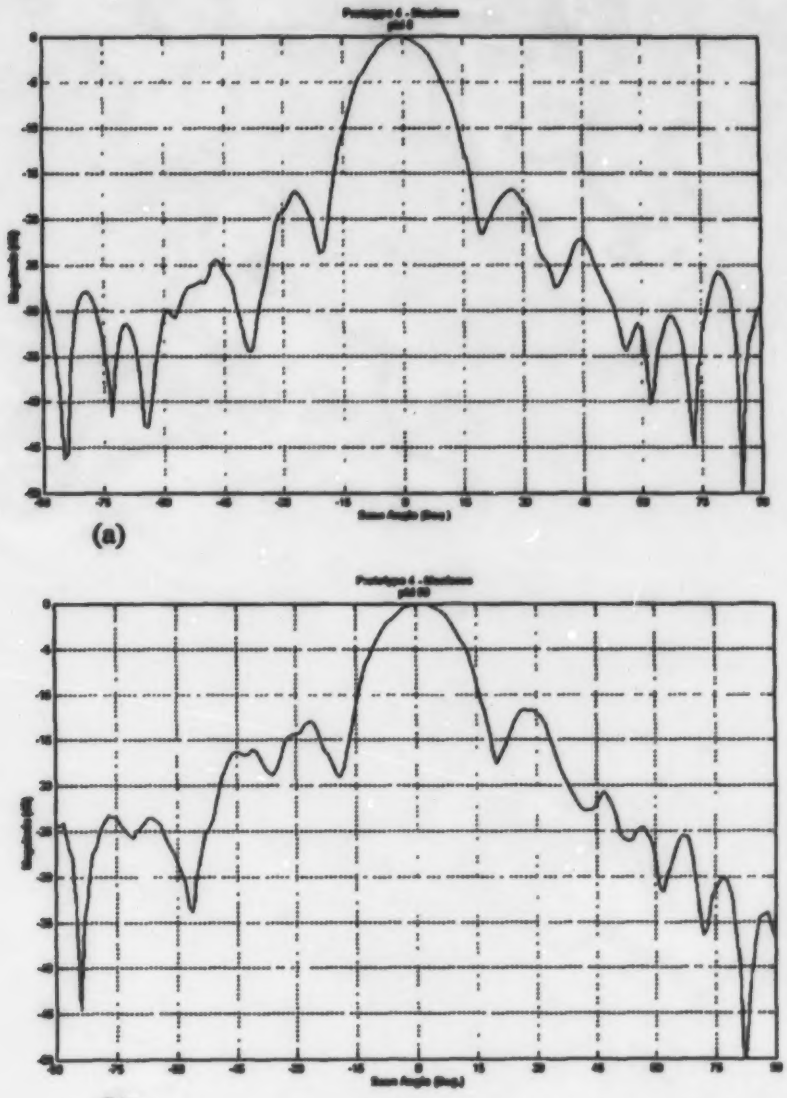

(a)

(b)

Figure 66: Prototype 4, meniscus lens, radiation patterns (a) phi=0° (b) phi=90°

By measuring the S_{21} value while changing the lens-to-patch distance, a standing wave was observed. This is the same reflection phenomenon as seen for prototype 1.

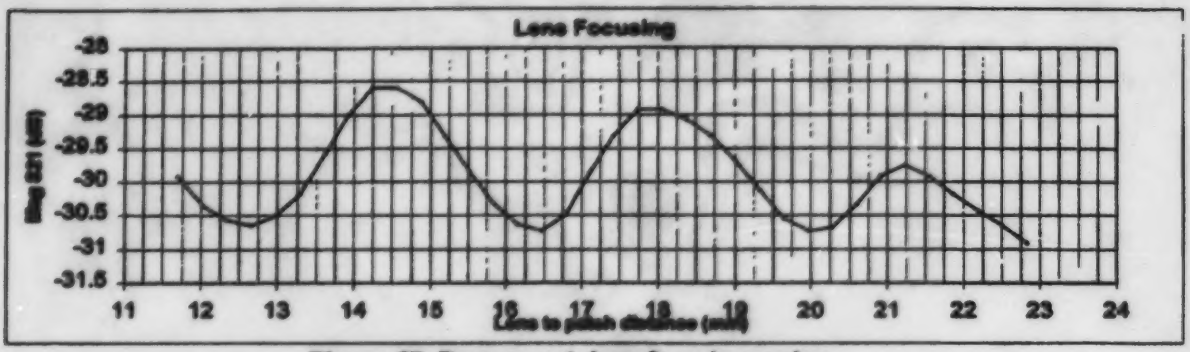

Figure 67: Prototype 4, lens focusing region

For the gain measurement, it can be noticed that for prototype 4, the meniscus lens, the gain was 14 dB at a distance of 12.99mm, which is higher than the 13.8 dB measurement from prototype 1. However by looking at the results from the investigation of the focusing region for prototype 1, Figure 56, the patch location was at 11.5 mm, which is in a region where the initial and the reflected signals are combined positively. For prototype 4, by looking at Figure 67, the two signals interfere destructively at a distance of 12.99mm. Even in the worst case, the meniscus lens provided a better result. An additional gain measurement was taken for the meniscus lens at a distance of 14.5 mm. A gain increase of 2.5 dB was noticed, resulting in a final gain value of 16.5 dB.

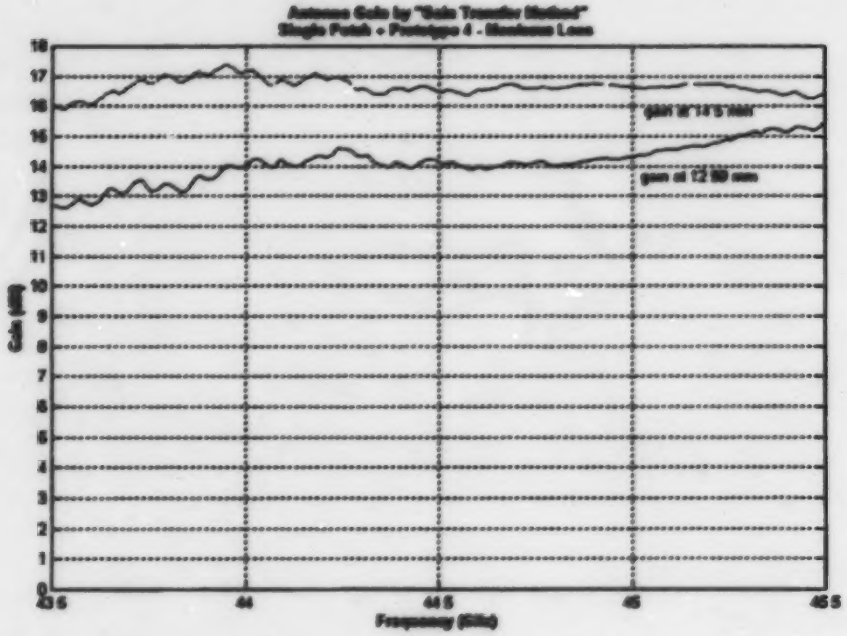

Figure 68: Prototype 4, Gain at various distances

CHAPTER 5: INTERPRETATION OF RESULTS AND DISCUSSION

5.1 Introduction

Interpretation of the results does not follow the same order as the presentation in Chapter 4. In the previous chapter, results from a previous section were required to lead to the development for the next section. In this chapter, the various aspects of the obtained results are discussed separately. They will be done in the following order: single element, single element and lens, array of elements without lens, array and lens. This will be followed by gain comparison from measurement results, analysis of the focusing region, four lens type discussion and selection of the possible best lens candidate.

5.2 Single Radiating Element

From the results presented in Chapter 4, the first aspect to be compared is the resonant frequency determined by measuring the S_{11} parameter. From comparison of both the simulation and the measurement, reasonably good results were obtained. The measured resonant frequency for the single element is 44.3 GHz, a difference of 0.5% compared to the simulated design resonant frequency of 44.5 GHz. This provides confidence in the design procedure.

Some problems were discovered with the initial measurements of the radiation patterns, especially for the E plane, phi = 90°, which is the plane intersecting the transmission line and the connector region. The occurring ripples were found to be caused by the edges of the support structure and the plexiglass bridge. By using absorbing material to mask the edges and the bridge, the ripples were attenuated. It was also noticed that the simulated pattern for phi = 90° in Figure 44 showed some ripples in the neighborhood of $\theta = -90°$; these can be attributed to the transmission line. The simulation patterns look wider than the measured pattern due to the fact that near ± 90° the measurements are at their limits. The patterns of the masked antenna compared acceptably well with that obtained through HFSS simulation.

5.3 Single Radiating Element with Lens, Prototype 1

It is obvious that by modeling a plane wave going through the lens, the focusing point is not the one predicted by the GO equations. This can be explained by the fact that GO equations were developed for signals having a frequency in the range of 40×10^{13} Hz, which is the lower range for visible light. At millimeter waves, the signal frequency is in the range of 40×10^{9} Hz, four orders of magnitude lower. The second explanation is that the equations used were derived from the thin lens theory, which assumes that the lens thickness is negligible compared to the focal length. In the cases considered here, the lens thickness is not negligible. However, the approximation was acceptable due to the fact that the focal point was determined using the plane wave simulation method. For prototype 1, the GO and PO focal lengths were 15 mm and 11.5 mm respectively, a difference of 3.5 mm.

With the current simulation design setup, comparison between the simulation and the measured patterns could be done only for the main beam, mainly in the region within

±10 degrees from boresight. The location of the first null and first side lobe could not be compared precisely. In the simulation, it was only possible to model a small portion of the lens support structure. The radiation of the single element onto the sides of the "absorbing radiation box" from HFSS simulation software influenced the final pattern. In the measurements, the energy from the radiating element not passing through the lens has to pass through the support structure. The support structure near the lens is tapered, in an attempt to minimize the unwanted effects by directing unwanted radiation away from the main lobe, however this was not totally successful. In general, the main beam from the simulation is wider than that found in the measurements, whether or not absorbing material was placed on the support structure. The shapes of the measured patterns without using the absorbing material agree more closely to those of the simulations. The absorbing material also covered the tapered region of the support structure, thus reducing the side lobes and the edge effects. Also, the absorbing material helped in providing a better understanding of the lens effects without the support structure.

Agreement between the simulated and the measured gain was good. A lower gain was expected for the measurement based on the feed network loss. From the simulation of the focusing region, by modifying the spacing between the lens and the patch, it can be seen that surface reflections from the lens had also to be taken into account. For both simulation and measurements, a standing wave pattern was predicted and observed, but the maxima in the patterns were not at the exact same location.

5.4 Four Element Array

The design of the four element array radiating elements was based on the same procedure as the single element with one improvement, that being the addition of a section of transmission line between the source and the matching line allowing the simulation of coupling effects during optimization. Simulation results predicted a resonant frequency of 44.52 GHz, however after fabrication and measurement, the resonant frequency was 44.3 GHz. A second design could have been submitted incorporating minor changes to achieve the desired resonant frequency. Because of time constraints and since the design frequency of 44.5 GHz is still within the operating band of the antenna, the design process was not repeated.

The radiation patterns obtained from the measurement are in agreement with the simulation using ARPS, as can be seen in Figure 59. Within ± 50° of boresight, the location of the nulls and the maxima are at the same location.

The gain of an array of 4 elements is expected to be 6 dB higher than that of a single element, when feed loss is not included. In this case, the single element gain was 5.1 dB, so the expected array gain was 11.1 dB. However, the total length of the feed network is 125 mm compared to 50 mm for the single element. The difference is 75 mm. Since the measured loss of a 50 mm length of transmission line is 2.15 dB, the loss of a 75 mm line is expected to be 3 dB. This would bring the expected gain of the array down to 8.1 dB. The measured gain of the array was 8.2 dB, a value close to that predicted.

5.5 Four Element Array with Lens, Prototypes 2 and 3

As expected, the PO focal point was not located at the same distance as the theoretical GO focal point for this type of lens; it was in fact located 5mm above the origin. By placing the lens at the same distance from the radiating elements for both prototypes 2 and 3, a gain comparison can be made between a single element and the combined array with their respective lenses. The gain difference is 4.5 dB.

For the simulation of the array patterns, the simulated pattern of one radiating element combined with one lens was used as a starting point. Four of these patterns were then combined in an array using the ARPS software. ARPS does not take into account the mutual coupling between one radiating element and adjacent lenses, or between adjacent elements.

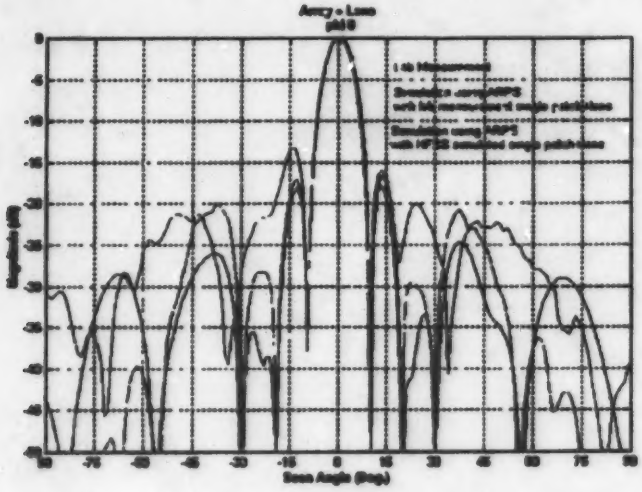

(a)

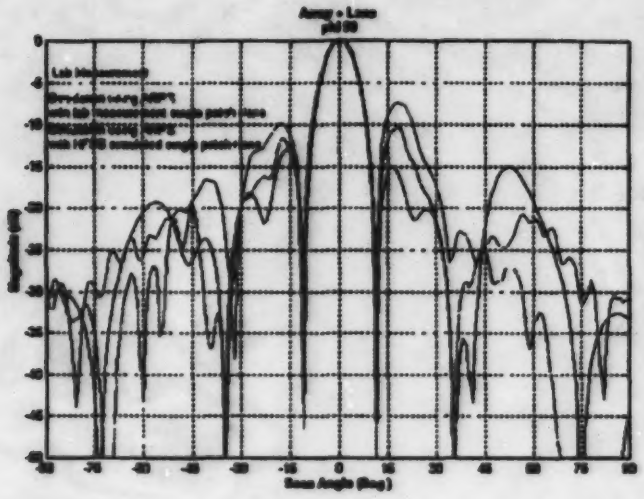

(b)

Figure 69: Array pattern comparison: lab measurement and simulation
(a) phi = 0^0 (b) phi = 90^0

The measurement of the cross-polarization (XP) was performed for the lens array setup. Previously, only co-polarization (CP) was presented. It can be seen that cross-polarization is not a problem within the main beam region with a minimum difference of 25 dB between CP and XP.

The gain of the array, including the lens is 17.2 dB, compared to 8.2 dB without the lens. An improvement of 9 dB was obtained.

5.6 Gain Comparison from Laboratory Measurements

In Figure 70, the gain of a single element and of the array, with and without lens are presented. This graph best summarizes the possible gain increase when using lenses. By using the lenses, an average increase gain of 9 dB was observed.

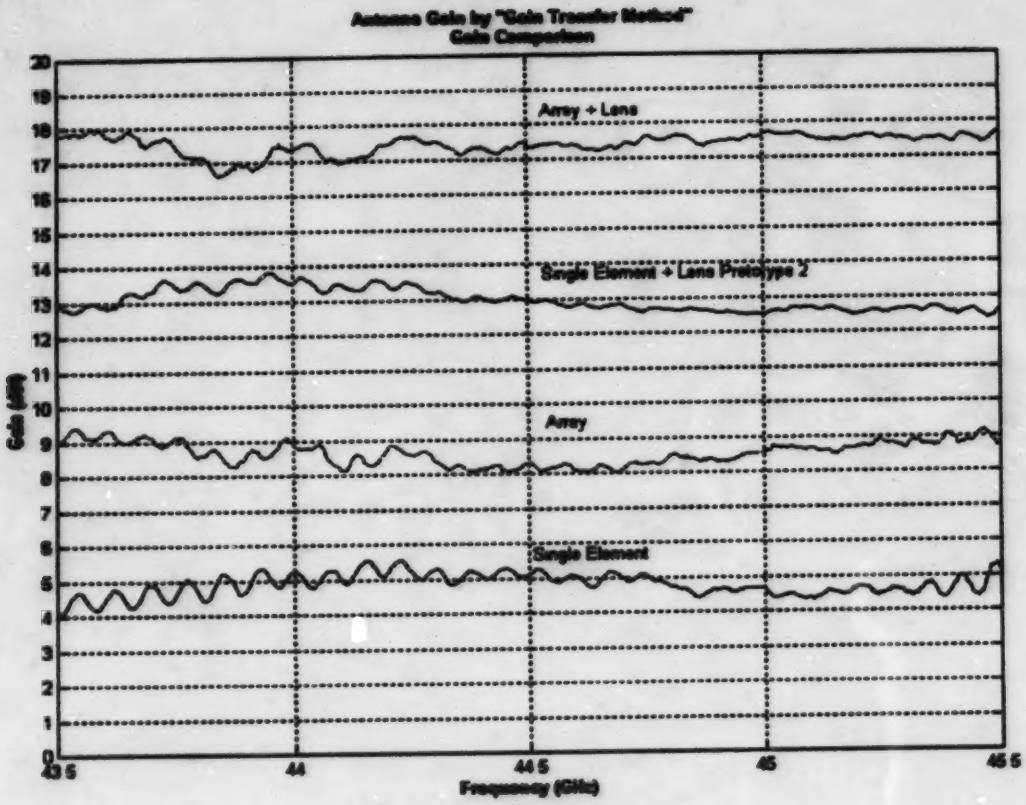

Figure 70: Gain comparison

5.7 Analysis of the Focusing Region

One of the important and significant aspects of this research was the study of the impact of the reflected signal at the bottom of the lens. This effect was first observed during measurement of Prototype 1, which was eventually simulated using HFSS.

The measured maximum of S_{21} for Prototype 1 occurred when the lens was moved one lf wavelength from the previous maximum. This resulted in an increase of one wavelength of travel for a signal reflected from the bottom of the lens, returning back to the patch location and being reflected back to the lens. The standing wave showing in Figure 71 comes from the combination of the initial signal and the reflected signal. It is noticed that the closer the lens is to the patch, the stronger is the standing wave, implying a greater impact from the reflected signal.

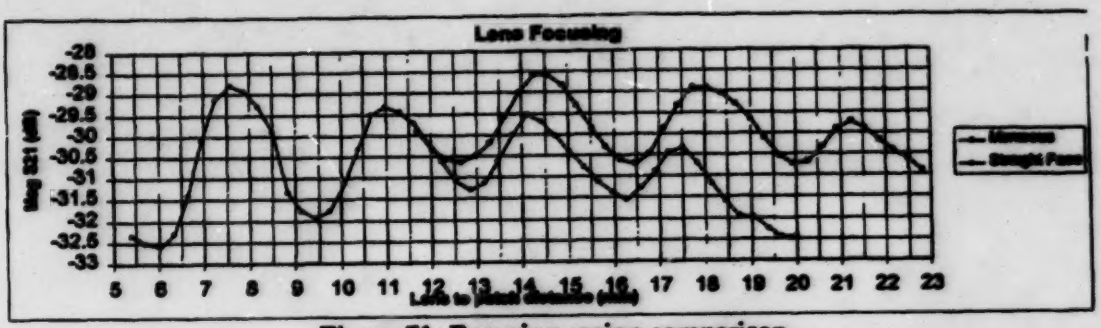

Figure 71: Focusing region comparison

For the simulation of Prototype 1, presented in Figure 55, the maximum gain from the antenna was also observed as a function of lens displacement over one half wavelength, 3.3 mm.

5.8 Comparison of the Four Lens Types

Based on the knowledge gained from the experimental measurements, it is now possible to comment with more confidence on the possible differences between the four lens types.

Each of the four lenses was designed using GO principles. Physical optics principles, incorporated into the HFSS modeling software, were used to predict the performance of each lens type. The discrepancy between the GO focal point of the design and the PO focal point from the simulation was the least for the meniscus type. However, the meniscus is the thickest lens, requiring the most material. For the three other lenses, having the PO focal point closer to the lens than predicted by GO is an advantage. This resulted in a reduced overall thickness of the antenna. Using the plane wave technique to find the focal point also provided information on how the lens would react as a receiving antenna. The meniscus lens is the one that will provide a more concentrated field.

It is obvious now that reflection process in the region between the lens and the patch is an important aspect. For the straight face lens, based on simulation and measurement, it can be said that the reflected signal will add positively to the primary signal when the lens is located at a multiple of a half wavelength from the patch. It is not yet possible to specify, for each lenses type, the required distance for the reflected and primary signals to add positively or negatively.

From the simulated radiation patterns obtained from HFSS, it can be said that for the four lens types, the gain is about 15 dB. However the effect of the reflected signal at these lens locations is not known . From the focal region simulation analysis of Prototype 1, it was seen that S_{21} could vary by up to 5 dB. As a general observation, the meniscus lens generated multiple side lobes compared to the three other types, but the side lobes were lower. Based on the current lens locations, the meniscus lens provided the narrower beamwidth, implying a better focused signal. Also the other types showed strong back radiation. Proper matching at the surface of the lens could once more reduce the back radiation.

5.9 Selection of the Lens

It is not easy with the current work accomplished in this research to select the lens which would provide the best performance in all circumstances. A more detailed analysis of the reflected signal would be required to assess the impact of the lens location. Surface matching would be required to eliminate this aspect of the problem. Without any matching, it appears that the meniscus lens proves a stronger concentration field for a received plane wave. The meniscus lens is also the one producing the lower back lobes. From the measured impact of the reflected signal, it can be seen that the meniscus lens provided improved S_{21} over the straight face lens when the lens is moved away from the patch. Based on this time limited research, the meniscus lens provided the best overall performance.

CHAPTER 6: CONCLUSIONS AND RECOMMENDATIONS

6.1 Summary

The design and simulation of a single microstrip patch radiating element and a four element array were carried out. In addition, various types of lenses were designed, simulated, and evaluated. The microstrip single radiating element and the four element array were fabricated and measured, as well as two lens types, the straight face lens and meniscus lens. Investigation of different lens types was accomplished and the goal of achieving a gain increase by using lenses was achieved.

As an intermediate goal, the design and optimization of a single radiating element as well as a four element microstrip array were required. Those designs were done from the beginning to allow a better understanding of microstrip design requirements. For the single element, the simulation and measured performances were similar. The resonant frequency of 44.5 GHz was within 0.5% and the radiation patterns were similar. For the array, a difference of 2.2% was observed for the resonant frequency. The antenna, however, was still operational at 44.5 GHz. The radiation patterns from simulations and measurements were in good agreement.

One major finding during this research was the impact of the reflection from the lens surface. For both prototypes, straight face lens prototype 1 and meniscus lens prototype 4, by modifying the lens-to-patch distance and measuring S_{21}, a standing wave was observed. The standing wave maxima occurred every half wavelength, confirming that the primary signal was combined with a reflected signal at a specific frequency of 44.5 GHz. Maxima, for both the straight face lens and meniscus lens, were at approximately the same location. However, the meniscus lens provided the improved signal transmission when the lens was moved away from the patch. A fluctuation of 2 dB was observed in the standing wave S_{21} measurement in the region of PO focal point.

6.2 Accomplishments

The accomplishments achieved based on the initial goals set out are summarized below.

6.2.1 New type of architecture for limited-scan array

The main goal of this work was to demonstrate the proof of the concept and to evaluate the increase in gain that could be achieved when using a lens over a patch radiating element. From the initial simulations, it was confirmed that the use of a lens above a microstrip patch element will increase the gain. From the simulation of a single element without lens the gain was 8.3 dB. From the lens simulations, with the patch located at the PO focal point, the predicted gain was between 15 dB and 16 dB for various lens types. This implied an increase in the gain of approximately 7.2 dB when the lens was added. Based on simulation only, the selection of the best lens is not obvious since their performances were similar.

From the measurement, the gain of a single patch was 5.1 dB. Additional loss has to be taken into account due to the feed network. With the radiating element located at the simulated PO focal point, for the straight face lens, prototypes 1 and 2, the measured

gain was 13.8 dB and 13 dB respectively. For the meniscus lens, the gain was 14.2 dB. The gain increase was thus approximately 8.6 dB. The measured gain of the array without the lens was 8.2 dB, and with the straight face lens array added, the gain was 17.2 dB. The gain increase was 9 dB. The use of lenses could be seen to increase the gain of a single element and the gain of the array.

An additional investigation of gain as a function of lens-to-patch distance was conducted. It was found out that by moving the meniscus lens away from the patch from its initial position of 12.99 mm to 14.5 mm, the gain increased from 14.2 to 16.5 dB, a difference of 2.3 dB. This is due to the interaction between initial and reflected signals.

6.2.2 Geometrical optics versus physical optics

It was shown by simulation that the location of the GO focal point initially predicted from the equations for each of the four lens types was only within the PO focal region for the meniscus lens type. For the plano-convex lenses, the center of the PO focal region was above the predicted GO focal point. The various focal point locations can be explained by the fact that GO equations were developed for signals having a frequency in the visible light range, approximately 1000 times that for the millimetre wave region. The second explanation is that the equations used were derived from the thin lens theory. However, it was demonstrated that a small lens, of only 3 wavelengths in diameter used at millimeter frequencies, still acts as a focussing device. The GO equations still apply in those conditions with optimization of the focal point using simulation software or laboratory measurements.

6.2.3 Optimum lens selection

Four lens types were analyzed using HFSS simulation software. They are: (a) plano-convex lens with the flat surface facing away from the patch radiating element, (b) meniscus lens, (c) straight face lens, which is the name given in this report to a plano-convex lens with the flat surface facing toward the patch radiating element, and (d) conventional lens, which is double convex. Two types, the straight face and the meniscus lenses, were fabricated and tested. The first prototype was a straight face lens. This initial lens was chosen based on the fact that fabrication was relatively easier compared to other types. This first prototype was used to validate the simulation software program. The meniscus lens provided the most interesting simulated results. To evaluate the real performance of a meniscus lens, a prototype was fabricated. Design of the lenses was based on GO equations. It has to be mentioned that the lens comparison based on the F/D ratio, focal length to lens diameter ratio, was not used to compare lenses.

Based on simulation results and measurement observations, the meniscus lens provide the most concentrated field at the PO focal region from a plane wave passing through the lens. Also from the simulation at the PO focal point, the meniscus lens provided the narrower main bean, implying the best focus. There were, however, multiple side lobes but no significant back lobe compared to other lenses. From the laboratory measurement, the gain of the meniscus lens was higher than that of the straight face lens for the simulated PO focal point distance. The minor drawbacks are the design and the fabrication complexity of the meniscus lens, and the requirement for slightly more material than the other lens types to be manufactured. Also, the total height of the antenna would be slightly higher with the meniscus lens compared to other types of lens.

The overall performance of the various lens types suggested that the meniscus lens is the optimum one to use.

6.3 Future Work

6.3.1 Aperture-coupled patches

The feed network used microstrip lines for its simplicity. However it has been seen that the radiation from the feed network interfered with the radiation of the patch, creating asymmetry in the overall radiation patterns. As well, increases in the cross-polarization have been noticed due to radiation from the transmission line. An alternate technique, to overcome some of the problems, would be to use the aperture-coupled feed configuration.

6.3.2 Lens matching

It was clearly identified that reflection on the lens surface was of great concern. Suitable matching will be required for any real world applications. Two techniques could be investigated. The first technique consists of adding to both surfaces a quarter-wavelength thick layer with an intermediate refractive index between that of the lens material and the air. This approach needs the availability of the proper material. The second technique is to modify the surface of the lens by adding slots or holes to change the effective dielectric constant. The dimension of the slots and their depth can be calculated for any incident angle and physically implemented on the lens. However due to the small size of the lens this technique might be difficult to apply.

6.3.3 Reduction of edge scattering

It has been understood that some differences from the simulated and measured radiation patterns were due to the configuration of the simulation design. In the simulation, to minimize the effect of the patch radiation on the side walls, the four side walls of the absorbing boundary box could be covered with simulated absorbing material. In the laboratory, absorbing material was placed on the edges of the support structure to minimize the edge effect. A more practical approach would be to use a larger substrate.

6.3.4 Circular polarization patches

Finally, to be most useful in the real world at 44.5 GHz, these techniques would need to be applied to circularly polarized antennas like the one used for EHF Satcom (Milstar). The radiating element array would also then be circular polarized.

REFERENCES

1. J.James and P. Hall, "*Handbook of Microstrip Antennas*", London, U.K., Peter Peregrinus Ltd, 1989.
2. Derneryd, A.G., "*A Theoretical Investigation of the Rectangular Microstrip Antenna Element*", IEEE Transactions on Antennas and Propagation, Vol. AP-26, No. 4, pp. 532-535, July 1978.
3. S. Noghanian and L. Shafai, "*Control of microstrip antenna radiation characteristics by ground plane size and shape*", IEE Proc.- Microw. Antennas Propag., Vol. 145, No. 3, pp. 207-212, June 1978.
4. S. Silver, "*Microwave Antenna Theory and Design*", McGraw-Hill Book Company, Inc, 1949.
5. Filipovic, D.F., Gearhart S.S., and Rebeiz, G. M., "*Double-slot Antennas an Extended Hemispherical and Elliptical Silicon Dielectric Lenses*", IEEE Transactions on Microwave and Techniques, Vol 41, No. 10, pp. 1738-1749, October 1993.
6. Filipovic, D.F.,Gauthier, G.P., Raman, S. , and Rebeiz, G. M, "*Off-Axis Properties of Silicon and Quartz Dielectric Lens Antennas*", IEEE Transactions on Antennas and Propagation, Vol. 45, No. 5, pp. 760-766, May 1997.
7. Dou, W.B., Zeng, G., and Sun Z.L., "*Pattern Prediction of Extended Hemispherical-Lens/Objective-lens Antenna System at Millimeter wavelengths*", IEE Proc.-Microw. Antennas Prog., Vol 145, no. 4, pp. 295-298, August 1998.
8. Eleftheriades, G.V., Brand, Y. Zurcher, J.-F. and Mosig J.R., "*ALPSS: A millimeter-wave Aperture-coupled patch antenna on a substrate lens*", Electronics Letters, vol. 33, No. 3, pp. 169-170., January 1997.
9. Neto, A., Maci, S., and de Maagt, P.J.I., "*Reflections inside an elliptical dielectric lens antenna*", IEE Proc.-Microw. Antennas Prog., Vol 145, no. 3, pp. 243-247, June 1998
10. Otero, P., Eleftheriades, G.V., and Mosig, J.R., "*Integrated Modified Rectangular Loop Slot Antenna on Substrate Lenses for Millimeter- and Submillimeter-Wave Frequencies Mixer Applications*", IEEE Transactions on Antennas and Propagation, Vol. 46, No. 10, pp. 1489-1497, Octobre 1998.
11. Zmuidzinas, J. and LeDuc, H.G., "*Quasi-Optical Slot Antenna SIS Mixers*", IEEE Transactions on Microwave Theory and Techniques, Vol 40, No. 9, pp. 1797-1804, Septembre 1992.
12. Gearhart, S.S., Rebeiz, G.M., "*A Monolithic 250 GHz Schottky-Diode Receiver*", IEEE Transactions on Microwave Theory and Techniques, Vol 42, No. 12, pp. 2504-2511, December 1994.
13. Rao, K.S., Chan, K., Tang, Q.M. and Kopal, J. "*EHF SATCOM PROJECT – XLENS, Final Report*", Spar Aerospace Limited, Quebec, 1995.
14. Constantine A. Balanis, "*Antenna Theory, Analysis and Design, 2nd edition*", John Wiley & Sons Inc., 1997.
15. "*Wiley Encyclopedia of Electrical and Electronics Engineering, Vol 1*", John Wiley & Sons Inc., 1999.

16. C.J. Sletten, "*Reflector and Lens Antennas -Analysis and Design Using Personal Computers*", Artech House Inc., Norwood, 1988.
17. C.S. Williams & O.A. Becklund, "*Optics: A Short Course for Engineers & Scientists*", John Wiley & Sons Inc., 1972.
18. N.F. Borrelli, "*Microoptics Technology – Fabrication and Applications of Lens Arrays and Devices*", Marcel Dekker Inc., New York, 1999.
19. Robert A. Sainati, "*CAD of Microstrip Antennas for Wireless Applications*", Artech House Inc., Norwood, 1996.
20. "*Getting Started: An Antenna Problem, Ansoft HFSS*", Ansoft Corporation, Pittsburg, PA, 1998.
21. "*IE3D Users Manuel Release 6*", Zeland Software Inc., Fremont, CA, 1999.
22. Hai Fong Lee and Wei Chen, "*Advances in Microstrip and Printed Antennas*", Wiley & Sons Inc., 1997.
23. Huang, J. "*Design of Printed Antennas for Wireless, Mobile, and Space Applications*",Boulder Microwave Technologies, Inc. July 10-12, 1997, Montreal, Quebec.
24. Traut, G. Robert, Rogers Corporation, Microwave and Circuit Material Division, http://www.rogers-corp.com/mwu/
25. Far Field, "*Antenna Radiation Patterns Software, Version 2.2, User's Guide*", 1998.
26. DOD, MIL-HDBK-141, Optical Design, 1962.

APPENDIX A: Matlab files for lens design

Meniscus lens m-file 1:

```
%Capt Rene Poirier
%Master These
%Meniscus Lenses
%27 October 1999
%Calculation of inner and outer contour of a MENISCUS LENS
%by giving Focal length and angle of coverage

%Variables
%Focal point
Focal=0;
%Er = dielectric constant of the lens
Er=input('Dielectric constant of the lens = ');
%N = lens index of refraction
N=sqrt(Er);
E=1/N;

%F = distance between F (focal point) and outer contour of lens with y=0
F=input('Focal length (at y=0), in mm = ');

%Teta limit
tetalimit=acos(1/N)*180/pi
%Max teta angle
tetamax=input('teta covered by le lens, in degree (max is tetalimit) = ');
tetamax=tetamax*pi/180; %in rad
%teta = angle in rad
teta=linspace(0,tetamax,20);
% D1 = radius of inner spherical contour
D1=F*(N-1)/(N-cos(tetamax))
% diameter of the lens
diameter=2*D1*sin(tetamax)
% D0 = thickness of the lens
D0=F-D1
%D/F
f_over_D=F/diameter

% inner contour of the lens
y1=D1.*sin(teta);
z1=D1.*cos(teta);

% outer contour of the lens
R2=F*(N-1)./(N-cos(teta));
y2=R2.*sin(teta);
z2=R2.*cos(teta);

figure(1)
plot (0,Focal,'*',z2,y2,z1,y1)
title('Design of Meniscus Lens')
xlabel('Z-axis')
ylabel('Y-axis')
```

Meniscus lens m-file 2:

```
%Capt Rene Poirier
%Master These
%Meniscus Lenses
%27 October 1999
%Calculation of inner and outer contour of a MENISCUS LENS
%by giving inner spherical radius, thickness of the lens and
%angle of coverage

%Variables
%Focal point
Focal=0;

%Er = dielectric constant of the lens
Er=input('Dielectric constant of the lens = ');

%N = lens index of refraction
N=sqrt(Er);

%D1 = distance between F (focal point) and inner contour of lens with y=0
D1=input('inner sperical radius (D1), in mm = ');

%D0 = lens thickness
D0=input('lens thickness,at y=0 (D0), in mm = ');

% Focal length
F=D0+D1;

%Teta limit
tetalimit2=acos(1/N);

%L = optimal radius at tetalimit2
L=F*(N-1)./(N-cos(tetalimit2));
if D1>L
  tetalimit1=acos(((D1*N)-(F*(N-1)))/(D1));
  tetalimit=tetalimit1*180/pi
  %diameter of the lens
  diameter=2*D1*sin(tetalimit1);
else
  tetalimit=tetalimit2*180/pi
  %diameter of the lens
  diameter=2*L*sin(tetalimit2);
end

%Max teta angle
tetamax=input('teta covered by le lens, in degree (max is tetalimit) = ');
tetamax=tetamax*pi/180; %in rad

%teta = angle in rad
teta=linspace(0,tetamax,20);% Focal length
F

%diameter of the lens
diameter
```

```
%f/D
f_over_D=F/diameter

% inner contour of the lens
y1=D1.*sin(teta);
z1=D1.*cos(teta);

% outer contour of the lens
R2=F*(N-1)./(N-cos(teta));
y2=R2.*sin(teta);
z2=R2.*cos(teta);

figure(1)
plot (0,Focal,'*',z2,y2,z1,y1)
title('Design of Meniscus Lens')
xlabel('Z-axis')
ylabel('Y-axis')
```

Conventional lens:

```
%Capt Rene Poirier
%Master These
%Conventional Lenses
%1 Nov 1999

%Calculation of inner and outer contour of a Conventional LENS

% NOTES:  Applicable for small diameter lens since approximation
%         sin(teta)=teta is used to determine the focal length


%Variables

epsilon=input ('Dielectric constant of the lens = ');
N=sqrt(epsilon);

%Radius of contour 1
R1=input('Radius of contour 1, (R1) = ');

%Radius of contour 2
R2=input('Radius of contour 2, (R2) = ');

%Angle of coverage

tetamax=input('angle of coverage (tetamax) ='); %in degree
tetamax=tetamax*pi/180; % in rad

teta=linspace(0,tetamax,20);

if R1<R2
  ymax=R1.*sin(tetamax);
else
  ymax=R2.*sin(tetamax);
end

y=linspace(0,ymax,20);

%Lens diameter
diameter=2*ymax


z1=sqrt(R1^2-y.^2);
z2=sqrt(R2^2-y.^2);


if R1<R2
  t10=z1(1)-z1(20);
  z2max=sqrt(R2^2-ymax^2);
  t30=z2(1)-z2max;
else  z1max=sqrt(R1^2-ymax^2);
  t10=z1(1)-z1max;
  t30=z2(1)-z2(20);
end
```

```
t1=t10-R1.*(1-sqrt(1-(y.^2./R1^2)));
t3=t30-R2.*(1-sqrt(1-(y.^2./R2^2)));


t0=t10+t30;

%Lens Thickness
T=t0

%Focal Length with focal point on left and parallel signal on right
f=1/((N-1)*(1/R1+1/R2))

y1=y;
y2=y;
z1=-t1+f;
z2=t3+f;


outer_distance=z2(1)

figure(1)
plot(z1,y1,z2,y2,f-f,0,'* )
title('Design of a Conventional Lens')
xlabel('Z-axis')
ylabel('Y-axis')
```

Plano-conves lens m-files:

```
%Capt Rene Poirier
%Master These
%Plano-Convex Lenses
%14 October 1999

%Calculation of inner and outer contour of a PLANO-CONVEX LENS

%Varisbles

%Focal point
F=0;

%Er = dielectric constant of the lens
Er=input('Dielectric constant of the lens = ');

%N = lens index of refraction
N=sqrt(Er);

%D1 = distance between F (focal point) and inner contour of lens with y=0
D1=input('Inner focal length (at y=0), in mm = ');

%Teta limit
tetalimit=acos(1/N)*180/pi

%Max teta angle
tetamax=input('teta covered by le lens, in degree (max is tetalimit) = ');
tetamax=tetamax*pi/180; %in rad

%teta1 = angle in rad
teta1=linspace(0,tetamax,20);


for i=1:20

  R(i)=(N-1)*D1/(N*cos(teta1(i))-1);

end

%inner contour of the lens
for j=1:20
  y1(j)=R(j)*sin(teta1(j));
  z1(j)=R(j)*cos(teta1(j));
end


%outer contour of the lens
y2=linspace(0,y1(20),20);
z2(1:20)=z1(20);

%outer focal length, at y=0
D3=z1(20)%diameter of the lens
diameter=2*y1(20)
```

```
%Lens thickness
D0=D3-D1

figure(1)
plot (F,F,'*',z2,y2,z1,y1)
title('Design of Plano-Convex Lens')
xlabel('Z-axis')
ylabel('Y-axis')
```

Straight face lens m-files:

```
%Capt Rene Poirier
%Master These
%Straight Face Lenses
%23 October 1999

%Calculation of inner and outer contour of a STRAIGHT FACE LENS

%Variables

%Focal point
F=0;

%Er = dielectric constant of the lens
Er=input('Dielectric constant of the lens = ');

%N = lens index of refraction
N=sqrt(Er);

%D1 = distance between F (focal point) and inner contour of lens with y=0
D1=input('Distance from F to inner contour,at y=0 (D1), in mm = ');

%D0 = thickness of the lens
D0=input('Thickness of the lens,at y=0 (D0), in mm = ');

%Teta limit
tetalimit=acos(D1/(N*D0-D0+D1))*180/pi

%Max teta angle
tetamax=input('teta covered by le lens, in degree (max is tetalimit) = ');
tetamax=tetamax*pi/180; %in rad

%teta1 = angle in rad
teta1=linspace(0,tetamax,20);

% inner contour of the lens
y1=D1*tan(teta1);
z1(1:20)=D1;

% variables required for outer contour
teta3=asin(sin(teta1)/N);

D3=N*D0+D1;

R=sqrt(y1.^2+z1.^2);

for j=1:20
  t(j)=((D3-R(j))*cos(teta3(j))/N-D0)/(cos(teta3(j))/N-1);
end

s=D0-t;

d=s.*tan(teta3);
% outer contour of the lens
```

```
z2=s+D1;
y2=y1+d;

% diameter of the lens

diameter=2*y2(length(y2))

figure(1)
plot (0,F,'*',z2,y2,z1,y1)
title('Design of Straight face Lens')
xlabel('Z-axis')
ylabel('Y-axis')
```

APPENDIX B: Lens design specification

Lens Design:

Using Capt Poirier Matlab mfiles

Plano-convex:

Dielectric constant of lens:	**2.53**
Theta max:	**25.523 degrees**
Inner length:	**17.2892 mm**
Lens Thickness:	**3.8753 mm**
Outer length:	**21.1645 mm**
Diameter:	**20.2108 mm**

Y1	Z1	Y2	Z2
0	17.2892	0	21.1645
0.4056	17.2973	10.1054	21.1645
0.8128	17.3215		
1.2232	17.3621		
1.6384	17.4194		
2.0602	17.4939		
2.4903	17.5863		
2.9308	17.6973		
3.3836	17.8281		
3.8512	17.9797		
4.3359	18.1538		
4.8407	18.3520		
5.3688	18.5765		
5.9236	18.8296		
6.5095	19.1145		
7.1312	19.4345		
7.7943	19.7940		
8.5055	20.1978		
9.2727	20.6522		
10.1054	21.1645		

Meniscus:

Dielectric constant of lens: 2.53
Theta max: 51.0461 degrees

Inner length: 12.9948 mm
Lens Thickness: 8.1697 mm
Outer length: 21.1645 mm

Diameter: 20.2108 mm

Y1	Z1	Y2	Z2
0	12.9948	0	21.1645
0.6091	12.9805	0.9902	21.1020
1.2169	12.9377	1.9673	20.9159
1.8220	12.8664	2.9186	20.6107
2.4231	12.7669	3.8326	20.1936
3.0188	12.6392	4.6991	19.6741
3.6080	12.4839	5.5095	19.0633
4.1892	12.3010	6.2572	18.3737
4.7611	12.0911	6.9376	17.6183
5.3227	11.8547	7.5477	16.8104
5.8725	11.5921	8.0866	15.9627
6.4094	11.3041	8.5545	15.0874
6.9322	10.9913	8.9532	14.1957
7.4398	10.6543	9.2854	13.2973
7.9310	10.2938	9.5546	12.4012
8.4048	9.9108	9.7649	11.5146
8.8601	9.5059	9.9206	10.6437
9.2960	9.0802	10.0262	9.7935
9.7114	8.6344	10.0863	8.9678
10.1054	8.1697	10.1054	8.1697

Straight face:

Dielectric constant of lens:	**2.53**
Theta max:	**31.8167 degrees**
Inner length:	**16.28775 mm**
Lens Thickness:	**4.87675 mm**
Outer length:	**21.1645 mm**
Diameter:	**20.2108 mm**

Y1	Z1	Y2	Z2
0	16.2878	0	21.1645
10.1054	16.2878	0.5655	21.1505
		1.1303	21.1086
		1.6937	21.0387
		2.2550	20.9411
		2.8136	20.8160
		3.3687	20.6634
		3.9199	20.4838
		4.4666	20.2773
		5.0084	20.0442
		5.5448	19.7848
		6.0756	19.4993
		6.6004	19.1880
		7.1191	18.8510
		7.6317	18.4885
		8.1381	18.1004
		8.6384	17.6866
		9.1329	17.2468
		9.6217	16.7808
		10.1054	16.2878

Conventional:

Dielectric constant of lens:	2.53
Theta max:	27.1939 degrees
Radius 1:	22.1123
Radius 2:	22.1123
Inner length:	16.2761 mm
Lens Thickness:	4.8884 mm
Outer length:	21.1645 mm
Diameter:	20.2108 mm

Y1	Z1	Y2	Z2
0	16.2761	0	21.1645
0.5319	16.2825	0.5319	21.1581
1.0637	16.3017	1.0637	21.1389
1.5956	16.3337	1.5956	21.1068
2.1275	16.3787	2.1275	21.0619
2.6593	16.4366	2.6593	21.0040
3.1912	16.5076	3.1912	20.9330
3.7230	16.5918	3.7230	20.8488
4.2549	16.6893	4.2549	20.7512
4.7868	16.8004	4.7868	20.6401
5.3186	16.9253	5.3186	20.5153
5.8505	17.0641	5.8505	20.3765
6.3824	17.2172	6.3824	20.2234
6.9142	17.3849	6.9142	20.0557
7.4461	17.5675	7.4461	19.8731
7.9779	17.7654	7.9779	19.6751
8.5098	17.9792	8.5098	19.4614
9.0417	18.2092	9.0417	19.2314
9.5735	18.4560	9.5735	18.9846
10.1054	18.7203	10.1054	18.7203

Prototype 1:

Straight Face Lens:

Dielectric constant of lens:	2.53
Theta max:	approx 36 degrees
Inner length:	15 mm
Lens Thickness:	6 mm
Outer length:	21 mm
Diameter:	20.075 mm

Y1	Z1	Y2	Z2
0	15	0	21.0000
10.9025	15	0.6208	20.9826
		1.2405	20.9305
		1.8582	20.8438
		2.4727	20.7227
		3.0833	20.5676
		3.6888	20.3788
		4.2887	20.1567
		4.8820	19.9018
		5.4683	19.6144
		6.0471	19.2951
		6.6180	18.9442
		7.1806	18.5620
		7.7351	18.1487
		8.2813	17.7043
		8.8196	17.2286
		9.3502	16.7213
		9.8738	16.1815
		10.0375	16
		10.9025	16

Prototypes 2 and 3:

Dielectric constant of lens: 2.53

Inner length: 16.28775 mm
Lens Thickness: 4.87675 mm
Outer length: 21.1645 mm

Support structure thickness: 1.00 mm

Diameter: 20.2108 mm

X	Z
0	5.8768
0.5655	5.8627
1.1303	5.8208
1.6937	5.7509
2.255	5.6533
2.8136	5.5282
3.3687	5.3756
3.9199	5.196
4.4666	4.9895
5.0084	4.7564
5.5448	4.497
6.0756	4.2115
6.6004	3.9002
7.1191	3.5632
7.6317	3.2007
8.1381	2.8126
8.6384	2.3988
9.1329	1.959
9.6217	1.493
10.1054	1

The lens locations for prototype 3 are:

Center of the plate:	**x = 0**	**y = 0**
Center of lens 1:	**x = -8.756**	**y = 14.915**
Center of lens 2:	**x = 8.756**	**y = 4.805**
Center of lens 3:	**x = -8.756**	**y = 5.305**
Center of lens 4	**x = 8.756**	**y = -15.915**

Prototype 4:

Meniscus:

Dielectric constant of lens: 2.53

Inner length: 12.9948 mm
Lens Thickness: 8.1697 mm
Outer length: 21.1645 mm

Support structure thickness: 1.00 mm

Diameter: 20.2108 mm

F1		F2	
X1	Z1	X2	Z2
0	4.8251	0	12.9948
0.6091	4.8108	0.9902	12.9323
1.2169	4.768	1.9673	12.7462
1.822	4.6967	2.9186	12.441
2.4231	4.5972	3.8326	12.0239
3.0188	4.4695	4.6991	11.5044
3.608	4.3142	5.5095	10.8936
4.1892	4.1313	6.2572	10.204
4.7611	3.9214	6.9376	9.4486
5.3227	3.685	7.5477	8.6407
5.8725	3.4224	8.0866	7.793
6.4094	3.1344	8.5545	6.9177
6.9322	2.8216	8.9532	6.026
7.4398	2.4846	9.2854	5.1276
7.931	2.1241	9.5546	4.2315
8.4048	1.7411	9.7649	3.3449
8.8601	1.3362	9.9206	2.474
9.296	0.9105	10.0262	1.6238
9.7114	0.4647	10.1054	1
10.1054	0	10.1054	0

DOCUMENT CONTROL DATA

(Security classification of title, body of abstract and indexing annotation must be entered when the overall document is classified)

1 ORIGINATOR (the name and address of the organization preparing the document Organizations for whom the document was prepared, e.g. Establishment sponsoring a contractor's report, or tasking agency, are entered in section 8)

Defence Research Establishment Ottawa
Department of National Defence
Ottawa, ON Canada K1A 0Z4

2 SECURITY CLASSIFICATION (overall security classification of the document, including special warning terms if applicable)

UNCLASSIFIED

3 TITLE (the complete document title as indicated on the title page Its classification should be indicated by the appropriate abbreviation (S,C or U) in parentheses after the title.)

Millimetre Wave Antennas Using an Array of Lenses (U)

4. AUTHORS (Last name, first name, middle initial)

Poirier, Capt. J.C.R., Moffat, J.W., Morin, G.A., Antar, Y.M.M.

5 DATE OF PUBLICATION (month and year of publication of document)	6a. NO. OF PAGES (total containing information. Include Annexes, Appendices, etc.)	6b. NO. OF REFS (total cited in document)
November 2000	xiii + 93	26

7. DESCRIPTIVE NOTES (the category of the document, e.g. technical report, technical note or memorandum. If appropriate, enter the type of report, e.g. interim, progress, summary, annual or final. Give the inclusive dates when a specific reporting period is covered)

DREO Technical Report

8 SPONSORING ACTIVITY (the name of the department project office or laboratory sponsoring the research and development Include the address.)

9a. PROJECT OR GRANT NO. (if appropriate, the applicable research and development project or grant number under which the document was written. Please specify whether project or grant)	9b. CONTRACT NO. (if appropriate, the applicable number under which the document was written)
5CA12	

10a ORIGINATOR'S DOCUMENT NUMBER (the official document number by which the document is identified by the originating activity. This number must be unique to this document.)	10b. OTHER DOCUMENT NOS (Any other numbers which may be assigned this document either by the originator or by the sponsor)
DREO TR 2000- 081	

11. DOCUMENT AVAILABILITY (any limitations on further dissemination of the document, other than those imposed by security classification)

(x) Unlimited distribution
( ) Distribution limited to defence departments and defence contractors; further distribution only as approved
( ) Distribution limited to defence departments and Canadian defence contractors; further distribution only as approved
( ) Distribution limited to government departments and agencies; further distribution only as approved
( ) Distribution limited to defence departments; further distribution only as approved
( ) Other (please specify):

12. DOCUMENT ANNOUNCEMENT (any limitation to the bibliographic announcement of this document. This will normally correspond to the Document Availability (11). However, where further distribution (beyond the audience specified in 11) is possible, a wider announcement audience may be selected.)

Full Unlimited Announcement

UNCLASSIFIED
SECURITY CLASSIFICATION OF FORM

13 ABSTRACT (a brief and factual summary of the document. It may also appear elsewhere in the body of the document itself. It is highly desirable that the abstract of classified documents be unclassified. Each paragraph of the abstract shall begin with an indication of the security classification of the information in the paragraph (unless the document itself is unclassified) represented as (S), (C), or (U). It is not necessary to include here abstracts in both official languages unless the text is bilingual)

One technique to increase the gain of a single radiating element is to use a conventional lens supported above a microstrip patch element. This configuration allows modification of both the inside and the outside surface curvatures of the lens. The frequency band studied is 43.5-45.5 GHz.

Four different lens types have been investigated using simulation software. Two lens types have been designed and fabricated, a plano-convex lens to validate the simulation software and a meniscus lens to validate the results of the most promising lens.

During this research, it was demonstrated that when using a lens above a radiating element, the gain is effectively increased. As a starting point, for a single element without a lens, the measured gain was 5.1 dB. From laboratory measurements, the gain while using a plano-convex lens with the straight face facing the radiating element was 13 dB, an increase of 7.9 dB compared to the measured single element. Using a meniscus lens, based on the same design criteria as the plano-convex lens, the gain increase was 9.1 dB. For an array of 4 elements using a four plano-convex lens array, a 9 dB increase in gain from 8.2 dB to 17.2 dB was measured. A major observation while doing measurement was the impact of the reflected signal from the inside surface of the lens. In the case of the meniscus lens, a gain fluctuation of 2.3 dB was observed when the lens-to-patch distance changed by 1.5 mm.

14. KEYWORDS, DESCRIPTORS or IDENTIFIERS (technically meaningful terms or short phrases that characterize a document and could be helpful in cataloguing the document. They should be selected so that no security classification is required. Identifiers such as equipment model designation, trade name, military project code name, geographic location may also be included. If possible keywords should be selected from a published thesaurus, e.g. Thesaurus of Engineering and Scientific Terms (TEST) and that thesaurus-identified. If it is not possible to select indexing terms which are Unclassified, the classification of each should be indicated as with the title.)

antennas
antenna arrays
planar antenna arrays
antenna phased arrays
microwave antenna arrays
millimetre wave antenna arrays
microwave antennas
antenna radiation patterns
lens antennas
directional antennas